Fluctuating moments in one and two dimensional Mott insulators

PhD Thesis

Miklós Lajkó

PhD supervisor: Karlo Penc

Budapest University of Technology and Economics
2013

Acknowledgements

I thank my supervisor, Karlo Penc, for his guidance and teaching throughout the past years.

I would like to thank Philippe Sindzingre for the joint work, and his kind welcome on my visit to Paris. I am grateful to Philippe Corboz, Andreas Läuchli, and Frédéric Mila for involving me in the study of SU(N) physics.

I appreciate the financial support of the Budapest University of Technology and the Wigner Research Centre for Physics. I owe special thanks to Attila Virosztek for offering a scholarship which allowed me to extend my PhD studies.

Finally, I would like to express my gratitude to my parents and my sister for their love and support, and I thank my friends for being my friends.

Contents

Chapter 1

Introduction

1.1 Hubbard model, Mott insulators

There are two conventional ways to picture the electron behavior in condensed matter. One considers the valence electrons traveling in the periodic potential of the nuclei that opens gaps in the quadratic free electron spectrum resulting in energy bands (near free electron approach). The other approach considers the electrons localized on nuclei, but allows the electrons in the valence shells to hop to neighboring positions (tight-binding model). The likelihood of the electron hopping is based on the overlap of the neighboring atomic wave functions. The hopping of electrons leads to the broadening of atomic energy levels into bands.

Though the two interpretations are conceptually different, both provide similar picture of the electron energy levels forming bands separated by gaps. Note that each energy level is doubly degenerate due to the spin degree of freedom of the electrons. In the band structure theory the electron-electron interaction is neglected and the ground state is thought to be a Fermi-sea state, where the lowest lying energy levels are filled till the Fermi-energy.

If the number of electrons in the unit cell is even, the Fermi energy lies between the uppermost fully filled and the lowermost empty bands, therefore any electron excitation must overcome the gap between these two bands, and the material will be a band insulator. Although, it can happen that there is no gap between the filled and empty band, or they even overlap, so the material behaves as a conductor (the number of states at the Fermi level is nonzero).

If the number of electrons in the unit cell is odd, we must have a partially filled band, in which case the band structure predicts conducting behavior. However, there are numerous materials, in particular among transition metal oxides, for which the experimental findings contradict to the predictions of band theory. For example, the CoO transition metal-oxide has a distorted rock

salt structure with a Co and O atom in the unit cell. The total number of electrons in the unit cell is odd, so according to the band theory it should be a conductor, yet it is a well-known insulator.

This contradiction calls for the revision of the band structure theory, and can be lifted if we consider the electron-electron interactions. We can implement the Coulomb repulsion between electrons in the framework of the tight-binding approach (for a detailed descriprion see [1]). The simplest model to discuss the electron-electron interaction as well is the Hubbard model,

$$H = -t \sum_{\sigma} \sum_{\langle i,j \rangle} \left(c^{\dagger}_{i,\sigma} c_{j,\sigma} + h.c. \right) + \sum_{i} U n_{i,\uparrow} n_{i,\downarrow} \tag{1.1}$$

where $c^{\dagger}_{i,\sigma}(c_{i,\sigma})$ creates (annihilates) an electron with σ spin on site i. The parameter t is the hopping integral and U is the Coloumb energy of two electrons placed on the same orbital with opposite spins. This model was introduced by Gutzwiller[2], Hubbard [3] and Kanamori[4] almost simultaneously in 1963. Anderson also considered a similar model in an earlier work [5], which can be viewed as a forerunner of this concept.

If $U = 0$, the probabilities that an orbital is occupied by an $\uparrow$ electron or by a $\downarrow$ electron are independent. Considering one electron per unit cell, the chance that there is an $\uparrow$ electron at site i is $1/2$, and the probability is the same for a $\downarrow$ electron as well. This means that in the Fermi-sea ground state the probability that a site is singly occupied is 1/2, while the probability that it is empty or doubly occupied is 1/4, respectively. If a large U Coulomb repulsion is introduced, states with only singly occupied sites are preferred. The strong Coulomb repulsion is responsible for the localization of electrons and the insulating nature of the material, since any hopping would result in a doubly occupied site. These correlation induced insulators, which are predicted to be conducting by the band structure, are called Mott insulators.

1.2 The origin of magnetism

In the $U \to \infty$ case, in the ground state of the half-filled Hubbard model, there is one electron with arbitrary spin at each site, which leads to a macroscopic, 2^N-fold degeneracy. If we consider a large, but finite U, second order perturbations prefer adjacent sites with antisymmetric spin configuration, since this allows for a process, where an electron hops to a neighboring site and back, lowering the energy by $-4t^2/U$. This process is prohibited for symmetric spin configuration by the Pauli principle. This leads to the effective low energy Hamiltonian

$$H_{\text{eff}} = -\frac{4t^2}{U} \sum_{\langle i,j \rangle} \left(1 - \frac{(\mathbf{S}_i + \mathbf{S}_j)^2}{2} \right), \tag{1.2}$$

where $(1-(\mathbf{S}_i+\mathbf{S}_j)^2/2)$ gives 1 if the spins of the electrons on sites i and j form an antisymmetric, i.e. a singlet state $\left|\uparrow_i\downarrow_j\right\rangle - \left|\downarrow_i\uparrow_j\right\rangle$, and gives 0 if the spins form a symmetric triplet pair. Since $(\mathbf{S}_i + \mathbf{S}_j)^2/2 = \mathbf{S}_i \cdot \mathbf{S}_j + 3/4$, the half filled Hubbard-model in the large-U limit leads to an effective antiferromagnetic Heisenberg model. This effective model provides the most basic example of interaction between the spins in a magnetic material. The origin of this interaction is the Coulomb repulsion and the perturbative exchange of the localized electrons.

In most compounds the magnetic sites (where the unpaired electrons are localized) are connected by non-magnetic ions with closed orbitals, and consecutive virtual hoppings lead to an effective exchange interaction. The sign and strength of this so-called superexchange can be given by collecting the contributions of the possible hopping paths, which can result even in ferromagnetic spin-spin interaction in the effective low-energy model.

Hopping processes involving multiple magnetic sites can lead to higher order spin terms in the effective magnetic model, an example is the ring exchange interaction, which describes the cyclic exchange of spins around a ring, which can involve four or more sites [6]. The four-spin ring exchange in the S=1/2 spin model reads as

$$H_{R.E.} = (\mathbf{S}_1 \cdot \mathbf{S}_2)(\mathbf{S}_3 \cdot \mathbf{S}_4) + (\mathbf{S}_1 \cdot \mathbf{S}_4)(\mathbf{S}_2 \cdot \mathbf{S}_3) - (\mathbf{S}_1 \cdot \mathbf{S}_3)(\mathbf{S}_2 \cdot \mathbf{S}_4), \tag{1.3}$$

which describes the cyclic exchange around the 1-2-3-4 loop in both directions. (See Fig. 1.1a)

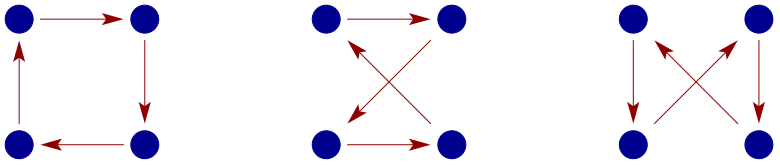

FIGURE 1.1: Three possible paths of the ring exchange interaction on a four site plaquette. Eq. (1.3) describes the rotation of the spins along the 1-2-3-4 path in both directions. The exchange path changes depending on the position of the "-" sign.

Signs of ring exchange interaction were found, for example in La_2CuO_4 [7], where the inelastic neutron scattering spectra were fitted by the results of a spin wave approach considering nearest, next nearest, third nearest and cyclic ring exchange interactions in the CuO_2 planes. The strength of the ring exchange interaction was found to be around one third of the nearest neighbor coupling.

We should note that ring exchange plays an important role in ^{3}He [8], where He atoms with S=1/2 nuclear spins form a bcc lattice at very high pressure (30 atmospheres) and low temperature. In this case the origin of the low energy effective spin model is the physical exchange of He atoms. The exchange of only two atoms is troublesome, because it is hard to squeeze them past each other, in the low energy effective model the spin-spin exchange terms are originated

from the cyclic exchange of three atoms[1], and the strength of the simple Heisenberg coupling is roughly the same as the strength of four-spin ring exchange terms in the effective magnetic model.

1.3 Orbital degeneracy

So far, we only allowed for spin degrees of freedom of the electrons in the Hubbard model. However, it is possible, that the electrons can be placed into multiple orbitals on the magnetic sites. In this case, the hopping amplitudes depend on the orbitals, and the Coulomb repulsion can be also different depending on whether two electrons occupy the same orbital (with antiparallel spins), or placed on different orbitals. A detailed discussion can be found in the book of Patrik Fazekas [1], section 5.4. In the large-U limit with a one electron/site filling, the low energy hamiltonian describes the exchange of not only the spin, but of the orbital degrees of freedom as well. In the special case of two orbitals, spin-1/2 like pseudo spin operators can be introduced, which act on the orbital degrees of freedom. Denoting the orbital states by $|a\rangle$ and $|b\rangle$ these are the eigenstates of the τ^z operator with $1/2$ and $-1/2$ eigenvalues, respectively, while the operators $\tau^\pm$ change one orbital state to the other, similar to the $S^\pm$ operators of the spin-1/2 degrees of freedom. An example of a simple spin-orbital Hamiltonian reads as

$$H_{KK} = \sum_{\langle i,j \rangle} \left[u + \mathbf{S}_i \cdot \mathbf{S}_j \right] \times \left[v + \alpha \left(\tau_i^+ \tau_j^- + \tau_i^- \tau_j^+ \right) + J'_z \tau_i^z \tau_j^z \right], \tag{1.4}$$

where the $\mathbf{S}_i$ operators act on the spin degrees of freedom, while the $\tau^\pm$ and τ^z operators act on the orbital degrees of freedom as discussed above. The spin term is isotropic due to the spin-rotation symmetry of the original system, while the orbital part is $U(1)$ symmetric only if we prohibit $|a\rangle \to |b\rangle$ type hoppings. If we allow for such hoppings, $\tau_i^- \tau_j^-$ and $\tau_i^+ \tau_j^+$, or even single τ_i^-, τ_i^+ terms are possible as well. These models were first discussed by Kugel and Khomskii [9]. The orbital and spin degeneracy allows for a large number of perturbative hopping processes in the low energy limit [10, 11].

For the special values of $\alpha = J'_z/2$ the orbital part of Eq. (1.4) is SU(2) symmetric as well. It is possible, that H_{KK} has even higher, SU(4) symmetry, at which point the spin-orbital states $(|\uparrow, a\rangle, |\uparrow, b\rangle, |\downarrow, a\rangle, |\downarrow, b\rangle)$ are equivalent, and the interaction is the exchange of the spin and orbital degrees of freedom of neighboring sites (See Chapter 4).

[1] Denoting the cyclic exchange of 3 spins by P_{123}, for S=1/2 spins $P_{123} + P_{123}^{-1} = P_{12} + P_{23} + P_{13} - 1$, where P_{ij} is the exchange of spin states at sites i and j.

1.4 Magnetic ordering

Up to this point, we gave a brief introduction to the origin of magnetism in condensed matter. In this short review we tried to emphasize the vast variety of the models, which can describe the low-energy behavior of these materials. However, this is only one side of a coin. The real question is, what kind of ordering these models exhibit, what is the low energy behavior of these systems [12]. Does the ground state show any kind of ordering, or symmetry breaking? What are the order parameters? What happens if we change the interactions? What are the relevant excitations? And so on.

Answering these questions is quite difficult in most of the cases. The frustration of the interactions and the quantum fluctuations can lead to a large number of possible orderings and ground state structures. Often, the classical approach, where we neglect the entanglement, i.e. the quantum mechanical nature of the system, can provide a good starting point. For systems with purely ferromagnetic interactions, the classical ground state of parallel spins is also the ground state of the quantum mechanical model, the quantum fluctuations are absent, and low energy excitations can be effectively treated by ferromagnetic spin-wave theory.

The case of antiferromagnetic interactions is different. If we consider a bipartite lattice with nearest neighbor Heisenberg interaction, the classical ground state is the two sublattice Néel-order with antiparallel neighboring spins. However, this state is not an eigenstate of the quantum mechanical Heisenberg Hamiltonian, so quantum fluctuations should be taken into account.

A way to address this problem is in the context of antiferromagnetic spin-wave theory, which is based on the assumption that the ground state is classically ordered. In the spin-wave theory, the quantum mechanical fluctuations lead to the shortening of the spins (more precisely, the zero point motion of the spins decreases the ordered moment). If these corrections are comparable to the length of the spin, it indicates that the initial ansatz was incorrect and a different kind of ordering takes place.

For higher dimensions and larger spins the spin wave theory usually gives small corrections and provides a good agreement with experiments. However, in low dimensional (1D or 2D) systems with small spins (mainly S=1/2), the entanglement plays an important role, and in these cases the classical approach is unable to capture the low energy physics of the system.

The most basic manifestation of entanglement is the antisymmetric singlet state of two S=1/2 spins, also called as a valence bond. In one or two dimensional S=1/2 spin systems, the formation of valence bonds is often energetically favorable to the classical ordering. This pairing usually leads to a distortion in the crystal structure, further stabilizing the pair formation [13–16].

If we consider two S=1/2 spins with antiferromagnetic $\mathbf{S}_1 \cdot \mathbf{S}_2$ Heisenberg interaction, the energy of an $|\uparrow_1\downarrow_2\rangle$ Néel state is $-1/4$, while for an antisymmetric valence bond, $|\uparrow_1\downarrow_2\rangle - |\downarrow_1\uparrow_2\rangle$, it is $-3/4$. However, a spin can form a valence bond with only one other spin, and the energy between two spins in different singlets is 0, so by increasing the number of neighbors, a classical Néel state may become favorable. For Z neighbors, the energy per site of the Néel state is $E_{\text{Néel}} = -Z/8$, that is to be compared with $E_{\text{VBC}} = -3/8$, and the Néel state wins for $Z > 3$ in this naive calculation.

The S=1/2 Heisenberg chain is exactly solvable by the Bethe ansatz [17], which gives an energy of $1/4 - \log(2) \approx -0.443$ per site. This is much smaller, than the energy of the Néel order $(-1/4)$ and even the energy of a nearest neighbor valence bond covering $(-3/8)$. The ground state can be described as a superposition of different valence bond coverings. The Heisenberg $\mathbf{S} \cdot \mathbf{S}$ interaction for S=1/2 spins can be rewritten as

$$\mathbf{S}_i \cdot \mathbf{S}_j = \frac{1}{2}\mathrm{P}_{i,j} - \frac{1}{4}, \tag{1.5}$$

where $\mathrm{P}_{i,j}$ exchanges the spins on site i and j, i.e. $\mathrm{P}_{i,j}\left|\alpha_i\beta_j\right\rangle = \left|\beta_i\alpha_j\right\rangle$, where α, β denote arbitrary spin states. Exchanging the spin states, mixing and moving the valence bonds can lower the energy of a static valence bond covering, creating eventually a resonating valence bond (RVB) ground state, where longer valence bonds are present as well. This construction was first proposed in the works of Philip W. Anderson and Patrik Fazekas, who studied the S=1/2 triangular lattice [18]. In this case the classical 120° antiferromagnetic order and a static nearest neighbor valence bond covering (valence bond crystal) construction has the same energy. Further investigations revealed, that the energy corrections considering the resonating valence bond picture were smaller than the spin-wave theory corrections to the Néel hypothesis [19], favoring an RVB ground state construction[2]. More recently, several models have been shown to accomodate RVB ground states [21–23].

The construction of Fazekas and Anderson of RVB states was the first instance of quantum spin liquids(QSL). Since then, spin liquids recieved increased attention from both theoretical and experimental side, since they represent a completely new type of approach to frustrated magnetic systems. An overview of quantum spin liquids can be found, for example in [24]. In general, quantum spin liquids are only characterized by the absence of any kind of–lattice or spin– symmetry breaking, which makes the experimental identification of these systems troublesome. Nevertheless, due to the increased scientific activity several materials were proposed as spin liquids [25, 26]. The development of numerical methods [27, 28] have also provided powerful tools in the study and identification of models with spin liquid states.

[2]We note that more recent numerical studies using exact diagonalization claim the existence of long range order for the triangular lattice [20].

1.5 Layout of the dissertation

In this work we present two instances of the effort to describe the ground state structure of magnetic models with the use of different analytical and numerical methods. Both topics provide an example of the importance of entanglement in low dimensional magnetic systems.

In the first part (Chapters 2 and 3) we will consider a model on a three-leg S=1/2 spin tube with nearest and next-nearest Heisenberg interactions and ring-exchange-like terms as well. This model was studied in the square lattice before, but as we will show, the ground state structure is really different on the three-leg tube. Based on the results of numerical exact diagonalizations, especially the form of the wave-functions, we were able to construct the exact ground states analytically and to provide a variational description of the low-lying excitations. Our findings provide an interesting insight into the physics of valence bond solids and resonating valence bond states. In this study we worked together with Philippe Sindzingre, who provided us with exact diagonalization calculations for larger systems.

In the second part (Chapters 4-7) we will consider SU(N) symmetric Heisenberg models. The recent experimental results in magnetic materials with orbital degeneracy [29], the realization of Mott insulating states in ultracold atoms in optical lattices [30], and the development of numerical methods renewed researchers' interest in these models.

We will discuss the SU(4) symmetric Kugel-Khomskii model on the honeycomb lattice. We will present substantial evidence that the ground state of this model is an algebraic spin-orbital liquid, where the correlations decay as a power-law with the distance. To reach this conclusion, we calculated the expectation values of the energy and the spin-spin correlations of different variational wave functions (Gutzwiller projected Fermi-sea states) using a Monte Carlo algorithm. We also investigated the stability and the robustness of the spin-orbital liquid state towards several kind of orderings.

This work was carried out as a part of a collaboration with Philippe Corboz, Andreas Laüchli and Frédéric Mila, where other methods were also used to investigate this system (exact diagonalization and tensor network algorithms). Our findings have strong experimental relevance as well, and are at the frontline of the search for spin liquid states in two dimensional Mott insulators.

We will use similar methods to discuss the ground state nature of the SU(3) symmetric Heisenberg model on the honeycomb lattice. In this case the results are less spectacular, we found a gapped plaquette state that breaks the translational invariance.

In both topics we will give a more detailed introduction to physics relevant in these systems, and since the to topics are not closely connected we will also make conclusions separately.

Chapter 2

Projection operators, exact ground states

In quantum spin models it is usually hard to decide what is the real ground state structure of a system. There are cases where mathematically rigorous theorems can be used to prove the existence of long range order, like for the square lattice with $S \geq 1$ spins [31, 32]. In certain cases, numerical methods can be used to identify the nature of the ground state (like the anti-ferromagnetic ordering for the S=1/2 square [33] and triangular lattice [20]). In other, mostly frustrated cases, the numerical methods are not powerful enough to characterize the ground state unambiguously.

There are a few cases when the ground state structure of a model can be given exactly. These models are sought-after, since they provide a solid starting ground for further investigation of the surrounding parameter space as well. Models with exact ground states are often created to accommodate a certain ground state structure. This can be done by using projection operators.

As the name shows, the projection operator approach is a concept to construct the Hamiltonian of a spin system as a sum of orthogonal projections. By definition a P projection is a linear transformation for which $P = P^2$, i.e. P leaves its image intact. P is an orthogonal projection if the kernel and the image of the transformation are orthogonal subspaces [1]. An orthogonal projection has two eigenvalues, 0 and 1, with a multiplicity corresponding to the dimensions of the kernel and the image. A simple geometrical example is the orthogonal projection onto the xy plane in $\mathbb{R}^3$ real space,

$$P_{xy} = \begin{pmatrix} 1 & 0 & 0 \\ 0 & 1 & 0 \\ 0 & 0 & 0 \end{pmatrix}. \tag{2.1}$$

[1] The kernel of an operator is the subspace of states for which $P|\Psi\rangle = 0$, while the image (also called as range) is the subspace of states which can be given as $P|\Psi\rangle$. For a P projection every state $|\Psi\rangle$ can be given as $|\Psi\rangle = P|\Psi\rangle + (1-P)|\Psi\rangle$, where $P|\Psi\rangle$ is part of the range of P, while $(1-P)|\Psi\rangle$ is in the kernel of P, since $P(1-P) = P-P^2 = P-P = 0$.

In this case the projection of a 3 dimensional vector (x, y, z) is simply $(x, y, 0)$. It is easy to see, that any further use of P_{xy} will have no effect, since $P_{xy}^2 = P_{xy}$. The kernel consists of the vectors $(0, 0, z)$ with an arbitrary real number z, while the image is the vectors in the xy plane. It is clear, that the range and the kernel of P_{xy} are orthogonal, therefore it is an orthogonal projection. For P_{xy}, 1 is an eigenvalue with a multiplicity of two and 0 is an eigenvalue with a multiplicity of one.

Projection operators in spin systems act on a group of spins and project out states according to the total spin of the group. In most of the cases projection based Hamiltonians are constructed to accommodate a certain ground state structure. If a Hamiltonian is a sum of projection operators, its eigenvalues are nonnegative, since each projection has nonnegative (0 or 1) eigenvalues. Therefore, if a state is an eigenstate of all the projections with an eigenvalue of 0 (i.e. it is in the kernel of all projections), it will be a ground state of the full Hamiltonian. Let us review a few, historically relevant examples.

2.1 Majumdar Ghosh model on the $S = 1/2$ spin chain

As we mentioned already, the nearest neighbor(J_1) S=1/2 Heisenberg chain is exactly solvable by the Bethe-ansatz, the unique ground state is gapless and can be described as a resonating valence bond state, which is a superposition of valence bond coverings. However, if a J_2 next nearest neighbor interaction is turned on, a quantum phase transition into a dimerized phase occurs at around $J_2/J_1 \approx 0.24$ [34]. Above the transition point the ground state is twofold degenerate, breaks the translational invariance of the system, and the excitations are gapped. The ground state is built out of short range valence bonds, rather than longer ones as in the RVB case. At a specific point, where $J_2/J_1 = 1/2$, the ground states were given exactly by Majumdar and Ghosh [35]. The Hamiltonian at this point can be given as a sum of projections, which allows us to capture the essence of the translational invariance breaking phase. The Hamiltonian at the Majumdar-Ghosh point is

$$H_{\mathrm{MG}} = \sum_i \left(\mathbf{S}_i \cdot \mathbf{S}_{i+1} + \frac{1}{2} \mathbf{S}_i \cdot \mathbf{S}_{i+2} \right), \tag{2.2}$$

which can be rewritten as

$$H_{\mathrm{MG}} = \sum_i \left[\frac{1}{4} \left(\mathbf{S}_i + \mathbf{S}_{i+1} + \mathbf{S}_{i+2} \right)^2 - \frac{9}{16} \right]. \tag{2.3}$$

The term $(\mathbf{S}_i + \mathbf{S}_{i+1} + \mathbf{S}_{i+2})^2$ has two eigenvalues $3/4$ and $15/4$ as the the total spin on the three adjacent sites is $1/2$ or $3/2$, respectively. This, up to constant factors is a projection. Rigorously

speaking,

$$P^{\mathrm{MG}}_{i,i+1,i+2} = \frac{1}{3}\left(\mathbf{S}_i + \mathbf{S}_{i+1} + \mathbf{S}_{i+2}\right)^2 - \frac{1}{4} \tag{2.4}$$

gives 1 for $|\mathbf{S}_i + \mathbf{S}_{i+1} + \mathbf{S}_{i+2}| = 3/2$ and 0 for $|\mathbf{S}_i + \mathbf{S}_{i+1} + \mathbf{S}_{i+2}| = 1/2$. So, the Majumdar-Ghosh Hamiltonian can be written as

$$H_{\mathrm{MG}} = \frac{1}{4}\sum_i \left[3P^{\mathrm{MG}}_{i,i+1,i+2} - \frac{6}{4}\right]. \tag{2.5}$$

H_{MG} gives its lowest possible value for states where the length of the sum of any three neighboring spins is $1/2$. For chains of even length this can be achieved by a state where pairs of nearest neighbor spins form valence bonds (See Fig. 2.1a),

$$\left|\Psi_{\mathrm{MG},1}\right\rangle = \bigotimes_l \left(|\uparrow_{2l-1}\downarrow_{2l}\rangle - |\downarrow_{2l-1}\uparrow_{2l}\rangle\right). \tag{2.6}$$

It is clear, that $\left|\Psi_{\mathrm{MG},2}\right\rangle = T\left|\Psi_{\mathrm{MG},1}\right\rangle$, where T is the translation by one site, is also a ground state (periodic boundary conditions are assumed). For chains of odd length this dimerized valence bond covering can only be achieved if one spin is left unpaired (Fig. 2.1b), in that case the ground state can be described as a single deconfined free spin (spinon) with $k = 0$ wave number. Similarly, the low lying excitations for even chains can be given as a pair of spinons or domain walls [36] (Fig. 2.1c). Fig. 2.1d shows the variational spectrum of the two domain wall (or two spinon) states for chains of even length, these excitations are clearly gapped, the shaded region shows the two domain wall continuum, and a bound state also appears in the singlet sector near $k = \pi/2$.

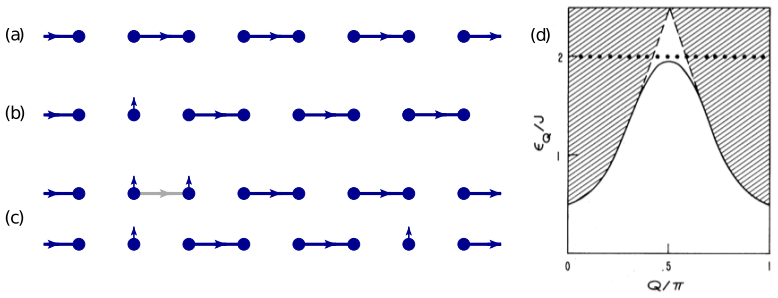

FIGURE 2.1: (a) One of the ground states of the Majumdar-Ghosh model at the $J_2/J_1 = 1/2$ point for spin-1/2 chains of even length. The arrows connecting two sites represent the valence bonds. In the other ground state, the valence bonds are shifted by one site. (b) In the ground state of odd length chains a single spinon or domain wall is propagating. (c) The low energy excitations for even length chains can be given as two domain walls, or spinons, on the valence bond order. Domain walls can be created by promoting a valence bond to a triplet, and than the spins can be separated. (d) The variational two domain wall spectrum taken from [36]. The shaded region is the two spinon continuum. A bound state appears at $k \approx 0.36$ and disappears at $k \approx 0.64$

2.2 S=1 chain with unique ground state, and gapped excitations

In case of one-dimensional half integer spin systems the Lieb-Schultz-Mattis theorem[37] proves that the ground state is either twofold degenerate or if the ground state is unique, the excitations are necessarily gapless. Haldane formulated the conjecture that Heisenberg chains with integer spins have a unique ground state with gapped excitations and an exponentially decaying correlation function. [38]. The first rigorous example for Haldane's conjecture was given by Affleck, Kennedy, Lieb and Tasaki for the S=1 chain with bilinear and biquadratic nearest neighbor interactions, where the ground state was exactly solvable, and the excitations were proven to be gapped [39]. In their construction they pictured an S=1 spin as two symmetrized S=1/2 spins on a site. If we form valence bonds between S=1/2 spins on adjacent sites, performing a symmetrization on each site will result in a valid S=1 spin state.

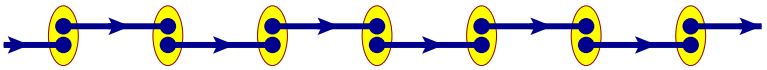

FIGURE 2.2: The AKLT ground state for the S=1 spin chain. This state is the exact ground state of the AKLT model. The blue dots dentote S=1/2 spin which are symmetrized on each site to form S=1 spins.

In this state the total spin of two adjacent sites is 1 at most, since in the spin-1/2 picture, the four S=1/2 spins on the two sites accommodate a valence bond. A Hamiltonian which accommodates this ground state structure can be given as a sum of projection operators,

$$H_{\mathrm{AKLT}} = \sum_i P^{\mathrm{AKLT}}_{i,i+1}, \tag{2.7}$$

where $P^{\mathrm{AKLT}}_{i,i+1}$ projects onto the subspace where $|\mathbf{S}_i + \mathbf{S}_{i+1}| = 2$. With this choice Ψ_{AKLT} will be the ground state of H_{AKLT} since it is an eigenstate of all projections with 0 energy. The projection operator can be rewritten using the S=1 spin operators as

$$P^{\mathrm{AKLT}}_{i,i+1} = (\mathbf{S}_i + \mathbf{S}_{i+1})^2((\mathbf{S}_i + \mathbf{S}_{i+1})^2 - 2) = \frac{1}{3} + \frac{1}{2}\mathbf{S}_i \cdot \mathbf{S}_{i+1} + \frac{1}{6}(\mathbf{S}_i\mathbf{S}_{i+1})^2 . \tag{2.8}$$

This model was the first example, but since then, several studies were made that provided further theoretical and experimental evidence for the existence of a Haldane gap in integer spin systems [40–42].

2.3 Valence bond crystals in two dimensions

The $S = 1/2$ two dimensional square lattice with nearest neighbor Heisenberg interactions (J_1) is generally accepted to exhibit Néel-order [33]. If we introduce next nearest neighbor interactions (J_2), the system undergoes a phase transition around $0.4 \lesssim J_2/J_1 \lesssim 0.6$, most-likely into an RVB-like spin-liquid phase [43]. Further increasing J_2, possible collinear, dimerized columnar and even plaquette ordered states were reported [44, 45]. For $J_2 \gg J_1$ the lattice is decoupled into two nearest neighbor Heisenberg square lattices. A valence bond crystal (VBS) structure also can be favored if we include third nearest neighbor [46], or higher order interactions as well.

In a special case the ground states can be exactly given. Batista and Trugman constructed a Hamiltonian for the S=1/2 square lattice which exhibits valence bond crystal (VBC) ground states [47] . The model they considered is

$$H_{BT} = \sum_{i=1}^{L} \sum_{j=1}^{L} R_{(i,j)(i+1,j)(i+1,j+1)(i,j+1)}, \tag{2.9}$$

where $R_{(i,j)(i+1,j)(i+1,j+1)(i,j+1)}$ acts on a four site square plaquette and projects onto the states where the total spin of this plaquette is 2. Any state where all plaquettes have a total spin of 0 or 1 is a ground state of the H_{BT}, such states can be seen in Fig. 2.3. Note that in these ground states each plaquette contains a valence bond, therefore each plaquette has a total spin of 1 at most.

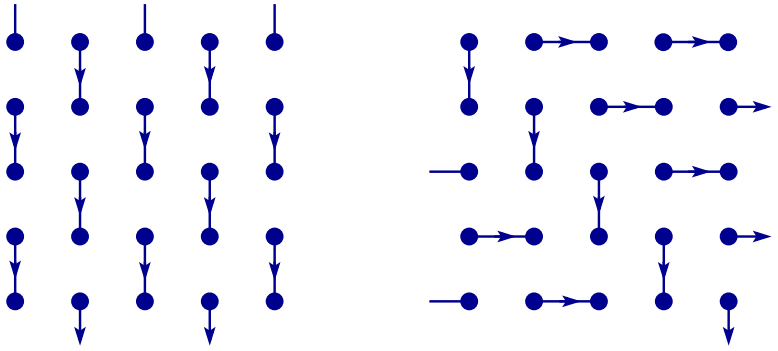

FIGURE 2.3: Possible ground states for the Batista Trugman model. Each four-site square plaquette contains a singlet bond, thus satisfying the corresponding R_α projection

On a system of $L_1 \times L_2$ sites with periodic boundary conditions, the number of plaquettes is $L_1 \times L_2$, and the system can be covered with $(L_1 \times L_2)/2$ valence bonds. So each valence bond has to satisfy two plaquettes. This means, that if a valence bond is put between next-nearest or further sites we won't be able to satisfy every plaquette. The same stands for the case where a plaquette has two valence bonds. Exact diagonalizations for finite systems show several ground states as expected, although if one collects the possible nearest neighbor valence bond coverings

a few ground states are unaccounted for. The 4×4 cluster with periodic boundary conditions has 14 nearest neighbor VBC ground states, however, exact diagonalization shows 16 singlet and even a triplet ground state, all with 0 energy. This means, that two singlet and a triplet ground state cannot be explained by the VBC picture. If we fix the lattice size in one dimension, the system can be viewed as a tube with L_1 legs ($L_1 = 3, 4, 5$ etc.). As we will see tubes with odd and even number of legs behave quite differently. This difference is in the frustration introduced by the periodic boundary conditions. Tubes of even length can have nearest neighbor valence bond crystal ground states as found by Batista and Trugman, while tubes of odd length can not accommodate such constructions. Nevertheless, exact diagonalization shows non-VBC ground states with 0 energy in both cases.

We would like to mention that if we consider systems with open boundary conditions the number of plaquettes is only $(L_1 - 1) \times (L_2 - 1)$, so additional ground states are present with defects in the valence bond crystal structure. Such defects can be next nearest neighbor valence bonds, or free, unpaired spins as well.

In the next chapter we will explain the origin of the additional, non-VBC like ground states in the case of the $L_1 = 3$, three-leg spin tube. In the end we will briefly contemplate on the case of tubes with higher number of legs as well [47].

Chapter 3

Exact ground states in three-leg spin tubes

Spin ladders were always considered as a starting step from one to higher dimensional systems. The finite extension in the second dimension allows for a much wider range of orderings and phases. A large number of compounds with ladder structure were synthesized which also boosted the scientific interest in these systems. All these circumstances led to a vast literature in this topic, for a review we refer to the paper of Dagott and Rice [48].

Tubes, i.e. ladders with periodic boundary conditions along the rung direction, attracted less attention, mainly due to the lack of experimental realizations. However, the additional frustration introduced by the boundary condition can provide a range of interesting phenomena [49].

The simplest case is the three-leg tube, where triangles with spins of length S ($S = 1/2, 1, 3/2 \dots$) at the vertices are coupled together. A simple model for such systems is

$$\mathcal{H}_0 = \sum_{i=1}^{L} \sum_{j=1}^{3} \left\{ J_\perp \mathbf{S}_{i,j} \cdot \mathbf{S}_{i,j+1} + J_1 \mathbf{S}_{i,j} \cdot \mathbf{S}_{i+1,j} + J_2 \left(\mathbf{S}_{i,j} \cdot \mathbf{S}_{i+1,j+1} + \mathbf{S}_{i,j} \cdot \mathbf{S}_{i+1,j-1} \right) \right\}, \tag{3.1}$$

where $J_\perp$ stands for the intra-triangle interaction, while J_1 and J_2 connects neighboring triangles. If $J_2 = 0$ then the topology of the system is a simple tube with square plaquettes on the sides [49–51] (See fig. 3.1b). If $J_1 = 0$ and $J_2 \neq 0$, then each site is connected to two sites in each neighboring triangle, and the tube is built of triangular plaquettes [52, 53].

Among the few compounds that exhibit a tube topology, $CsCrF_4$ has a three-leg structure [54], where the electrons on the half filled e_g band of the Cr^{3+} ions produce S=3/2 spins. The Cr ions form equilateral triangles which are stacked without rotation, thus arranged in a three-leg tube with square plaquettes. The Cr sites are connected by F ions in the tubes, while the triangles in different tubes are connected by Cs ions, which provides a really good separation. (See Fig 3.1).

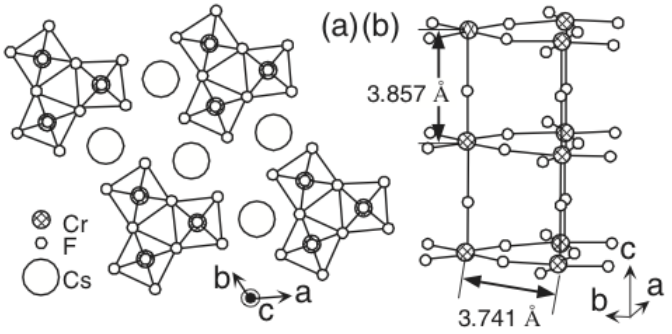

FIGURE 3.1: Structure of the the $CsCrF_4$. The Cr^{3+} ions are connected by F ions inside a tube, and the tubes are separated by Cs ions. Image taken form [54].

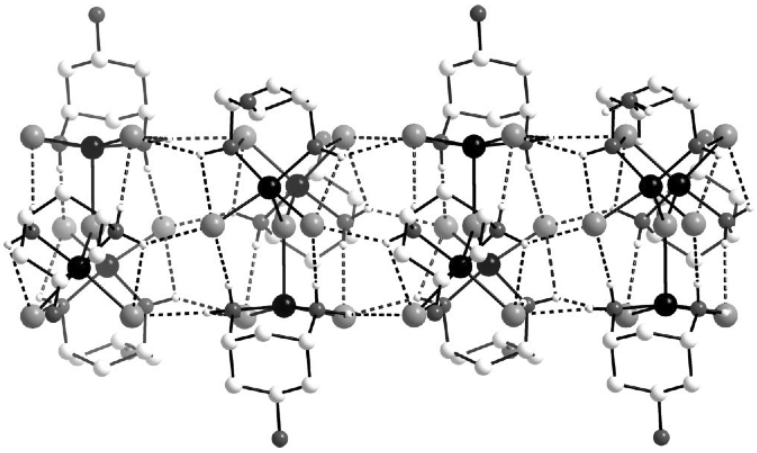

FIGURE 3.2: Structure of the the $[(CuCl_2tachH)_3]Cl_2$ The Cu ions as large black spheres, the N atoms as small black spheres, the Cl ions as large grey spheres, the carbon atoms as large white spheres, and the hydrogen atoms as small white spheres. Solid lines represent covalent bonds, while the dashed lines stand for hydrogen bonds. Image taken form [56]

.

Another example is the $[(CuCl_2tachH)_3]Cl_2$ compound, [55, 56], where the magnetic d^9 Cu atoms have a spin-1/2 degree of freedom, forming Cu_3Cl triangles. Cu atoms in neighbouring triangles are connected via $Cu - Cl \cdots H - N - Cu$ superexchange (the dots denote a hydrogen bond between the Cl and H atoms). Neighboring triangles in a tube are rotated by 180 degrees compared to each other, resulting in a triangular structure (see Fig. 3.2). Despite the long exchange route, experiments show that the superexchange between the triangles is of the same magnitude as the intra-triangle exchange mediated by chloro-ligands and hydrogen bonds.

From now on we will consider the S=1/2 case, and will give an introduction to the common properties of these systems.

3.1 A single triangle of $S = 1/2$ spins

The basic building block of the three-leg tube is a single triangle, which has a C_3 rotation axis and 3 symmetry planes, forming a D_3 symmetry group. A schematic figure of the symmetry elements, and the character table of the D_3 group is shown in Fig. 3.3. The D_3 group has two one-dimensional (A_1, A_2) and a two-dimensional (E) irreducible representation. The transformation of the energy eigenstates under the effect of the symmetry elements can be classified by these irreducible representations.

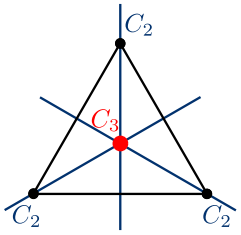

$C\mathrm{Id}$

D_3	Id	$2C_3$	3σ
A_1	1	1	1
A_2	1	1	-1
E	2	-1	0

FIGURE 3.3: Symmetries of a triangle, C_3 rotation axis marked by a red dot, and is perpendicular to the plane of the triangle. Each of the three mirror plane goes through the center and one site of the triangle, and is also perpendicular to the plane. The character table shows the three irreducible representations of D_3.

The eight dimensional Hilbert space of three S=1/2 spins can be split into a four dimensional $S^{\Delta} = 3/2$ and a pair of two dimensional $S^{\triangle} = 1/2$ subspaces.

$$\frac{1}{2} \otimes \frac{1}{2} \otimes \frac{1}{2} = \frac{1}{2} \oplus \frac{1}{2} \oplus \frac{3}{2}. \tag{3.2}$$

In our case, the three S=1/2 spins are at the vertices of the triangle and coupled by Heisenberg interactions. The energy on the triangle is given by

$$J_{\perp} \left(\mathbf{S}_1 \cdot \mathbf{S}_2 + \mathbf{S}_2 \cdot \mathbf{S}_3 + \mathbf{S}_3 \cdot \mathbf{S}_1\right) = J_{\perp} \left(\frac{1}{2} \left(\mathbf{S}_1 + \mathbf{S}_2 + \mathbf{S}_3\right)^2 - \frac{9}{8} \right) \tag{3.3}$$

which has two degenerate energy levels, it gives $6J_{\perp}/8$ for the $S^{\triangle} = 3/2$ quadruplet and $-6J_{\perp}/8$ for the two, degenerate $S^{\triangle} = 1/2$ doublet states. For ferromagnetic $J_{\perp}$ Heisenberg interaction in the triangle, the $S_{\triangle} = 3/2$ quadruplet has lower energy, while for the antiferromagnetic case, the $S_{\triangle} = 1/2$ doublet states are preferred.

The four $S^{\triangle} = 3/2$ states transform as the totally symmetric A_1 irreducible of D_3, and can be further distinguished by the z component of the total spin as $S^z = 3/2, 1/2, -1/2$ and $-3/2$. The two doublets both have a spin-1/2 degree of freedom. For these states a chirality, or pseudo-spin degree of freedom can be introduced to distinguish the two doublets. An orthonormal basis for the $S^{\triangle} = 1/2$ states can be given as

$$|\sigma, \tau\rangle = |\nu^{\sigma,1}\rangle + e^{\pm \frac{2\pi i}{3}} |\nu^{\sigma,2}\rangle + e^{\pm \frac{4\pi i}{3}} |\nu^{\sigma,3}\rangle, \tag{3.4}$$

where the $|\nu^{\sigma,j}\rangle$ are states with a valence bond between sites $j+1$, $j+2$ and an unpaired spin σ on site j of the triangle,

$$|\nu^{\sigma,j}\rangle = \frac{1}{\sqrt{2}}(|\sigma_j \uparrow_{j+1}\downarrow_{j+2}\rangle - |\sigma_j \downarrow_{j+1}\uparrow_{j+2}\rangle), \tag{3.5}$$

considering periodic boundary conditions in j. The upper(lower) signs in the exponents in Eq. (3.4) stand for the $\tau = l(r)$ chirality (see also Fig. 3.4). The $|\sigma, l\rangle$ and $|\sigma, r\rangle$ states are eigenstates of the C_3 rotation with an eigenvalue $e^{\pm 2\pi/3}$. Up to a phase factor each mirror plane takes these states one to the other, hence a $|\sigma, r\rangle, |\sigma, l\rangle$ pair belongs to the two dimensional irreducible representation E.

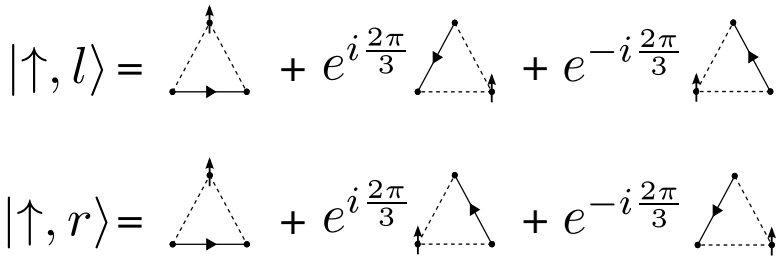

FIGURE 3.4: The S=1/2 states on a triangle with spin and chirality degrees of freedom. The arrow between two sites denotes a valence bond $|\uparrow\downarrow\rangle - |\downarrow\uparrow\rangle$, while the small arrow on a site denotes a free spin.

We note that these spin-chiral states are eigenstates of the scalar-chirality $\mathbf{S}_1 \cdot (\mathbf{S}_2 \times \mathbf{S}_3)$ [57, 58] on the triangle with eigenvalues $\pm\sqrt{3}/4$. The S=3/2 states are also eigenstates of the scalar-chirality with eigenvalue 0.

3.2 Weakly coupled triangles, overview

For weak inter-triangle interactions ($J_1, J_2 \ll |J_\perp|$) we can achieve an effective spin-3/2 model, or an effective spin-chiral model on the three-leg spin-1/2 tubes, depending on the sign of $J_\perp$.

For ferromagnetic $J_\perp$, the effective low energy Hamiltonian is the one dimensional S=3/2 Heisenberg-model, assuming that no higher order interactions are present on the tube. The spin-chiral limit for antiferromagnetic $J_\perp$ is more interesting, the effective Hamiltonian is similar to the Kugel-Khomskii spin-orbital model that we discussed in Chapter 1 [59]. In case when only $J_1, J_2, J_\perp$ interactions are present the effective model takes the form

$$H_{\text{eff}} = \sum_{i=1}^{N} \frac{2}{3}(2J_2 + J_1)\,\boldsymbol{\sigma}_i\boldsymbol{\sigma}_{i+1}\left[1 + \frac{4(J_2 - J_1)}{2J_2 + J_1}\left(\tau_i^+\tau_{i+1}^- + \tau_i^-\tau_{i+1}^+\right)\right], \tag{3.6}$$

where the $\sigma_i^\pm$ and σ_i^z operators act on the spin degrees of freedom, and the $\tau_i^\pm$ and τ_i^z operators act on the chirality degrees of freedom. The SU(2) invariance in the original Hamiltonian results in

an isotropic exchange between the spin degrees of freedom, and the C_3 symmetry is responsible for the $U(1)$ symmetry of the chirality degrees of freedom.

There are several ways to extend the Hamiltonian (3.1). For example, one can include interactions between next nearest triangles [60], or higher order terms as well. We can introduce anisotropy in the triangles by weakening one of the bonds [51], which breaks the degeneracy of the $|\sigma, \tau\rangle$ states on the triangle resulting in a different low energy behavior in the weakly coupled limit. It also allows us to discuss the transition between the tubes and the ladders.

3.3 Three-leg spin tube with ring exchange interaction

We studied a three-leg $S = 1/2$ spin tube with $J_\perp$, J_1, J_2 and fourth-order ring exchange interactions. The model is the application of the Hamiltonian of Batista and Trugman [47] introduced in Eq. (2.9) on the three-leg spin tube.

3.3.1 Projection operator approach on the three-leg spin tube

Spin tubes can be viewed as two-dimensional systems with a finite extension in the direction perpendicular to the axis of the tube . The three-leg spin tube is the most extreme case, being only three sites wide in the rung direction. We consider the Hamiltonian (2.9) of Batista and Trugman [47] on the spin tube, where the projections are applied on the square plaquettes on the sides of the tube.

Just like in the two-dimensional case, if we find a state where every plaquette has a total spin of 1 at most, it will be a good ground state. We can start the search among the static valence bond coverings. In the square lattice it was crucial that in a valence bond covering ground state all valence bonds should be nearest neighbor bonds and no plaquettes should have two valence bonds. The problem is that the tube can not accommodate a valence bond coverings where each plaquette contains a valence bond. In general, for an $L_1 \times L_2$ system with periodic boundary conditions static valence bond covering ground states exist only if both L_1 and L_2 are even.

On the other hand, exact diagonalization for three-leg tubes with an even number of triangles, up to 12 triangles (36 spins) show three singlet ground states with zero energy. What is more surprising, we find an S=1/2 doublet ground state with 0 energy for tubes of odd length as well (See Fig. 3.5). In both cases periodic boundary conditions are considered. Since the D_3 symmetry operations and the longitudinal translations are interchangeable, the energy eigenstates can be classified by the irreducible representations of the D_3 symmetry group and the wave vector along the tube.

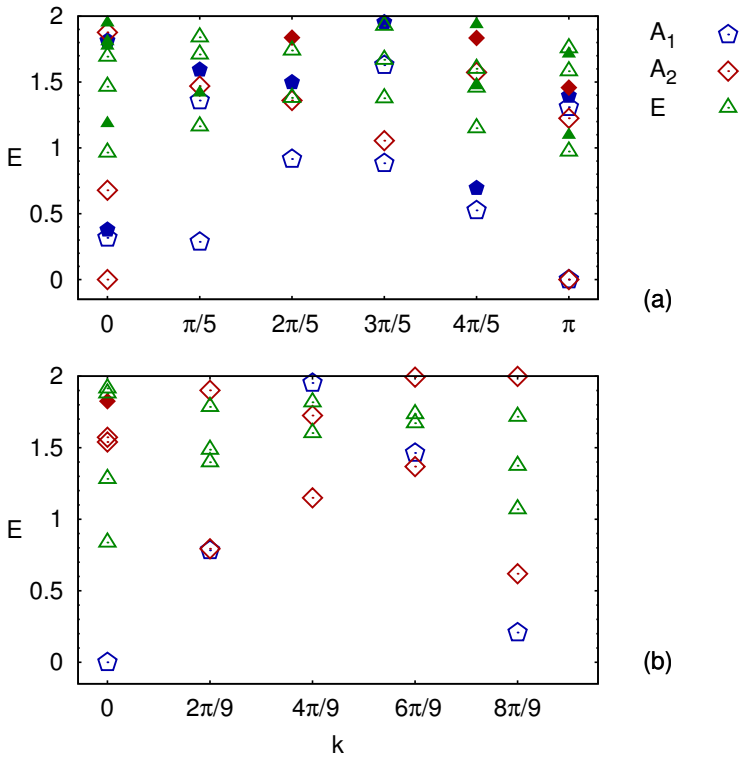

FIGURE 3.5: Results of exact diagonalizion for tubes of 10 (a) and 9 (b) triangles. A_1, A_2 and E are the three irreducible representations of the D_3 symmetry group of a triangle, k is the wave number in the longitudinal direction. Empty symbols denote singlet (S=0), filled symbols denote triplet (S=1) states.

Since the construction of the nearest neighbor valence bond coverings can't explain these ground states, we need to find a new approach. The introduction of a $K_\triangle$ term allows us to study the limiting cases of weakly coupled triangles. The model we consider is

$$\mathcal{H} = K_\triangle \sum_{i=1}^{L} P_i + K_\square \sum_{i=1}^{L} \sum_{j=1}^{3} R_{(i,j)(i+1,j)(i+1,j+1)(i,j+1)}, \tag{3.7}$$

with $R_{(i,j)(i+1,j)(i+1,j+1)(i,j+1)}$ acting on the square plaquettes as explained before in Section 2.3, and P_i acting on the triangles, projecting onto the states where the total spin of the triangle is 3/2. $P_i = (4\mathbf{S}_i^\triangle \cdot \mathbf{S}_i^\triangle - 3)/12$, where $\mathbf{S}_i^\triangle = \sum_{j=1}^{3} \mathbf{S}_{i,j}$ is the total spin operator of the i^{th} triangle. Changing $K_\triangle$ basically changes the intra-triangle coupling allowing us to tune the system between the two weakly coupled limits. By α denoting a four site plaquette, R_α can be written as

$$R_\alpha = (\mathbf{S}_\alpha \cdot \mathbf{S}_\alpha)(\mathbf{S}_\alpha \cdot \mathbf{S}_\alpha - 2)/24 \tag{3.8}$$

where $\mathbf{S}_\alpha = \sum_{(i,j)\in\alpha} \mathbf{S}_{i,j}$ is the total spin operator of the plaquette. As it can be seen, the expansion contains four-spin terms as well. If we expand the full Hamiltonian, it has the form

$$\begin{aligned}\mathcal{H} = \sum_{i=1}^{L}\sum_{j=1}^{3} \Big\{ & J_\perp \mathbf{S}_{i,j}\cdot\mathbf{S}_{i,j+1} + J_1 \mathbf{S}_{i,j}\cdot\mathbf{S}_{i+1,j} \\ & + J_2\left(\mathbf{S}_{i,j}\cdot\mathbf{S}_{i+1,j+1} + \mathbf{S}_{i,j}\cdot\mathbf{S}_{i+1,j-1}\right) \\ & + J_{\mathrm{RE}}\Big[(\mathbf{S}_{i,j}\cdot\mathbf{S}_{i+1,j})(\mathbf{S}_{i,j+1}\cdot\mathbf{S}_{i+1,j+1}) \\ & \quad + (\mathbf{S}_{i,j}\cdot\mathbf{S}_{i,j+1})(\mathbf{S}_{i+1,j}\cdot\mathbf{S}_{i+1,j+1}) \\ & \quad + (\mathbf{S}_{i,j}\cdot\mathbf{S}_{i+1,j+1})(\mathbf{S}_{i,j+1}\cdot\mathbf{S}_{i,j+1})\Big]\Big\},\end{aligned} \tag{3.9}$$

where the intra-triangle $J_\perp = 5K_\square/6 + 2K_\triangle/3$, the inter-triangle $J_1 = 5K_\square/6$ and $J_2 = 5K_\square/12$, and the four-spin interaction $J_{\mathrm{RE}} = K_\square/3$. We set $K_\square = 1$ in the following.

The four spin term is similar to a ring-exchange interaction discussed in Chapter 1 (see Eq. (1.3) and Fig. 1.1), which describes the cyclic permutation of spins around a four-site plaquette, except here all 3 terms have positive signs. For the conventional ring-exchange two of the three terms have positive sign, the third has negative depending on the path of the exchange. If we add all three possible paths of the ring exchange we get the J_{RE} term in (3.9).

3.3.2 Spin-chiral effective model in the $K_\triangle \to \infty$ limit

In the $K_\triangle \gg 1$ limit, the low energy physics is described by the spin-chiral states $|\sigma,\tau\rangle$ defined in Eq. (3.4), and the effective Hamiltonian has the form

$$\mathcal{H}' = \frac{5}{9}\sum_{i=1}^{L}\left(\frac{3}{4} + \hat{\boldsymbol{\sigma}}_i\cdot\hat{\boldsymbol{\sigma}}_{i+1}\right)\left(1 + \hat{\tau}_i^+\hat{\tau}_{i+1}^- + \hat{\tau}_i^-\hat{\tau}_{i+1}^+\right), \tag{3.10}$$

where $\hat{\boldsymbol{\sigma}}_i$ act on the spin-1/2 and $\hat{\tau}_i^\pm$ act on the chirality (pseudospin–1/2) degrees of freedom. From exact diagonalization of the Hamiltonian (3.10) we learn that the excitations are gapped and the system has a doubly degenerate ground state. This ground state can be given analytically as well.

The spin term $\left(\frac{3}{4} + \hat{\boldsymbol{\sigma}}_i\cdot\hat{\boldsymbol{\sigma}}_{i+1}\right)$ gives 0 if the spin degrees of freedom form a singlet, $(|\uparrow_i\downarrow_{i+1}\rangle - |\downarrow_i\uparrow_{i+1}\rangle)$, and 1 if the spins form a triplet. The chirality term $\left(1 + \hat{\tau}_i^+\hat{\tau}_{i+1}^- + \hat{\tau}_i^-\hat{\tau}_{i+1}^+\right)$ gives 0 if the chiralities form a singlet $(|l_i r_{i+1}\rangle - |r_i l_{i+1}\rangle)$, it gives 1 for the $|l_i l_{i+1}\rangle$ and $|r_i r_{i+1}\rangle$ states, and 2 for $|l_i r_{i+1}\rangle + |r_i l_{i+1}\rangle$. Since the original Hamiltonian (3.7) is a sum of projections, $\mathcal{H}'$ has only non-negative eigenvalues, so a state of alternating spin and chirality singlets is a ground state of $\mathcal{H}'$ with 0 energy (see Fig. 3.6). There are two such ground states, denoted by $\left|\Psi_{\mathrm{GS},1}\right\rangle$ and $\left|\Psi_{\mathrm{GS},2}\right\rangle$, breaking the translational invariance of the system.

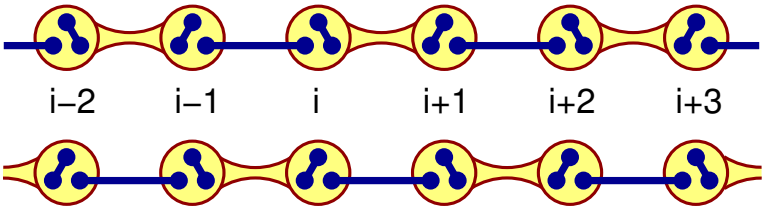

FIGURE 3.6: Schematic drawing of the translational invariance breaking ground states of the spin-chiral effective model $\mathcal{H}'$. The small dots inside the circles denote spin-1/2 sites, the lines stand for the valence bonds. The coloured arcs between two levels denote a chirality singlet $|lr\rangle - |rl\rangle$. These states are exact ground states of the original model for all $K_\triangle \geq 0$ as well.

Kolezhuk et al. [61] also found the ground states $\left|\Psi_{\mathrm{GS},1}\right\rangle, \left|\Psi_{\mathrm{GS},2}\right\rangle$, when studying a more general spin-orbital model, which gives (3.10) as a special case. Similar ground states were also found by [60], who considered a model with $J_\perp, J_1$ and an additional interaction between next nearest triangles. In that case the exact ground states can be given as spin and chirality singlets formed between the same triangles.

3.3.3 Exact ground states for the projection based Hamiltonian on the tube

Considering $\left|\Psi_{\mathrm{GS},1}\right\rangle$ and $\left|\Psi_{\mathrm{GS},2}\right\rangle$ in the full Hilbert space of the Hamiltonian (3.7) reveals that these states are not only ground states of the $K_\triangle \to \infty$ effective model, but of the original $\mathcal{H}$ for all $K_\triangle \geq 0$[1]. It is easy to see, that all the P_i projections are satisfied, since each triangle have a total spin of 1/2. As for the $R_{(i,j)(i+1,j)(i+1,j+1)(i,j+1)}$, $\left|\Psi_{\mathrm{GS},1}\right\rangle$ and $\left|\Psi_{\mathrm{GS},2}\right\rangle$ are superpositions of static valence bond coverings, but interestingly, none of these coverings satisfy all the plaquettes simultaneously by themselves, yet somehow their superposition does.

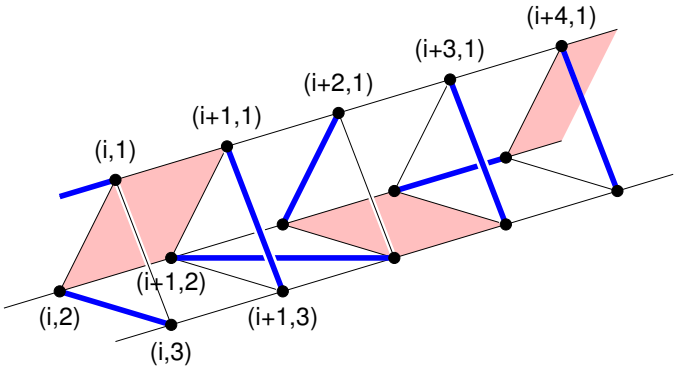

FIGURE 3.7: The spin tube with a snapshot of valence bond covering from the dimerized spin–chiral exact ground state. There is a spin singlet between triangles $i+1$ and $i+2$, $i+3$ and $i+4$ and so on. A chirality singlet is present between triangles i and $i+1$, $i+2$ and $i+3$ and so on. The shaded plaquettes are not satisfied in this particular configuration, and only quantum resonance with other configurations will make all the plaquettes satisfied.

[1] We note that $\left|\Psi_{\mathrm{GS},1}\right\rangle$ and $\left|\Psi_{\mathrm{GS},2}\right\rangle$ are eigenstates of (3.7) for all $K_\triangle$, but they are ground states only for $K_\triangle \geq 0$

Fig 3.7 shows a typical valence bond covering building up these spin-chiral ground states. As it can be seen, the plaquettes belonging to a spin singlet (e.g. between triangles $i+1$ and $i+2$ or between $i+3$ and $i+4$) are all satisfied in each covering in the superposition, but one of the three plaquettes belonging to a chirality singlet are seemingly not (e.g. plaquettes between triangles i and $i+1$ or between $i+2$ and $i+3$). This contradiction can be resolved if we recall that valence bond coverings are usually non-orthogonal, and the subset of these states is overcomplete [2]. The simplest illustration is the set of $|\nu^{\sigma,j}\rangle$ states on a single triangle with a free spin σ at site j and a valence bond between the other two sites, as defined in (3.5). These three $\left|\nu^{\sigma,j}\right\rangle$ states on a triangle are linearly dependent, namely $\left|\nu^{\sigma,1}\right\rangle + \left|\nu^{\sigma,2}\right\rangle + \left|\nu^{\sigma,3}\right\rangle = 0$ (See Fig. 3.8).

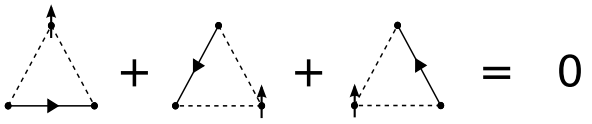

FIGURE 3.8: The linear dependence of the thre $\left|\nu^{\sigma,j}\right\rangle$ states.

This equation provides an explanation to our problem. It tells us that if we can't see a valence bond, it doesn't mean it is not there. In other words, it is not necessary for each plaquette to have a valence bond explicitly in each covering building up the ground state. We can exploit the linear dependency of the $\left|\nu^{\sigma,j}\right\rangle$ to redefine the $|\sigma,\tau\rangle$ states using only $\left|\nu^{\sigma,1}\right\rangle$ and $\left|\nu^{\sigma,2}\right\rangle$:

$$|\sigma_i,\tau_i\rangle = \left(1 - e^{\pm\frac{4\pi i}{3}}\right)|\nu_i^{\sigma,1}\rangle + \left(e^{\pm\frac{2\pi i}{3}} - e^{\pm\frac{4\pi i}{3}}\right)|\nu_i^{\sigma,2}\rangle \tag{3.11}$$

Using this expansion a chirality singlet between the i^{th} and $i+1^{\text{th}}$ triangles is $|l_i r_{i+1}\rangle - |r_i l_{i+1}\rangle = \left|\nu_i^{\sigma_i,1}\nu_{i+1}^{\sigma_{i+1},2}\right\rangle - \left|\nu_i^{\sigma_i,2}\nu_{i+1}^{\sigma_{i+1},1}\right\rangle$ (see Fig. 3.9). One can see that the plaquette between the legs $j=2$ and $j=3$ and the plaquette between legs $j=1$ and $j=3$ contain a singlet bond in both terms. This means that these plaquettes are both satisfied. If we use $\left|\nu^{\sigma,2}\right\rangle$ and $\left|\nu^{\sigma,3}\right\rangle$ in the expansion of $|\sigma_i,\tau_i\rangle$, we can see that the plaquette between legs $j=1$ and $j=2$ is also satisfied.

To summarize, the contradiction between the existence of 0 energy ground states of the Batista-Trugman model (Eq. (2.9) or (3.7) with $K_\triangle = 0$) on the tube, and the fact that no static valence bond covering ground state exists for the three-leg tube can be resolved if we consider that these valence bond coverings are not-orthogonal and form a highly overcomplete subset of the Hilbert space. Tuning the system to the weakly coupled limit provided a viewpoint that helped in identifying the ground states of the original model.

[2] We call a subset of states (highly) overcomplete, if the number of states is (much) larger than the number of linearly independent states in the subset.

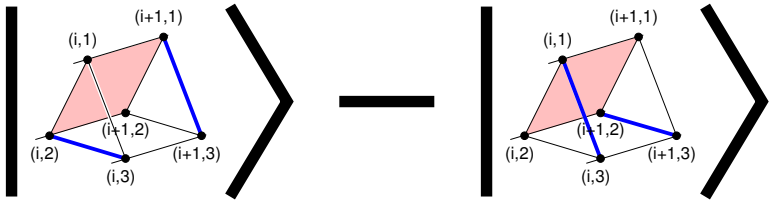

FIGURE 3.9: $|\nu_i^{\sigma_i,1}\nu_{i+1}^{\sigma_{i+1},2}\rangle - |\nu_i^{\sigma_i,2}\nu_{i+1}^{\sigma_{i+1},1}\rangle$, the expansion of a chirality singlet section of the spin-chiral ground states $\left|\Psi_{\mathrm{GS},1}\right\rangle$ and $\left|\Psi_{\mathrm{GS},2}\right\rangle$, if the $|\sigma,\tau\rangle$ states are expanded as in (3.11). The plaquettes between legs j=2 an j=3, and between j=1 and j=3 are clearly satisfied. A similar picture can be drawn if we use $\left|\nu^{\sigma,2}\right\rangle$ and $\left|\nu^{\sigma,3}\right\rangle$ in the expansion of $|\sigma_i,\tau_i\rangle$ only the seemingly unsatisfied plaquettes will be elsewhere, thus we can prove that all plaquettes are always satisfied.

3.4 Domain walls at $K_\triangle = 0$

So far, we have discussed the $K_\triangle \geq 0$ regime of the Hamiltonian (3.7), and found dimerized, translational invariance breaking ground states with gapped excitations. In the following section we will concentrate on the $K_\triangle = 0$ point, where exact diagonalization found three ground state for tubes of even length, and a doublet ground state for odd length tubes. In case of odd length tubes a construction of alternating spin and chirality singlets cannot be implemented due to the periodic boundary conditions. We are facing a similar problem as for the Majumdar-Ghosh model (see section 2.1). In that case a dimerized doubly degenerate exact ground state was found for chains of even length as well, while for the ground state of chains of odd length a dimerized state with a single domain wall was proposed [36]. The low-lying excitations for chains of even length were also given as a pair of domain walls.

Exact diagonalization shows, that a domain wall picture is also realized in our case. Fig. 3.10a-c shows the lowest energy states as we change $K_\triangle$ for tubes of even length. For $K_\triangle > 0$ the ground state is doubly degenerate as we discussed previously. For $K_\triangle \leq 0$, several crossings can be seen before we enter the S=3/2 regime for large negative $K_\triangle$. These crossovers are the sign of some kind of domain walls appearing in the ground state . Our intuition is further confirmed if we check the expectation of $\left\langle \sum_i P_i \right\rangle$ i.e. the number of triangles with a total spin of 3/2 (see Fig 3.10d), where jumps can be seen at the points of energy crossings. As it can be seen $\left\langle \sum_i P_i \right\rangle$ takes non-integer values, meaning that the domain wall structure is more complex than a single $S = 3/2$ triangle (we will give the detailed structure of the domain walls later).

Exact diagonalization for finite tubes of odd length at $K_\triangle = 0$ revealed that the 0 energy doublet ground state is indeed a spin-chiral order with a single domain wall. There are two kinds of domain walls (shown on Fig 3.11), depending on whether we break the dimerized order at spin singlet or a chirality singlet, we denote these domain wall states by $\left|\xi_i^\sigma\right\rangle$ and $\left|\eta_j^\sigma\right\rangle$, respectively.

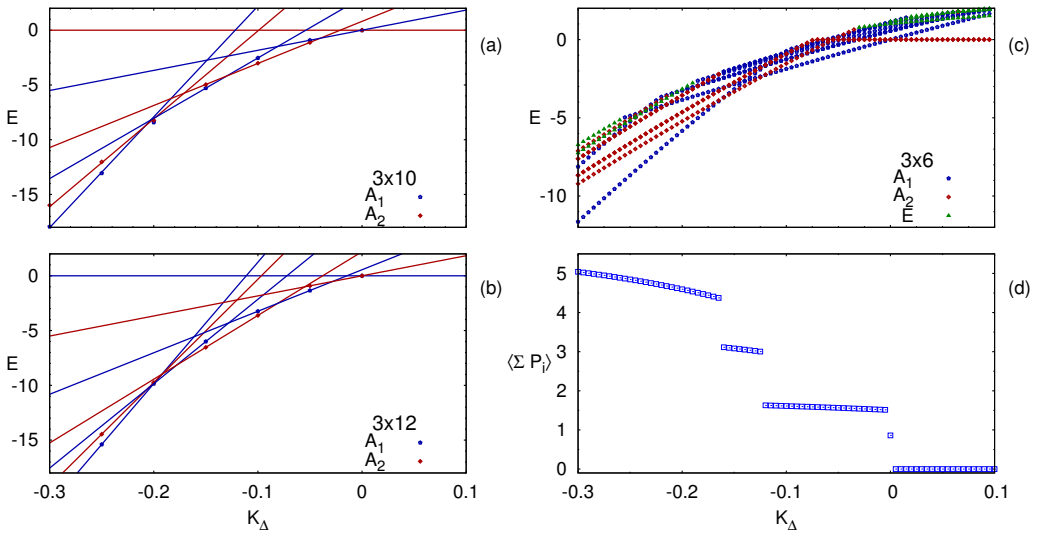

FIGURE 3.10: Energy levels as we change $K_\triangle$ for tubes of different length (a) L=10,(b) L=12,(c) L=6. (d) The number of S=3/2 levels for the 3x6 tube. The crossings in the energy spectrum and the jumps in the number of S=3/2 triangles corresponds to the appearance of pairs of domain walls into the spin-chiral order.

The lower indices stand for the position of the domain wall, while $\sigma = \uparrow, \downarrow$ is a spin-1/2 degree of freedom.

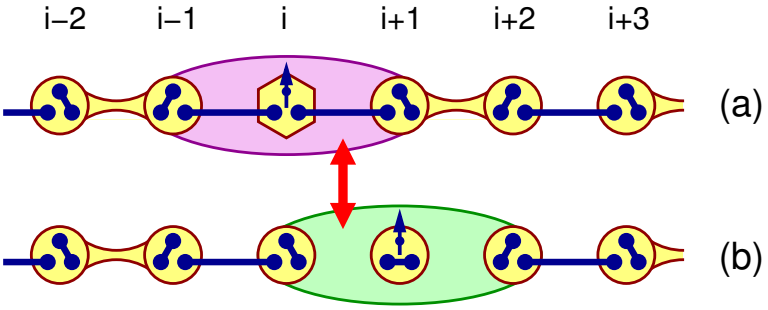

FIGURE 3.11: Single domain walls in tubes of odd length with periodic boundary conditions at $K_\triangle = 0$. (a) If we break the dimerized order at a spin singlet, the domain wall is a S=3/2 triangle(denoted by $\left|\xi_i^\uparrow\right\rangle$, and drawn as a hexagon in the figure) connected by valence bonds to the the neighboring triangles. (b) If the order is broken at a chirality singlet the domain wall is a S=1/2 triangle which forms a $|lll\rangle + |rrr\rangle$ chirality structure with the neighboring triangles, we show $\left|\eta_{i+1}^\uparrow\right\rangle$. In both cases the ellipses show the part of the one domain wall states where the plaquettes are not satisfied with respect to $\mathcal{H}_{K_\triangle=0}$. The arrow emphasizes that the Hamiltonian $\mathcal{H}_{K_\triangle=0}$ has a nonzero matrix element between $\left|\xi_i^\uparrow\right\rangle$ and $\left|\eta_{i+1}^\uparrow\right\rangle$. The domain walls always contain an unpaired spin (denoted by small arrow).

$\left|\xi_i^\sigma\right\rangle$ and $\left|\eta_i^\sigma\right\rangle$ satisfy all R_α in the Hamiltonian, except for those plaquettes that include spins on the i^{th} triangle. These plaquettes are responsible for the non-zero matrix elements for these states. The Hamiltonian connects $\left|\xi_i^\sigma\right\rangle$ to $\left|\eta_{i\pm1}^\sigma\right\rangle$, thus allowing the domain wall to propagate.

The Hamiltonian (3.7) has the following non-zero matrix elements in Fourier space at $K_\triangle = 0$:

$$\begin{aligned}
\left\langle \eta_k^\sigma \right| \mathcal{H} \left| \eta_k^\sigma \right\rangle &= \frac{5}{6}\left(1 - a_L \cos k\right) \\
\left\langle \xi_k^\sigma \right| \mathcal{H} \left| \xi_k^\sigma \right\rangle &= \frac{5}{18}\left(1 - a_L \cos k\right) \\
\left\langle \xi_k^\sigma \right| \mathcal{H} \left| \eta_k^\sigma \right\rangle &= -5\sqrt{3}\left(\cos k - a_L\right),
\end{aligned} \tag{3.12}$$

where $a_L = 8/2^L$ vanishes for $L \to \infty$. Similarly, the overlaps in finite systems are

$$\begin{aligned}
\left\langle \eta_k^\sigma \middle| \eta_k^\sigma \right\rangle &= \left(1 - a_L \cos k\right) \\
\left\langle \xi_k^\sigma \middle| \xi_k^\sigma \right\rangle &= 1 \\
\left\langle \xi_k^\sigma \middle| \eta_k^\sigma \right\rangle &= 0.
\end{aligned} \tag{3.13}$$

Since these domain wall states are not orthonormal, a generalized eigenvalue problem has to be solved to get the variational energies in the single domain wall subspace,

$$\begin{pmatrix} \left\langle \eta_k^\sigma \right| \mathcal{H} \left| \eta_k^\sigma \right\rangle & \left\langle \eta_k^\sigma \right| \mathcal{H} \left| \xi_k^\sigma \right\rangle \\ \left\langle \xi_k^\sigma \right| \mathcal{H} \left| \eta_k^\sigma \right\rangle & \left\langle \xi_k^\sigma \right| \mathcal{H} \left| \xi_k^\sigma \right\rangle \end{pmatrix} \left| \Psi_{\mathrm{1DW}}^{\pm}(k) \right\rangle = E_{\mathrm{1DW}}^{\pm}(k) \begin{pmatrix} \left\langle \eta_k^\sigma \middle| \eta_k^\sigma \right\rangle & \left\langle \eta_k^\sigma \middle| \xi_k^\sigma \right\rangle \\ \left\langle \xi_k^\sigma \middle| \eta_k^\sigma \right\rangle & \left\langle \xi_k^\sigma \middle| \xi_k^\sigma \right\rangle \end{pmatrix} \left| \Psi_{\mathrm{1DW}}^{\pm}(k) \right\rangle . \tag{3.14}$$

This gives the variational energy for the propagating domain wall in the infinite system as

$$E_{\mathrm{1DW}}^{\pm}(k) = \frac{5}{36}\left(4 \pm \sqrt{10 + 6\cos 2k}\right), \tag{3.15}$$

which is a gapless spectrum at $k = 0$ and π. Moreover, for tubes of finite length $E_{1DW}^{-}(k = 0) = 0$ which corresponds to the 0 energy ground state found by exact diagonalization[3]. This ground state can be written as $\left|\Psi_{\mathrm{1DW}}^{-}(k = 0)\right\rangle = \sqrt{3}\left|\xi_{k=0}^\sigma\right\rangle + \left|\eta_{k=0}^\sigma\right\rangle$.

As we mentioned before, in a single domain wall state, all plaquettes are satisfied except the ones which have sites in the triangle at the center of the domain wall(i.e. the i^{th} triangle in case of $\left|\xi_i^\sigma\right\rangle$ or $\left|\eta_j^\sigma\right\rangle$). However, for $\sqrt{3}\left|\xi_i^\sigma\right\rangle + \left|\eta_{i+1}^\sigma\right\rangle$ all three plaquettes between the i^{th} and $i+1^{\text{th}}$ triangle become satisfied. This "resonance" allows us to build up the $|\Psi_{\mathrm{1DW}}\rangle$ ground state, making plaquettes satisfied step by step.

For tubes of even length domain walls can be introduced in pairs. The two domain wall states can be identified by exact diagonalization. Fig. 3.13 shows the types of two domain wall states. As it turns out, the origin of the domain walls is the promotion of a chirality singlet to a triplet, which is then separated into two parts. The variational Hamiltonian over the two domain wall states can be given for arbitrary length, the overlaps and Hamiltonian matrix element between the two domain wall states can be found in Appendix A.

[3]The energy of a variational state is always larger than the ground state energy, $E_{\mathrm{GS}} < \langle\Psi|\mathcal{H}|\Psi\rangle$. So, if we find a variational state with the same energy as the ground state, it will be, in fact a ground state of the full Hamiltonian.

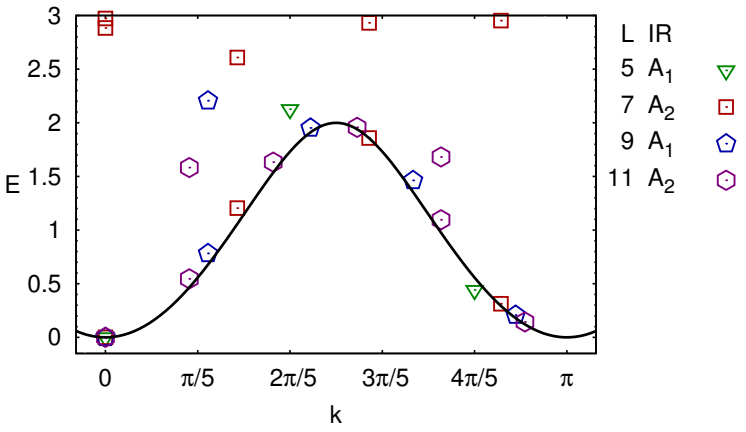

FIGURE 3.12: The variational one domain wall excitation in the infinite limit (solid line), and the corresponding excitations of finite system found by exact diagonalization (open symbols) for tubes of odd length.

The low energy variational excitation spectrum is shown in Fig. 3.14. The independent two domain wall continuum is gapless in the infinite system. In the singlet sector (i.e. when the spins of the two domain walls form a singlet) a bound state appears which touches the lower edge of the continuum at $k = 0$ and π. The domain wall - domain wall correlation function verifies that the bound state is indeed built out of close domain wall terms (See Fig. 3.15).

At $k = \pi$ the variational approach gives a 0 energy state for finite systems already. This state corresponds to the third ground state found by exact diagonalization, and can be described as two deconfined domain walls, the domain wall - domain wall correlation function shows no decay, i.e. the weight of the different terms does not depend on the distance of the domain walls. The explicit form of the two domain wall exact ground state can be found in Appendix A.

Here we should take a moment to compare these findings with the Majumdar-Ghosh model discussed in Sec. 2.1. In both cases dimerized exact ground states were found. However, in our case the domain wall excitations give a gapless spectrum, while for the Majumdar-Ghosh model, two domain wall excitations are gapped (see Fig. 2.1). The presence of a bound state is also a common feature, although it only appears near $k = \pi/2$ in the Majumdar-Ghosh model, while in our case bound state appears right at $k = 0$ and π.

These results are also interesting from the aspect of RVB states. In the infinite limit the two domain wall continuum becomes gapless in both the singlet and triplet sector. This suggests that the infinite system has a short range resonating valence bond ground state, with gapless excitations.

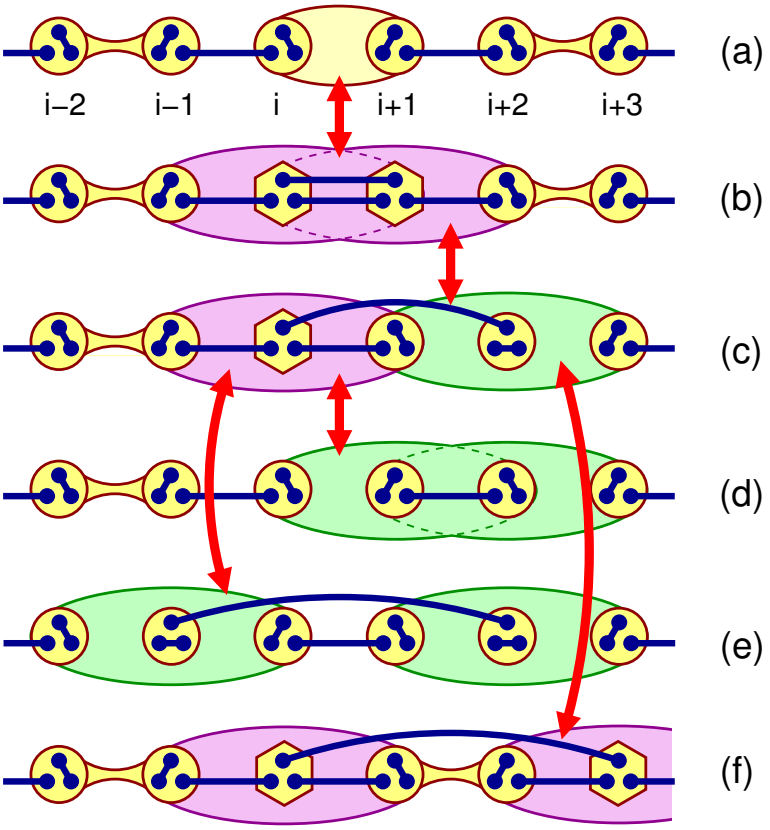

FIGURE 3.13: Relevant two domain wall configurations in the spin singlet sector for L even. In (a) the small ellipse denotes a chirality triplet ($|rl\rangle + |lr\rangle$), that breaks up into two domain walls. (c), (e) and (f) are generally given as $|\xi_i^\uparrow \eta_j^\downarrow - \xi_i^\downarrow \eta_j^\uparrow\rangle$, $|\eta_i^\uparrow \eta_j^\downarrow - \eta_i^\downarrow \eta_j^\uparrow\rangle$, and $|\xi_i^\uparrow \xi_j^\downarrow - \xi_i^\downarrow \xi_j^\uparrow\rangle$, where the domain walls can be arbitrarily separated. (b) and (d) shows overlapping domain walls, (b) is actually $|\xi_i^\uparrow \xi_{i+1}^\downarrow - \xi_i^\downarrow \xi_{i+1}^\uparrow\rangle$, (d) corresponds to $|\eta_i^\uparrow \eta_{i+1}^\downarrow - \eta_i^\downarrow \eta_{i+1}^\uparrow\rangle$, where the chirality configuration is $|llrr\rangle - |rrll\rangle$. Arrows connect states between which the Hamiltonian $\mathcal{H}_{K_\Delta=0}$ has a nonzero matrix element, the position of the arrows corresponds to the position of R_α projections relevant in the overlap.

3.5 Lieb-Schultz-Mattis theorem applied to three-leg spin tube

The Lieb-Schultz-Mattis theorem [37] states that one-dimensional spin systems with SU(2) and translational invariant Hamiltonians, short range interactions and half-integer spin in the unit cell either have gapless excitations or degenerate ground states in the thermodynamic limit. The proof of the theorem is constructive, it states the for a given ground state $|\Psi_0\rangle$ by applying the unitary transformation

$$U_{2\pi} = \exp\left\{ i \frac{2\pi}{L} \sum_{l,n} l S^z_{l,n} \right\} \tag{3.16}$$

$U_{2\pi}|\Psi_0\rangle$ is orthogonal to $|\Psi_0\rangle$ and has an energy $O(1/L)$ compared to the ground state energy. The ground state is either degenerate for finite L already, or a gap closes as $L \to \infty$.

The unitary transformation $U_{2\pi}$ is twisting the spins, in the l^{th} unit cell the spins are rotated by

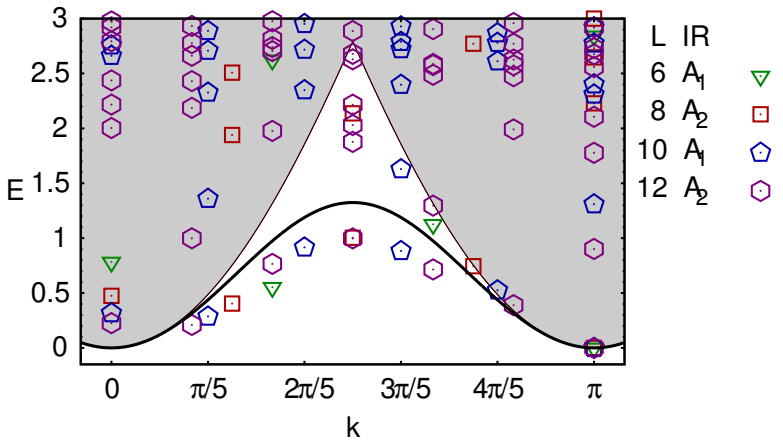

FIGURE 3.14: Low energy two domain wall excitations in the thermodynamic limit compared to ED spectra of small clusters with symmetry compatible with the variational solution. The thick line below the (shaded) continuum is the bound state.

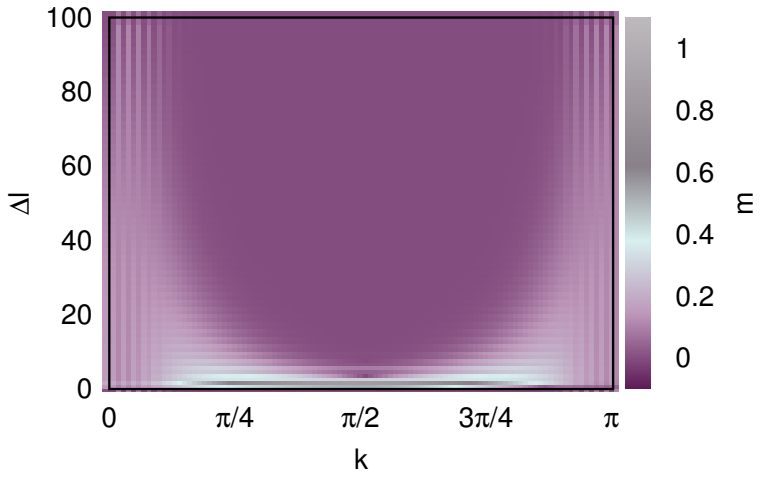

FIGURE 3.15: The domain wall-domain wall correlation function in the bound state of the two domain wall variational spectrum for L=200. The color corresponds to the weight of the component where the distance of the two domain walls is Δl. k stands for the wave number of the bound state. As it can be seen around $k = \pi/2$ the domain walls are close to each other, and the distribution broadens towards $k = 0$ and π.

$2\pi \cdot l/L$ around the S^z axis. Spins in neighboring unit cells are only rotated by a relative angle of $2\pi/L$, thus the energy gain can be proven to be of order $1/L^2$ for an $\mathbf{S}_i\mathbf{S}_{i+1}$ like interaction. For a system with nearest neighbor interactions only this gives an energy difference of $O(1/L)$. If long range interactions are present (i.e. where the interaction length is proportional to the system size), the energy gain is of $O(1)$ and does not disappear in the infinite limit. In general the strength of the interaction should decay faster than $1/r$,where r is the distance of the unit cells, to assure that the energy difference caused by the twisting disappears in the thermodynamical limit.

For half integer spin in the unit cell $TU_{2\pi}T^{-1} = -U_{2\pi}$, where T is the translation operator. This means that if $|\Psi_0\rangle$ is chosen to be an eigenstate of the translational operator (which can be always done, since the Hamiltonian is translational invariant), $|\Psi_0\rangle$ and $U_{2\pi}|\Psi_0\rangle$ will have different eigenvalues with the translation operator, and therefore the two states are orthogonal. The theorem fails for integer spins in the unit cell, since in that case $TU_{2\pi}T^{-1} = U_{2\pi}$ thus $U_{2\pi}|\Psi_0\rangle$ and $|\Psi_0\rangle$ are not necessarily different.

The Lieb-Schultz-Mattis theorem can be applied for the three-leg tube as well, since the unit cell contains three S=1/2 spins. Let us review, how the $U_{2\pi}$ transformation acts on the ground states in the $K_\triangle = 0$ case.

As for the spin-chiral dimerized ground states $U_{2\pi}$ leaves the chirality structure intact since it rotates the spins in the same triangle simultaneously, it only affects the effective spin degrees of freedom,

$$\begin{aligned}\exp\left\{i\frac{2\pi}{L}lS^z_l + i\frac{2\pi}{L}(l+1)S^z_{l+1}\right\}(|\uparrow_l\downarrow_{l+1}\rangle - |\downarrow_l\uparrow_{l+1}\rangle) = \\ = \exp\left\{-i\frac{\pi}{L}\right\}|\uparrow_l\downarrow_{l+1}\rangle - \exp\left\{i\frac{\pi}{L}\right\}|\downarrow_l\uparrow_{l+1}\rangle \\ = |\uparrow_l\downarrow_{l+1}\rangle - |\downarrow_l\uparrow_{l+1}\rangle - i\frac{\pi}{L}(|\uparrow_l\downarrow_{l+1}\rangle + |\downarrow_l\uparrow_{l+1}\rangle) + O(\frac{1}{L^2}).\end{aligned} \tag{3.17}$$

As it can be seen, $U_{2\pi}$ mixes the spin singlets with an $O(1/L)$ triplet component. The only exception is when the singlet is crossing the boundary i.e. $(|\uparrow_L\downarrow_1\rangle - |\downarrow_L\uparrow_1\rangle)$, where an extra -1 factor is introduced,

$$\begin{aligned}\exp\left\{i\frac{2\pi}{L}LS^z_L + i\frac{2\pi}{L}S^z_1\right\}(|\uparrow_L\downarrow_1\rangle - |\downarrow_L\uparrow_1\rangle) = \\ = \exp\left\{i\pi - i\frac{\pi}{L}\right\}|\uparrow_L\downarrow_1\rangle - \exp\left\{-i\pi + i\frac{\pi}{L}\right\}|\downarrow_L\uparrow_1\rangle \\ = -\left(|\uparrow_L\downarrow_1\rangle - |\downarrow_L\uparrow_1\rangle\, i - \frac{\pi}{L}(|\uparrow_L\downarrow_1\rangle + |\downarrow_L\uparrow_1\rangle)\right) + O(\frac{1}{L^2}).\end{aligned} \tag{3.18}$$

Thus, $U_{2\pi}\left|\Psi_{\mathrm{GS},1,2}\right\rangle = \pm\left|\Psi_{\mathrm{GS},1,2}\right\rangle + O(1/L)$, where the -1 factor is applied in the case when a spin-singlet crosses the boundary. By considering translational invariant combination of these states, if we take $|\Psi_0\rangle = \left|\Psi_{\mathrm{GS},1}\right\rangle + \left|\Psi_{\mathrm{GS},2}\right\rangle$, then $U_{2\pi}\left(\left|\Psi_{\mathrm{GS},1}\right\rangle + \left|\Psi_{\mathrm{GS},2}\right\rangle\right) = \left|\Psi_{\mathrm{GS},1}\right\rangle - \left|\Psi_{\mathrm{GS},2}\right\rangle + O(1/L)$, and the the two states have different eigenvalues (1 and -1) with respect to the T translation. These spin-chiral ground states illustrate the case of the LSM-theorem, where the ground state is already degenerate for finite systems.

If we consider the two-domain wall ground state, denoted by $|\Psi_{2DW}\rangle$, it is not connected to the dimerized $\left|\Psi_{\mathrm{GS},1}\right\rangle, \left|\Psi_{\mathrm{GS},2}\right\rangle$ ground states by $U_{2\pi}$, since it belongs to a different irreducible representation of D_3. $|\Psi_{2DW}\rangle$ has a wave number $k = \pi$, so if we apply $U_{2\pi}$ the resulting state will be at $k = 0$, this means that a gap is closing at $k = 0$, which is in agreement with the two

domain wall variational and finite size ED calculations (See Fig. 3.14 as the lowest energy state at k=0 approaches to 0 as increasing the system size).

3.6 $K_\triangle < 0$ case, an intermediate phase, S=3/2 regime

At the$K_\triangle = 0$ point, three ground states are present for even length tubes, but changing $K_\triangle$ lifts this degeneracy. If we denote the energy of the dimerized ground states by $E_{0\mathrm{DW}}$ and the energy of the two-domain wall ground state as $E_{2\mathrm{DW}}$, the derivative of the energies can be given exactly at this point using the Hellman-Feynmann theorem [4]: $\delta E_{2\mathrm{DW}}/\delta K_\triangle = 3/2$, while $\delta E_{0\mathrm{DW}}/\delta K_\triangle = 0$.

This indicates that for small negative $K_\triangle$ values the two-domain wall state will become the only ground state. As we further decrease $K_\triangle$, several level crossings can be seen as more and more domain walls are introduced to the system. Eventually we enter the S=3/2 regime. Finite size scaling analysis of the transition points shows that the transition from the intermediate phase to the effective S=3/2 regime takes place at $K_\triangle \approx -0.23$. This intermediate phase is novel in the spin tubes. Previous studies didn't find any explicit sign of a third phase between the spin-chiral and S=3/2 limit, and interpreted the transition as a first order phase transition [52, 53].

For $K_\triangle \lesssim -0.23$ the system can be described by an effective S=3/2 model

$$\mathcal{H}'' = \sum_i \left[\frac{45}{32} + \frac{7}{12} \tilde{\mathbf{S}}_i \cdot \tilde{\mathbf{S}}_{i+1} + \frac{1}{18} \left(\tilde{\mathbf{S}}_i \cdot \tilde{\mathbf{S}}_{i+1} \right)^2 \right] \tag{3.19}$$

According to exact diagonalization results this model is adiabatically connected to the simple Heisenberg chain in accordance with the findings of Fridman et al. [62].

3.7 Conclusion

In this chapter we discussed the implementation of the model of Batista and Trugman [47] to the three-leg spin tube. The model can be given as a sum of projection operators. The ground states constructed as nearest neighbor valence bond coverings, found in the square lattice, can not be accommodated in the tube, yet exact diagonalization found 0 energy ground states. Actually, for tubes of even length we found three ground states. This degeneracy can be lifted by changing the intra triangle coupling. In the strongly antiferromagnetic limit ($K_\triangle \gg 1$) two of the three ground states remain. These states can be described as dimerized states of alternating spin and chirality singlets in the effective low energy description. In the projection operator picture these ground

[4] The Hellmann-Feynman theorem says, that if the Hamiltonian depends on some variable λ, the derivative of the energy of an eigenstate can be given as $\frac{\delta E}{\delta \lambda} = \langle \Psi_\lambda | \frac{H_\lambda}{\delta \lambda} | \Psi_\lambda \rangle$. In our case $\frac{H_\lambda}{\delta K_\triangle}\Big|_{K_\triangle = 0} = \sum_i P_i$.

states can be explained by considering the non-orthogonality of the valence bond coverings. The ground states found in tubes of odd length, and the third ground state for even length tubes at $K_\triangle = 0$ can be given as gapless one or two domain wall excitations, respectively.

The $K_\triangle = 0$ case is a quantum critical point, separating the spin-chiral phase ($K_\triangle > 0$) and an intermediate phase where pairs of domains walls are introduced into the system ($-0.23 < K_\triangle < 0$). If we further decrease $K_\triangle$, the system enters an S=3/2 regime, where the low energy effective Hamiltonian can be given as a bilinear biquadratic S=3/2 model, which is adiabatically connected to the S=3/2 Heisenberg model. The phase transition between the intermediate and the S=3/2 phase seems to be of first order, since a macroscopic change in number of S=3/2 triangles takes place.

The model we considered is novel, since it explicitly shows an intermediate phase between the spin-chiral and S=3/2 phases. The phase transition point between the spin-chiral and intermediate phase ($K_\triangle = 0$) is exactly given by the Batista-Trugman Hamiltonian, while the phase transition point to the S=3/2 phase can be estimated by finite sizes scaling of exact diagonalization results. Previous studies didn't find any explicit sign of an intermediate phase and interpreted the transition between the spin-chiral and S=3/2 phases as a first order phase transition [52, 53]. This shows that the upon turning off the four-spin ring exchange interactions the intermediate phase disappears, although the details of this transition require further analysis.

Preliminary numerical results show that the general case of tubes with odd number of legs is similar to the three-leg case. Exact diagonalization for five-leg tubes (with length $L = 4, 5, 6$) also shows 0 energy ground states for the Batista-Trugman point, 3 singlet ground state for tubes of even length and an S=1/2 doublet for tubes of odd length.

The physics of tubes with higher number of legs is not so well established in the literature [63]. The energy spectrum of a separated polygon is more complex than it was for a triangle, the weakly coupled limits provide limited guidance in identifying the ground states. Also, the increasing number of legs restrains the number of coupled polygons which can be simulated by exact diagonalization. All these make the description of exact ground states challenging. Nonentheless, these results suggest, that the Batista-Trugman model for the two dimensional square lattice is in fact a quantum critical point, which makes this model even more interesting, and the general description of the non-trivial (i.e. non static valence bond crystal) ground states a worthy goal to pursue.

Chapter 4

Introduction to SU(N) physics

4.1 Introduction

For the SU(2) symmetric S=1/2 Heisenberg model each spin can be in two states, ↑ or ↓, and the interaction can be rewritten as

$$\mathbf{S}_i \cdot \mathbf{S}_j = \frac{1}{2} P_{ij}^{(2)} - \frac{1}{4}, \tag{4.1}$$

where P_{ij} exchanges the spin states on sites i and j. By this analogy, an SU(N) symmetric Heisenberg interaction can be introduced for systems where the fundamental SU(N) spins on each site can have N states, or – as we will refer to it later – colors.

If we consider the SU(2) symmetric, S=1 Heisenberg model, every spin can have three states (S^z= +1, 0, −1), but the interaction is not SU(3) symmetric since these S^z states are not equivalent, for example the $\mathbf{S} \cdot \mathbf{S}$ interaction does not connect the $S^z = 1$ and $S^z = -1$ states. However, if we allow for biquadratic interactions as well, we can create an SU(3) symmetric model for the S=1 spin system,

$$\left(\mathbf{S}_i \mathbf{S}_j\right) + \left(\mathbf{S}_i \mathbf{S}_j\right)^2 - 1 = P_{ij}^{(3)}. \tag{4.2}$$

Another example can be given as a special case of the Khugel-Khomskii spin-orbital Hamiltonian, that we already mentioned in Chapter 1. On every site the number of possible states is 4: the spin can be ↑ or ↓, and the orbitals can take two possible values as well (denoted by a and b). At special values of coupling constants this model possesses SU(4) symmetry so that

$$\left(2\mathbf{S}_i \mathbf{S}_j + \frac{1}{2}\right)\left(2\boldsymbol{\tau}_i \boldsymbol{\tau}_j + \frac{1}{2}\right) = P_{i,j}^{(2)}(S) P_{i,j}^{(2)}(\tau) = P_{ij}^{(4)}, \tag{4.3}$$

where $\mathbf{S}_i$ acts on the spin and $\boldsymbol{\tau}_i$ acts on the orbital degrees of freedom. The spin term exchanges the spin states on the two sites, while the orbital term exchanges the orbital degrees of freedom.

In the above examples it is clear , that the $P_{ij}^{(N)}$ interaction is SU(N) symmetric (N=2,3 and 4 respectively), since no matter how we transform the onsite color states, the exchange interaction will be left unchanged.

SU(N) models also arise in the Mott insulating state of ultra-cold alkaline-earth atoms trapped in optical lattices. In these systems, the nuclear spin of length F becomes the only relevant degree of freedom with N = 2F+1 states, and the interaction leads to the SU(N) symmetric Heisenberg models [30, 64–66].

Of course the physics of SU(N) systems is much wider, and it requires a thorough introduction to group theory and representation theory as well, here we will only restrict to briefly mention some of the basics to help placing our work in context.

4.2 Irreducible representations of the SU(N) group

4.2.1 Fundamental irreducible representation of the SU(2) group

The principal building block of the SU(2) physics in condensed matter is the electron spin, which is thought as an intrinsic magnetic moment of an electron. Historically the first experiment to prove the quantized nature of the spin was the famous Stern-Gerlach experiment [67, 68]. In this experiment a beam of neutral silver atoms were led into an inhomogenous magnetic field, where the particles are deflected due to their magnetic moment. Stern and Gerlach tried to prove the quantized nature of the angular momentum as predicted by the Bohr-Sommerfeld model, however, in the view of the modern quantum mechanics we know that the splitting was caused by the spin of the unpaired 4s electron [69], as the angular momentum of the silver atom is L=0 (it has a closed 3d and a half filled 4s band).

So, the Stern-Gerlach experiment showed, that spin components in any direction are quantized, and can take two values. Selecting this direction along the z-axis, S^z, i.e. the operator measuring the z component of the spin, has two eigenvalues $+1/2$ and $-1/2$, with the two eigenstates denoted by $|\uparrow\rangle$ and $|\downarrow\rangle$, respectively. In this basis a general spin state can be represented by two complex numbers $c_\uparrow$ and $c_\downarrow$, $\left|\Psi(c_\uparrow, c_\downarrow)\right\rangle = c_\uparrow|\uparrow\rangle + c_\downarrow|\downarrow\rangle$, with a restriction on normalization $|c_\uparrow|^2 + |c_\downarrow|^2 = 1$. The transformations, i.e. rotations of the spin state are then represented by 2×2 unitary matrices, which form the SU(2) group and can be given as

$$U(\mathbf{n}, \phi) = \exp\left[i\phi(S^x \cdot n_x + S^y \cdot n_y + S^z \cdot n_z)\right], \tag{4.4}$$

where (n_x, n_y, n_z) is a unit vector, ϕ is a real number, and S^x, S^y and S^z are the infinitesimal generators of the SU(2) group. These three generators are in fact the matrices of the three

components of the spin operator in the $|\uparrow\rangle$, $|\downarrow\rangle$ basis,

$$S^x = \frac{1}{2}\begin{pmatrix} 0 & 1 \\ 1 & 0 \end{pmatrix} \quad S^y = \frac{1}{2}\begin{pmatrix} 0 & -i \\ i & 0 \end{pmatrix} \quad S^z = \frac{1}{2}\begin{pmatrix} 1 & 0 \\ 0 & -1 \end{pmatrix}. \tag{4.5}$$

The $U(\mathbf{n}, \phi)$ unitary transformation can be interpreted as a rotation of the spin around the direction $\mathbf{n}$ by an angle of ϕ. The matrices in Eq. (4.5) without the 1/2 factor are also known as the Pauli-matrices.

The three spin operators fulfill the commutation relations

$$\left[S^\alpha, S^\beta\right] = i\epsilon_{\alpha\beta\gamma}S^\gamma, \tag{4.6}$$

where α, β, γ can take values of x, y, z, or $1, 2, 3$. $\epsilon_{\alpha\beta\gamma}$ is the totally antisymmetric tensor, or also known as the three-dimensional Levi-Chivita tensor. The length of a single spin is $(S^x)^2 + (S^y)^2 + (S^z)^2 = \mathcal{I} \cdot 3/4$, which commutes with all three generators ($\mathcal{I}$ is the identity operator).

4.2.2 Higher dimensional SU(2) irreducible representations

If we consider multiple electron spins, the Hilbert space breaks into subspaces based on the length of the total spin, for example if we consider 2 electrons, the length of the total spin can be $S_t = 1$ or $S_t = 0$. The spin operators of the total spin are given as $S_t^\alpha = S_1^\alpha + S_2^\alpha$, and $(S_t^x)^2 + (S_t^y)^2 + (S_t^z)^2 = S_t(S_t + 1)$. The $S_t = 1$ subspace is three-dimensional, while the $S_t = 0$ subspace is one-dimensional.

$$\begin{aligned}
\left|S_t = 1, S_t^z = \quad 1\right\rangle &= |\uparrow,\uparrow\rangle \\
\left|S_t = 1, S_t^z = \quad 0\right\rangle &= \frac{1}{\sqrt{2}}|\uparrow,\downarrow\rangle + \frac{1}{\sqrt{2}}|\downarrow,\uparrow\rangle \\
\left|S_t = 1, S_t^z = -1\right\rangle &= |\downarrow,\downarrow\rangle
\end{aligned} \tag{4.7}$$

$$\left|S_t = 0, S_t^z = \quad 0\right\rangle = \frac{1}{\sqrt{2}}|\uparrow,\downarrow\rangle - \frac{1}{\sqrt{2}}|\downarrow,\uparrow\rangle$$

where S^t stands for the length and S_t^z for the z component of the total spin. The simultaneous rotations of the spins can be given by unitary transformations, however the matrices in this case are reducible into a 3 and a 1 dimensional part according to the value of S_t. In the $S_t = 1$ subspace the unitary transformations can be represented by 3×3 matrices and can be formally

given similarly as in (4.4) with the $S = 1$ spin operators.

$$S^x = \frac{1}{\sqrt{2}}\begin{pmatrix} 0 & 1 & 0 \\ 1 & 0 & 1 \\ 0 & 1 & 0 \end{pmatrix} \quad S^y = \frac{1}{\sqrt{2}}\begin{pmatrix} 0 & -i & 0 \\ i & 0 & -i \\ 0 & i & 0 \end{pmatrix} \quad S^z = \begin{pmatrix} 1 & 0 & 0 \\ 0 & 0 & 0 \\ 0 & 0 & -1 \end{pmatrix} \tag{4.8}$$

These generators, and the $U(\mathbf{n}, \phi)$ transformations give a three dimensional irreducible representation of the SU(2) group. The one-dimensional matrices of the $S_t = 0$ subspace are the trivial representation of the SU(2) group, as all one-dimensional transformation matrices are identically 1. This means that the $S_t = 0$ state is invariant under the simultaneous rotation of the spins.

If we consider more electron spins we can get higher dimensional irreducible representations of the SU(2) group. The total spin can be a multiple of 1/2 (S_t=1/2, 1, 3/2, 2 ...), and the dimension of the matrices of the spin operators is $2S_t + 1$.

In materials which exhibit localized spin degrees of freedom with spins larger than $1/2$, multiple electrons are present in the highest occupied, partially filled orbitals and the Hund energy causes their spins to align. An example is the $CaMnO_3$. The crystal field of the octahedral O environment splits the 3d orbitals of Mn into e_g and t_{2g} levels. The three $3d$ electrons of the Mn^{4+} occupy the t_{2g} levels with parallel spins to minimize the Hund energy. This configuration results an effective $S = 3/2$ spin without any orbital degeneracy [70].

4.2.3 SU(N) spins

In the general SU(N) case the elementary building block can be imagined as a spin with N possible states, or colors, denoted by α. A general state can be given as $|\Psi\rangle = \sum_\alpha c_\alpha |\alpha\rangle$. The transformations of an elementary SU(N) spin can be represented by $N \times N$ unitary matrices, which form the SU(N) group. A set of infinitesimal generators can be chosen as the operators $S^\alpha_\beta = |\alpha\rangle \langle\beta|$ that change the color of the spin. These generators fulfill the following commutation relations

$$\left[S^\alpha_\beta, S^\gamma_\delta\right] = \delta^\gamma_\beta S^\alpha_\delta - \delta^\alpha_\delta S^\gamma_\beta, \tag{4.9}$$

where $\alpha, \beta, \gamma, \delta$ can take values from 1 to N. Since $\sum_\alpha S^\alpha_\alpha = \mathcal{I}$ is the identity, the number of independent generators is $N^2 - 1$.

With this notation the conventional SU(2) spin-1/2 operators can be expressed as $S^x = (S^1_2 + S^2_1)/2$, $S^y = (S^1_2 - S^2_1)/(2i)$ and $S^z = (S^1_1 - S^2_2)/2$.

Again, emphasizing the analogy to the SU(2) case, if we consider multiple elementary SU(N) spins, more complex SU(N) objects can be constructed. The addition rules of SU(N) spins

can be illustrated by Young-tableaux, which provide a systematic way to collect the possible irreducible representations of the compound spin. The simplest case is the addition of two fundamental SU(N) spins, which can either form a symmetric (N(N+1)/2 dimensional subspace) or antisymmetric pair (N(N-1)/2 dimensional subspace). If a single fundamental spin is represented by a square, the symmetric and antisymmetric pair of two spins can be represented by two squares aligned in a row or in a column respectively.

If we consider 3 fundamental spins, the three spins can be in totally symmetric state (represented by three squares in a row), a totally antisymmetric configuration (three squares in a column), or a mixed state, which is represented by two squares in a row, and the third square in the next row (see Table 4.1).

site irreps	Young tableau	wave functions	degeneracy
$\square\otimes\square$	$\begin{smallmatrix}\square\\\square\end{smallmatrix}$	$\|\alpha\beta\rangle - \|\beta\alpha\rangle$	3
	$\square\square$	$\|\alpha\alpha\rangle$ $\|\alpha\beta\rangle + \|\beta\alpha\rangle$	6
$\square\otimes\square\otimes\square$	$\begin{smallmatrix}\square\\\square\\\square\end{smallmatrix}$	$\begin{pmatrix}\|\alpha\beta\gamma\rangle + \|\gamma\alpha\beta\rangle + \|\beta\gamma\alpha\rangle \\ -\|\alpha\gamma\beta\rangle - \|\beta\alpha\gamma\rangle - \|\gamma\beta\alpha\rangle\end{pmatrix}$	1
	$2\times\begin{smallmatrix}\square\square\\\square\end{smallmatrix}$	$\|\alpha\alpha\beta\rangle - \|\beta\alpha\alpha\rangle - \|\alpha\beta\alpha\rangle$ $\begin{pmatrix}\|\alpha\beta\gamma\rangle - \|\gamma\alpha\beta\rangle - \|\beta\gamma\alpha\rangle \\ -\|\alpha\gamma\beta\rangle + \|\beta\alpha\gamma\rangle - \|\gamma\beta\alpha\rangle\end{pmatrix}$	2×8
	$\square\square\square$	$\|\alpha\alpha\alpha\rangle$ $\|\alpha\alpha\beta\rangle + \|\beta\alpha\alpha\rangle + \|\alpha\beta\alpha\rangle$ $\begin{pmatrix}\|\alpha\beta\gamma\rangle + \|\gamma\alpha\beta\rangle + \|\beta\gamma\alpha\rangle \\ +\|\alpha\gamma\beta\rangle + \|\beta\alpha\gamma\rangle + \|\gamma\beta\alpha\rangle\end{pmatrix}$	10

TABLE 4.1: The addition rules of 2 and 3 fundamental SU(3) spins. Two spins can form an antisymmetric or a symmetric pair, illustrated by a Young tableaux with 2 squares in a column or a 2 squares in a row, respectively. In case of 3 fundamental spins, the fully symmetric subspace (three squares in a row) is 10 dimensional. There are two independent, partially symmetrized subspaces (two squares in a row, and the third one in the next row), depending on which two positions are symmetrized (the third case is linearly dependent of the other two) , in the table we took examples where symmetrization is made between the first and second position, and any exchange with the third spin is antisymmetric. Finally, the totally antisymmetric case (three squares in a column) is non-degenerate , and it is called an SU(3) singlet state.

For the SU(2) case two fundamental spins can form an antisymmetric pair or singlet, which is invariant under the spin rotations. In the SU(3) case 3 spins are needed to form a totally antisymmetric singlet state, which is invariant under the rotations. Similarly, in the SU(N) case N fundamental spins can form a singlet. Like the formation of valence bonds in the SU(2) case (see Chapter 1), the formation of singlets is an important aspect of the SU(N) physics [71, 72].

A wide variety of models can be created with more complex SU(N) spins on the sites [73–75]. In case when the spin on each site can be represented by a Young-tableau of one row and M

columns – i.e. M symmetrized fundamental spins are present at each site – a bosonic approach naturally arises. A spin can be represented by M bosons, and the spin operators can be written as $S^{\alpha}_{\beta}(i) = b^{\dagger}_{\alpha}(i)b_{\beta}(i)$, where $b^{\dagger}_{\alpha}(i)$ ($b_{\alpha}(i)$) creates (annihilates) a boson with color α on site i, and the usual bosonic commutation relations apply.

Similarly, in case when the spins on each site correspond to a Young-tableu with one column and M rows, i.e. M anitisymetrized fundamental spins are present at each site ($M \leq N$) a spin can be represented by M fermions and the spin operators read as $S^{\alpha}_{\beta}(i) = f^{\dagger}_{\alpha}(i)f_{\beta}(i)$, where $f^{\dagger}_{\alpha}(i)$ ($f_{\alpha}(i)$) creates (annihiliates) a fermion with color α on site i.

In this work we will only consider models where fundamental, N dimensional spins are placed on each site. In this case both a fermionic and bosonic representation of the model is possible.

4.3 SU(N) symmetric models, numerical methods

A system is SU(N) symmetric, if the Hamilton operator is invariant under the simultaneous rotation of all spins, i.e. it commutes with all the spin operators of the total spin, $\sum_j S^{\alpha}_{\beta}(j)$. Such operators are called Casimir operators [76], the simplest non-trivial, or so-called first Casimir operator can be given as $C(\Lambda) = \sum_{\alpha,\beta} S(\Lambda)^{\alpha}_{\beta} S(\Lambda)^{\beta}_{\alpha}$, where $S(\Lambda)^{\alpha}_{\beta}$ are the total spin operators of an arbitrary subsystem Λ. The Heisenberg exchange mentioned in the introduction can be derived from these Casimir operators, since

$$P_{ij} = \sum_{\alpha,\beta} S(i)^{\alpha}_{\beta} S(j)^{\beta}_{\alpha} = \frac{1}{2}\left(C(\{i,j\}) - C(\{i\}) - C(\{j\})\right), \tag{4.10}$$

where $\{i, j\}$ is the subsystem of two spins on sites i and j, while $\{i\}$ and $\{j\}$ are subsystems with one spin. In the SU(2) case the first Casimir operator is the square of total spin of the subsystem Λ, ($C(\Lambda) = 2\mathbf{S}(\Lambda)^2 + 1/2$) and the conventional Heisenberg interaction can be written as

$$\begin{aligned} \mathbf{S}(i)\mathbf{S}(j) &= \frac{1}{2}\left((\mathbf{S}(i) + \mathbf{S}(j))^2 - \mathbf{S}(i)^2 - \mathbf{S}(j)^2\right) \\ &= \frac{1}{2} S_t(S_t + 1) - S(S + 1), \end{aligned} \tag{4.11}$$

where S_t is the length of total spin on sites i and j, and S is the length of the spins separately.

4.3.1 Classical approach, flavor wave theory

In the SU(2) case the classical approach was the first step in understanding spin systems, where spins were treated as three dimensional classical vectors. This approach was more accurate for longer spins. A similar approach can be done in the general SU(N) case as well. A site factorized

wave function is the closest to the classical case, as there is no entanglement between the spins. This site factorized approach becomes exact when the spins correspond to Young-tableaux with one row and M columns as $M \to \infty$, although it can often provide valuable insight into systems with finite M (even M=1). The site factorized wave function in the fundamental SU(N) model has the form

$$|\Psi\rangle = \prod_i |\Psi(i)\rangle\,, \tag{4.12}$$

where $\Psi_i = \sum_\alpha c_\alpha(i)\,|\alpha\rangle$ is the local state of the spin at site i. The energy of a Heisenberg exchange in this approximation is

$$\langle\Psi|\,P_{ij}\,|\Psi\rangle = \left\langle\Psi_j|\Psi_i\right\rangle\left\langle\Psi_i|\Psi_j\right\rangle = \left|\left\langle\Psi_i|\Psi_j\right\rangle\right|^2, \tag{4.13}$$

which is clearly non-negative, thus the lowest possible energy of the whole system is 0, which can be reached if the two local states at i and j are orthogonal for all $\langle i, j\rangle$ bonds.

In the SU(2) case this can be done for bipartite lattices like the square or the honeycomb lattice resulting the two sublattice Néel-order, which is unique apart from global SU(2) rotations. For the triangular lattice we can't satisfy all the bond simultaneously, because the local Hilbert space is only two dimensional, and the three states around a triangle can't be all orthogonal to each other. As a compromise, the classical ground state is the three-sublattice, 120° spin configuration. However, for the SU(3) case a zero energy classical ground state can be achieved for the triangular lattice, shown in Fig. 4.1a, which is the analogue of the SU(2) Néel-order and it is unique up to a global SU(3) rotation. For the square lattice the number of fully color ordered classical ground states is macroscopic in the SU(3) case, while for the triangular lattice the number of classical color ordered ground states becomes macroscopic in the SU(4) model. The more colors are allowed, the more possibilities are available to cover the lattice without having two neighboring sites with the same color.

The degeneracy of the classical ground state manifold is certainly split in the quantum model. One can adapt the linear spin-wave theory used in SU(2) systems to the SU(N) case, leading to the linear flavor-wave theory (LFWT)[1] [77]. In this approach we consider fluctuations in the bosonic representation of the site factorized ground state. The spectrum, and so the zero point energy of the resulting harmonic excitations depends on the underlying classical ground state, therefore it can lift the macroscopic degeneracy (order by disorder). These linear-flavor wave corrections prefer states where the next-nearest neighbors are also orthogonal, i.e. they have different colors in the color ordered case. For the square lattice in the SU(3) case a striped three-sublattice configuration has the lowest zero-point energy [78] (shown in Fig. 4.1b), while for the SU(4) model linear-flavor wave theory predicts a color ordered state where the corrections show smaller bond energies around separated square plaquettes [79] (See Fig. 4.1c).

[1] The different colors may also be called flavors.

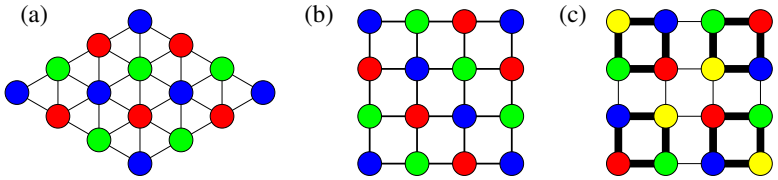

FIGURE 4.1: (a) The three sublattice order in the SU(3) triangular lattice. (b) The striped three sublattice order in the SU(3) square lattice selected by linear flavor wave corections. (c) The color ordered state with smaller bond energies around squares, which is predicted by flavor-wave theory for the SU(4) square lattice.

For the honeycomb lattice the classical ground state is macroscopically degenerate in the SU(3) and SU(4) case as well. Linear-flavor wave corrections for the SU(3) model predict a dimerized color-ordered state [80] (See Fig. 4.2a). The SU(4) case is more interesting. LFWT corrections still allow a macroscopic degeneracy in the ground state. The honeycomb lattice can be covered in a way that all nearest and next-nearest spins have different colors. The most symmetric case is shown in Fig. 4.2b. If one exchanges the colors along a stripe, the resulting state will have the same energy even after considering the zero point energy of LFWT, which allows for an $O(2^L)$ degeneracy, where L is the linear size of the system. This makes the honeycomb lattice a promising candidate to accommodate a spin-liquid ground state [81].

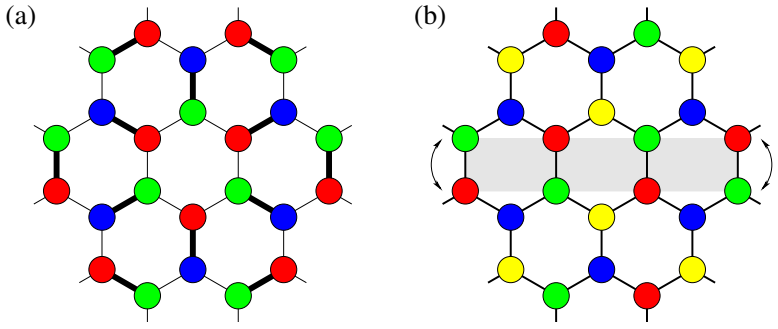

FIGURE 4.2: (a) The color ordered state with dimerized bonds found by linear flavor wave theory for the SU(3) honeycomb lattice. (b) LFWT just partially lifts the degeneracy for the SU(4) case, one can exchange colors along a stripe, which leads to a degeneracy of order of 2^L, where L is the linear size of the system.

4.3.2 Fermionic mean-field approach and Gutzwiller projection

Up to this point we made the assumption that the ground state can be described as a classically ordered state and the quantum corrections are the zero point energy of flavor waves. However, other approaches might predict a different type of ground state.

For example, instead of the bosonic representation of the spins, we could start with the fermionic representation of the colors. i.e. we picture the system as a lattice gas with N different fermions

corresponding to the N different colors, and restrict the number of fermions at each site to one. In this picture the Hamiltonian has the form

$$\mathcal{H} = \sum_{\langle i,j \rangle} P_{i,j}^{(N)} = \sum_{\langle i,j \rangle} f_{i,\alpha}^{\dagger} f_{i,\beta} f_{j,\beta}^{\dagger} f_{j,\alpha} \tag{4.14}$$

where $f_{i,\alpha}^{\dagger}$ ($f_{i,\alpha}$) creates (annihilates) a fermion with color α at site i. Repeated flavor indices are summed over all possible colors, and the usual fermionic anticommutation relations stand. The Hamiltonian can be transformed as

$$\mathcal{H} = zN_f - \sum_{\langle i,j \rangle} f_{j,\beta}^{\dagger} f_{i,\beta} f_{i,\alpha}^{\dagger} f_{j,\alpha} \tag{4.15}$$

where z is the coordination number, and N_f is the total number of fermions (i.e. number of sites for the fundamental SU(N) model) in the system. Here we can make a mean field approximation estimating $f_{i,\alpha}^{\dagger} f_{j,\alpha}$ by its expectation value $\chi_{i,j} \equiv \left\langle f_{i,\alpha}^{\dagger} f_{j,\alpha} \right\rangle$ and keeping only the linear terms of the fluctuations. The mean field Hamiltonian has the form

$$\mathcal{H}_{MF} = zN_f + \sum_{\langle i,j \rangle} \left[\left| \chi_{i,j} \right|^2 - \left(f_{j,\beta}^{\dagger} f_{i,\beta} \chi_{i,j} + h.c. \right) \right] \tag{4.16}$$

At this point one can proceed by solving the free fermionic Hamiltonian self-consistently in $\chi_{i,j}$ [74]. The one fermion per site occupancy can be enforced by adding Lagrange multiplier terms for each site [82].

A complementary approach is to project out the configurations with multiply occupied sites from the free fermionic Fermi-sea wave function. This, so-called Gutzwiller projection method proved to be efficient in SU(2) systems [83–85]. In this method the self-consistency is not required, a suitably chosen hopping configuration can give an accurate description of the correlations. As an example, for one-dimensional SU(4) chains the exponents of the correlation function [86] can be reproduced with high accuracy in this approach (see section 5.8).

In the mean field approach, the self-consistent solution often results in a $\chi_{i,j}$ configuration, where the flux i.e. the phase of $\prod \chi_{i,j}$ around the elementary plaquettes is non-zero. For the SU(N) square lattice when on each site the spin can be represented by a Young tableau of 1 column and $N/2$ rows (so that two sites can form an SU(N) singlet), the energetically favored mean-field solution has a π-flux for each plaquette [74]. For the fundamental SU(6) honeycomb lattice, the energetically most favorable configuration was the one with $2\pi/3$ flux for each hexagon plaquette [82].

Similarly, the Gutzwiller projection often gives better energies with a non-trivial flux configuration [87, 88]. For the SU(4) square lattice a Gutzwiller projected variational wave function based on

a Majorana-fermion approach predicted spin-orbital liquid behavior [89], opposed to the plaquette order suggested by the linear flavor wave theory. (As it turns out, unbiased numerical calculations using tensor network algorithms showed that probably a third scenario, a dimerized state is realized [79].)

The topologically different hopping-configurations can be classified using Projective Symmetry Group analysis [90]. This method is effective in describing algebraic spin-liquids in SU(2) systems, where full PSG classifications are available for several cases [91]. For the SU(N) case this method is not so well established yet, but a properly chosen ansatz on the free fermionic hopping configuration can still provide valuable insight on the ground state structure. We will use the Gutzwiller-projection approach on the honeycomb lattice to calculate bond energies and correlation functions of the SU(3) and SU(4) Heisenberg-model. In Chapter 5 we will give a description how these quantities can be calculated for finite systems using Monte Carlo algorithm.

4.3.3 Tensor network algorithms, iPEPS

The tensor network representation used in higher dimensional systems can be understood as a generalization of the matrix product state (MPS) representation of one dimensional spin states. In one dimension a general matrix product state can be written as

$$\Psi = \sum_{j_1, j_2, j_L} \mathrm{Tr}\left(A^{[1]j_1} A^{[2]j_2} \dots A^{[L]j_L}\right) |j_1, j_2, \dots, j_L\rangle \tag{4.17}$$

where $|j_n\rangle$ is a basis for local states at site n, and $A^{[n]j_n}$ is a $d_{n-1} \times d_n$ matrix [92]. In general the sets of matrices for each site can be different. The coefficient of a $|j_1, j_2, \dots, j_L\rangle$ configuration is

$$\sum_{m_1=1}^{d_1} \sum_{m_2=1}^{d_2} \cdots \sum_{m_L=L}^{d_L} A^{[1]j_1}_{m_L, m_1} A^{[2]j_2}_{m_1, m_2} \dots A^{[L]j_L}_{m_{L-1}, m_L} \tag{4.18}$$

One can make calculations on systems with open boundary conditions by setting d_L to 1. The special case of $d_n \equiv 1$ is the site factorized approach, and by increasing the dimension of the matrices more and more entanglement is allowed in $|\Psi\rangle$. MPS can be used to efficiently describe one-dimensional gapped systems, as the ground state of such systems can be approximated to arbitrary precision by finite ds. The MPS variational approach provides a framework for DMRG calculations in one dimensional systems.

A generalized version can be used in higher dimensional systems as well, where tensors are considered instead of matrices. The rank of the tensor on each site corresponds to the number of neighbors, for example on the square lattice one should take rank-4 tensors for each site. The dimension of the tensors corresponds to the precision of the approach. This variational state

is called projected entangled-pair state (PEPS)[27], but also often referred to as tensor product state.

In an infinite PEPS or iPEPS, we consider periodic boundary conditions around the unit cell to represent a wave function in the thermodynamical limit. Apart from the selection of unit cell this approach is unbiased, i.e. doesn't require any initial assumption on the ground state structure, so it is an excellent starting point, which can provide the basis for further investigations by other methods.

Chapter 5

Introduction to variational Monte Carlo calculations

Monte Carlo method is a collective name for a wide number of computational algorithms, which can be applied in different fields to calculate quantities or properties of systems with a very large number of particles or degrees of freedom. The common feature of these methods is that instead of considering every possible term or contribution in calculating a given quantity, Monte Carlo methods use random sampling to select a representative portion of these terms. The power of Monte Carlo methods is that they require much less computer resources than other, explicit methods, and still can provide accurate and controlled results. The book of Mark Newman and Gerard Barkema [93] offers a great introduction to the basics of Monte Carlo calculations.

The first instances of these methods were used to estimate difficult integrals numerically. The concept was based on the picture that $\int_0^x f(x')dx'$ gives the size of the area under the curve of $f(x')$ on the $[0, x]$ interval. For the sake of simplicity we assume that $f(x') > 0$ on that interval. To give an estimate of the integral one can repeatedly take random numbers x_i in $[0, x]$ and y_i in $[0, y_{\max}]$, where $y_{\max} > \sup\{f(x'), x' \in [0, x]\}$. If x_i and y_i are chosen uniformly in the corresponding interval, the probability that the (x_i, y_i) point is under the curve of $f(x)$ is equal to $\int_0^x f(x')dx'/(x \cdot y_{\max})$. If a large number of points are randomized the estimate of the integral is

$$\int_0^x f(x')dx' \approx \frac{M}{N} x \cdot y_{\max}, \tag{5.1}$$

where N is the total number of (x_i, y_i) points, and M is the number of points for which $f(x_i) < y_i$. The more points are taken the more precise the approximation becomes. This method provides a simple way to numerically estimate difficult integrals and in principle it can be carried out even manually. Of course, computers can considerably speed up the process.

Another famous example for the use of such techniques is Buffon's needle experiment, which can be used to estimate the value of π. The idea is to throw a needle of length l at random on a sheet of paper on which parallel lines are drawn with a distance d. If $d \geq l$, the probability that the needle will intersect a line is $2l/d\pi$. So, if one counts the M number of drops where the needle intersects a line the estimate for π can be given as

$$\pi \approx \frac{2Nl}{Md} \tag{5.2}$$

where N is the total number of needle drops. Again, the more drops we make the more accurate the estimate becomes.

Monte Carlo techniques got a big boost and attention at the time of the Second World War, when they were used for neutron diffusion calculations in the construction of the atomic bomb. Later the techniques were used in the development of the hydrogen bomb as well. The name Monte Carlo was conceived in 1949, when it was used by Nicholas Metropolis and Stanislaw Ulam. The Hungarian mathematician John von Neumann (Neumann János) also played an important role in the improvement of the method and implementing it to the time's "super-computer" (ENIAC). Among others he created a pseudo-random number generating method (the middle square method). Since Monte Carlo algorithms use random sampling, a good pseudo-random generator is a crucial part of the simulations.

Since then, the growth in computer power and the improvement of techniques allowed the method to provide more and more accurate predictions in the field of physics. Apart from more or less obvious approaches in statistical physics, it is ingeniously used to address difficult quantum mechanical problems both at zero and finite temperature.

In the following sections we will explain how to use a Monte Carlo algorithm to calculate different quantities for Gutzwiller projected variational wave functions. First, we present the basic idea, and will include improvements to the algorithm step by step, in the hope that through this specific problem the reader can get an insight into the concept of Monte Carlo methods.

5.1 Spin-spin correlation function in the Gutzwiller projected ground state

We can use a Monte Carlo algorithm to calculate color-color $\langle n_i^\beta n_j^\beta \rangle$ correlation functions in Gutzwiller-projected variational wave functions, where n_i^β is the onsite color density for color β. One can also calculate Heisenberg-bond energies and bond-bond correlations for these wave

functions, which we will discuss later. The variatonal wave function is derived from the Fermi-sea ground state of a free fermionic Hamiltonian,

$$H = -\sum_{\alpha}\sum_{\langle i,j\rangle}\left(t_{i,j}f^{\dagger}_{j,\alpha}f_{i,\alpha} + h.c.\right). \tag{5.3}$$

The energy levels are filled to $1/N$ for each color, so that the number of fermions in the system is equal to the number of sites. From now on, we will explicitly write the summation for colors, to avoid any misinterpretation. The Fermi-sea ground state wave function for a system with N_s sites has the form

$$|\Psi\rangle = \sum_{\{j\}}\prod_{\alpha=1}^{N} w_{\{j^\alpha\}}|j^\alpha_1 j^\alpha_2 \dots j^\alpha_{\mathsf{N}_s/N}\rangle \tag{5.4}$$

where j^α_l denotes the position of the l-th fermion with color α, and $w_{\{j^\alpha\}}$ is a Slater-determinant for color α,

$$w_{\{j^\alpha\}} = \begin{vmatrix} \xi_1(j^\alpha_1) & \xi_1(j^\alpha_2) & \dots & \xi_1(j^\alpha_{\mathsf{N}_s/N}) \\ \xi_2(j^\alpha_1) & \xi_2(j^\alpha_2) & \dots & \xi_2(j^\alpha_{\mathsf{N}_s/N}) \\ \vdots & \vdots & \ddots & \vdots \\ \xi_{\mathsf{N}_s/N}(j^\alpha_1) & \xi_{\mathsf{N}_s/N}(j^\alpha_2) & \dots & \xi_{\mathsf{N}_s/N}(j^\alpha_{\mathsf{N}_s/N}) \end{vmatrix}, \tag{5.5}$$

where $\xi_k(j)$ are the one fermion wave functions of the free fermionic Hamiltonian (5.3). The number of Slater-determinants corresponds to the number of colors (N). In the Fermi-sea ground states the $\{j^\alpha\}$ sets can overlap, i.e. it is possible that a site is occupied by more than one type of fermion, while other sites are empty. In the Gutzwiller projection we simply consider only those configurations where each site is strictly singly occupied (i.e. $\{j^\alpha\}\bigcap\{j^\beta\}$ is empty for $\alpha \neq \beta$). For a system with N_s sites, the number of such configurations is $\mathsf{N}_s!/((\mathsf{N}_s/N)!)^N$. As an illustration, for an SU(4) honeycomb lattice with $\mathsf{N}_s = 24$ sites, the number of one fermion per site configurations is 2 308 743 493 056.

The definition of the $|j^\alpha_1 j^\alpha_2 \dots j^\alpha_{\mathsf{N}_s/N}\rangle$ states are not unambiguous, one has to fix the order of fermion creation operators, since changing that order can introduce -1 factors which would cause trouble if not treated with care. We will order the creation operators according to colors, i.e. first we create all fermions with one kind of color, then all the fermions with the next color and so on. The order among the same kind of fermions is arbitrary, though the order of creation operators must be the same as of the one fermion wave functions in the corresponding Slater determinant.

$$\bigotimes_{\alpha=1}^{N}|j^\alpha_1 j^\alpha_2 \dots j^\alpha_{\mathsf{N}_s/N}\rangle = \prod_{\alpha=1}^{N}\left(f^{\dagger}_{j^\alpha_1,\alpha}f^{\dagger}_{j^\alpha_2,\alpha}\dots f^{\dagger}_{j^\alpha_{\mathsf{N}_s/N},\alpha}\right)|0\rangle\,, \tag{5.6}$$

where $|0\rangle$ is the vacuum state. In the following we will review the basics and tricks of Monte Carlo calculations through the example of calculating the $\langle n^\beta_i n^\beta_j\rangle$ correlation function for the Gutzwiller projected state. We will follow the narrative of [93].

5.2 Basic Concept of Monte Carlo calculation, importance sampling

The expression we want to calculate is the color-color correlation function,

$$\langle \sum_{\beta} n_i^{\beta} n_j^{\beta} \rangle = \frac{\langle \Psi_{GW} | \sum_{\beta} n_i^{\beta} n_j^{\beta} | \Psi_{GW} \rangle}{\langle \Psi_{GW} | \Psi_{GW} \rangle}. \tag{5.7}$$

In case of color independent hopping amplitudes in the free fermionic Hamiltonian (5.3), $\langle n_i^{\beta} n_j^{\beta} \rangle$ has the same value for all colors. $n_i^{\beta} n_j^{\beta}$ is a diagonal operator, i.e. in the expansion only diagonal matrix elements of configurations are present. Expanding the Gutzwiller-projected wave function we get

$$\langle n_i^{\beta} n_j^{\beta} \rangle = \frac{1}{\sum_{\{j\}} \left| w_{\{j\}} \right|^2} \sum_{\{j\}} \left| w_{\{j\}} \right|^2 \langle \{j\} | n_i^{\beta} n_j^{\beta} | \{j\} \rangle, \tag{5.8}$$

where $\left| w_{\{j\}} \right|^2 = \prod_{\alpha=1}^{N} \left| w_{\{j^{\alpha}\}} \right|^2$ and $|\{j\}\rangle = \otimes_{\alpha} | j_1^{\alpha} j_2^{\alpha} \dots j_{\mathrm{N}_s/N}^{\alpha} \rangle$ is a fermion configuration. The sum runs through all nonequivalent configurations with strictly one fermion per site. The expectation $\langle \{j\} | n_i^{\beta} n_j^{\beta} | \{j\} \rangle$ is 1 if sites i and j are both occupied by a fermion with color β, and 0 in any other case.

To exactly calculate $\langle n_i^{\beta} n_j^{\beta} \rangle$ a vast number of states should be considered. The basic concept of Monte Carlo calculations is to randomly choose several representative configurations and give an estimate on $\langle n_i^{\beta} n_j^{\beta} \rangle$ based on these configurations.

The simplest way to choose configurations is to distribute the fermions randomly, i.e. all configurations have the same probability to be chosen. In this case the estimator is

$$\langle n_i^{\beta} n_j^{\beta} \rangle_{\mathrm{MC}_1} = \frac{1}{\sum_{\mu=1}^{M} \left| w_{\{j\}_{\mu}} \right|^2} \sum_{\mu=1}^{M} \left| w_{\{j\}_{\mu}} \right|^2 \langle \{j\}_{\mu} | n_i^{\beta} n_j^{\beta} | \{j\}_{\mu} \rangle \tag{5.9}$$

where μ indexes the chosen $\{j\}_{\mu}$ configurations. The stochastic expectation of $\langle n_i^{\beta} n_j^{\beta} \rangle_{\mathrm{MC}_1}$ is $\langle n_i^{\beta} n_j^{\beta} \rangle$, so by increasing the number of sampled states (M), we get a more and more accurate estimator.

However, as it is often the case, a minority part of the configurations provides the main contribution to the sum in $\langle n_i^{\beta} n_j^{\beta} \rangle$, and there can be a difference of several magnitudes between the weight of different configurations, so the convergence of the estimator (5.9) is really poor, because most of the time we pick states which has really low contribution to the quantum mechanical expectation value. If we pick a configuration with higher weight after sampling a lot of low-weight states, that one higher-weight configuration state will dominate the value of the estimator, so the majority of the samplings will be in vain.

Fig. 5.1 shows the logarithmic distribution of the weights $\left|w_{\{j\}_\mu}\right|^2$ of 800 000 fermion configuration chosen with uniform probability for the SU(4) honeycomb lattice system with $N_s = 216$ sites and uniform π-flux hopping configuration (see Chapter 6 for detailed explanation). As it can be seen, the selected configurations has weights ~100 magnitudes smaller, than the highest possible weight of the four sublattice ordered configuration predicted by linear-flavor wave theory (shown in Fig. 4.2b).

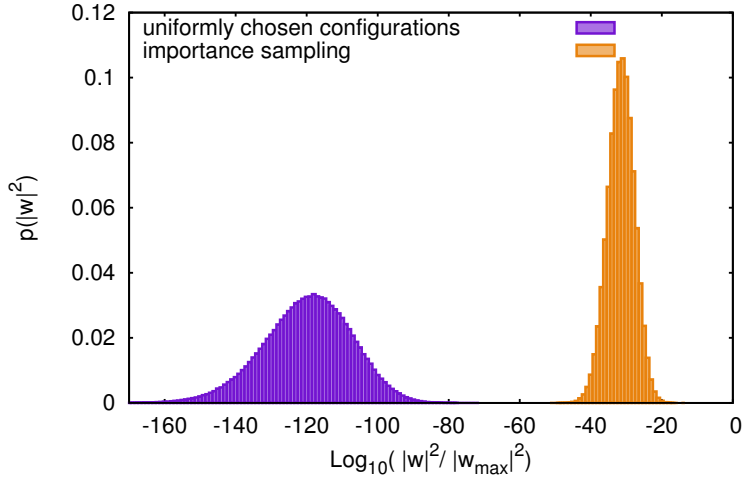

FIGURE 5.1: Distribution of the $\left|w_{\{j\}_\mu}\right|^2$ weight of 800 000 configurations chosen with uniform probability, compared to a distribution of a set chosen by importance sampling for a $N_s = 216$ cluster. The highest weight $|w_{\max}|$ is achieved for the four-sublattice ordered configuration predicted by LFWT.

To speed up the convergence one can pick the configurations with the probability proportional to their weight $\left|w_{\{j\}}\right|^2$. If a $\{j\}_\mu$ configuration is chosen with a probability

$$p^{\mathrm{IS}}(\{j\}_\mu) = \frac{\left|w_{\{j\}_\mu}\right|^2}{\sum\limits_{\{j\}} \left|w_{\{j\}}\right|^2} \tag{5.10}$$

then the estimator on the color-color correlation function after M sampled configuration is

$$\langle n_i^\beta n_j^\beta \rangle_{\mathrm{MC}_2} = \frac{1}{M} \sum_{\mu=1}^{M} \langle \{j\}_\mu | n_i^\beta n_j^\beta | \{j\}_\mu \rangle. \tag{5.11}$$

The weights are not included in the estimator, since the sampling process already takes them into account. The stochastic expectation of this estimator is also $\langle n_i^\beta n_j^\beta \rangle$, although it provides much more accurate estimation with the same number of samples. In this case all sampled configurations contribute to the estimator equally, so the convergence will be much faster.

This selection is called importance sampling. Comparing to uniform sampling in Fig. 5.1, it can be seen that with importance sampling the weight of the picked configurations is much higher

and closer to the maximum weight.

The question arises how to pick configurations randomly with the probability $p^{\mathrm{IS}}(\{j\})$. As we will see this can be done without the need to calculate the actual weights of all the states. The analogy to the classical statistical physics might give a valuable perspective.

In statistical physics the calculation of some macroscopic quantity of a system (like the magnetization of some spin models, or the energy of a container of gas) is thought as an average over an ensemble, i.e. we imagine a large number of duplicates of the system, each exhibiting a different microscopic configuration, we measure the quantity in question in all these duplicates and we take the average of these measurements. In real life however we only have one instance of the system, so instead we make measurements in time, letting the system to evolve between measurements, so at each sampling it exhibits a different, hopefully independent microscopic configuration. In statistical physics, the probability that the system will be in a certain microscopic configurations is proportional to the Boltzmann weight $e^{-\beta E}$, where E is the energy of the system, and β is the inverse temperature. In our case the probability distribution for configurations is given by $p^{\mathrm{IS}}(\{j\})$ defined in (5.10). To implement a similar "measurement in time" approach we need to create some dynamics or time evolution in the phase space of the 1 fermion/site configurations.

5.3 Markov processes, acceptance ratios

The concept of sampling configurations with a certain probability distribution is to create a dynamics for the fermion configurations, and at certain times make measurement at that certain configuration. The key is the so called discrete time Markov process, which is determined by the transition matrix $\mathbf{W}$. $W(\{j\} \to \{j'\})$ is the probability that from a given $\{j\}$ configuration the system changes into $\{j\}'$ in a time step. The transition matrix allows us to tell how a given probability distribution will change after a step.

$$\frac{\partial p(\{j\},t)}{\partial t} = \sum_{\{j'\}} \left[W(\{j'\} \to \{j\})p(\{j'\},t) - W(\{j\} \to \{j'\})p(\{j\},t)\right] \tag{5.12}$$

where $p(\{j\},t)$ is the probability, that at time t the system is in configuration $\{j\}$. This is the so called master equation. This set of equations describes, that the probability of the system being in a given $\{j\}$ configuration is increased by the probability that after a time step the system evolves into that configuration, and decreased by the probability that the system was in $\{j\}$, but evolved into an other configuration.

If the transition matrix is time-independent, the system has a stationary or equilibrium distribution for which $\partial p(\{j\},t)/\partial t = 0$. For physical systems in equilibrium, a stronger condition can

be assumed, where each part of the sum in the right hand side of the master equation is 0:

$$W(\{j'\} \to \{j\})p(\{j'\}, t) - W(\{j\} \to \{j'\})p(\{j\}, t) = 0 \tag{5.13}$$

for all $\{j\}, \{j'\}$. This is the so called detailed balance condition, which states that the equilibrium stands not just for the probablity distribution, but for all paths, i.e. there is no current between any two configurations in the phase space. In statistical mechanics this assumption is usually validated by the reversibility of the physical processes.

It can be proven, that if a system has an equilibrium distribution which satisfies the detailed balance, then the probability distribution will indeed converge to this equilibrium. This corresponds to the second law of thermodynamics i.e. that the (information) entropy always increases.

In our case we want to define a transition matrix on the phase space of 1 fermion/site configurations that satisfies the detailed balance with the probabilities $p^{\mathrm{IS}}(\{j\})$ defined in (5.10). Once we defined a suitable dynamics we have to select an initial configuration, it doesn't matter how, since the dynamics ensures, that the system will reach the equilibrium distribution. The easiest is to choose a starting configuration with uniform probability. At this point, we have to let the system evolve in time until it reaches equilibrium, then, if we make a measurement, the probability that the system will be in a given $\{j\}$ configuration will be indeed $p^{\mathrm{IS}}(\{j\})$.

Assuming we found the dynamics for our system, we still face some computational issues. A naive implementation of an elementary time step would require to collect all possible target states and the transition probabilities to those states, and make a choice according to these probabilities. Since the storage of all $W(\{j\} \to \{j'\})$ is impossible, we would need to generate the required probabilities at each step, which is really inefficient and time consuming.

Fortunately, we can save ourselves from this by introducing so called acceptance ratios. We can split the transition probability into two parts:

$$W(\{j\} \to \{j'\}) = g(\{j\} \to \{j'\})A(\{j\} \to \{j'\}) \tag{5.14}$$

where $g(\{j\} \to \{j'\})$ is the so called selection probability and $A(\{j\} \to \{j'\})$ is the acceptance ratio. The selection process always selects a new configuration ($\sum_{\{j'\}:\{j'\}\neq\{j\}} g(\{j\} \to \{j'\}) = 1$), but after selecting the target, the step is only made with a probability given by $A(\{j\} \to \{j'\})$.

The detailed balance now has the form

$$\frac{p^{\mathrm{IS}}(\{j\})}{p^{\mathrm{IS}}(\{j'\})} = \frac{g(\{j'\} \to \{j\})A(\{j'\} \to \{j\})}{g(\{j\} \to \{j'\})A(\{j\} \to \{j'\})}. \tag{5.15}$$

If we choose a selection process in such a way, that all configurations have the same number of reachable neighbors, and the selection probability is uniform for all targets, then the detailed

balance can be satisfied with the proper choice of acceptance ratios. The main advantage of this method is that we can select a target configuration without generating the full $W(\{j\} \to \{j'\})$ transition probabilities, and we only need to calculate the acceptance ratio to the selected target.

In our calculations we considered the selection process to connect configurations, which can be reached by exchanging two (not necessarily neighboring) fermions with different colors. In this case, for each configuration there are $\binom{N}{2}\left(\frac{N_s}{N}\right)^2$ target configurations, and we choose one from them with uniform probability.

As for the acceptance ratio, we used the most common realization for an importance sampling method, the so-called Metropolis algorithm [94], where the acceptance ratios are set as

$$A(\{j\} \to \{j'\}) = \begin{cases} 1, & \text{if } p^{\mathrm{IS}}(\{j'\}) > p^{\mathrm{IS}}(\{j\}), \\ \frac{p^{\mathrm{IS}}(\{j'\})}{p^{\mathrm{IS}}(\{j\})}, & \text{if } p^{\mathrm{IS}}(\{j'\}) \leq p^{\mathrm{IS}}(\{j\}). \end{cases} \tag{5.16}$$

In our case the ratio of the probabilities is

$$\frac{p^{\mathrm{IS}}(\{j'\})}{p^{\mathrm{IS}}(\{j\})} = \prod_{\alpha=1}^{N} \frac{\left|w_{\{j'^{\alpha}\}}\right|^2}{\left|w_{\{j^{\alpha}\}}\right|^2}, \tag{5.17}$$

which is the square of the ratio of two products of Slater-determinants. In general the computation of the determinant of an $n \times n$ matrix would require $O(n^3)$ elementary operations, however in our case we just slightly modify the Slater-matrices. In the selection process two fermions with different colors are chosen, and their positions are exchanged. Since two fermions are moved, only the two Slater determinants of the corresponding colors will be modified. In each of the two determinants, only one column will be changed, corresponding to the position of the exchanged fermions. If we choose a fermion with color α on site j_l^{α} and a fermion with color β on site j_m^{β}, then the values of the the l^{th} column in the Slater-determinant for color α, and the values of the m^{th} column in the Slater-determinant for color β will be exchanged.

So we need to calculate ratios of determinants where only a single column is modified. The properties of determinants allow an effective update in this case.

5.4 Efficient determinant update

5.4.1 Determinants, inverse matrices, a really brief mathematical reminder

The determinant of an $n \times n$ square matrix $\mathbf{A}$ is defined as

$$\det(\mathbf{A}) = \sum_{\pi} (-1)^{I(\pi)} a_{1\pi(1)} a_{2\pi(2)} \dots a_{n\pi(n)}, \tag{5.18}$$

where a_{ij} is the matrix element in the i^{th} row and j^{th} column of $\mathbf{A}$, the sum goes over all n-dimensional permutation π, and $I(\pi)$ is the number of inversions in π. The determinant can be also calculated recursively,

$$\det(\mathbf{A}) = \sum_j (-1)^{i+j} \cdot a_{ij} \cdot \det(\mathbf{A}_{ij}), \tag{5.19}$$

where $\mathbf{A}_{ij}$ is an $(n-1)\times(n-1)$ so-called minor matrix which we get by omitting the i^{th} row and j^{th} column of $\mathbf{A}$. This latter formula is known as the Laplace -formula.

The inverse of an $n \times n$ square matrix $\mathbf{A}$ is also an $n \times n$ matrix denoted by $\mathbf{A}^{-1}$ for which

$$\mathbf{A} \cdot \mathbf{A}^{-1} = \mathbf{A}^{-1} \cdot \mathbf{A} = \mathbf{I}, \tag{5.20}$$

where $\mathbf{I}$ is the $n \times n$ identity matrix. This definition can be written as

$$\sum_{j=1}^{n} a_{ij}\, a_{jk}^{-1} = \delta_{ik}, \tag{5.21}$$

where a_{ij}^{-1} is the element in the i^{th} row and j^{th} column of $\mathbf{A}^{-1}$, and δ_{ik} is the Kronecker-delta symbol, which gives 1 if $i = k$, and 0 otherwise. The elements of the inverse matrix can be calculated as

$$a_{jk}^{-1} = \frac{1}{\det(\mathbf{A})}(-1)^{(j+k)}\det(\mathbf{A}_{kj}). \tag{5.22}$$

As we can see, in the inverse matrix we can also find the determinants of the minor matrices of $\mathbf{A}$. This is the key for a time efficient determinant update, when only a column is changed in the matrix. We will need to keep track of the inverse matrix as well, but as we will see, it can be updated efficiently as well.

5.4.2 Determinant update if only one column is changed

If we change the k^{th} column of the matrix $\mathbf{A}$, based on equations (5.19) and (5.22) the determinant of the updated matrix will be

$$\det(\tilde{\mathbf{A}}) = \sum_{j=1}^{n}(-1)^{j+k}\tilde{a}_{jk}\det(\tilde{\mathbf{A}}_{jk}) = \sum_{j=1}^{n}(-1)^{j+k}\tilde{a}_{jk}\det(\mathbf{A}_{jk}) = \det(\mathbf{A})\sum_{j=1}^{n}\tilde{a}_{jk}a_{kj}^{-1}, \tag{5.23}$$

where $\tilde{a}_{jk}$ are the updated values in column k. The $\mathbf{A}_{jk}$ minor matrices are left unchanged, since we only change elements in the k^{th} column. So, if the elements of the inverse matrix are stored as well, the ratio of the new and old determinant is really easy to calculate:

$$q := \frac{\det(\tilde{\mathbf{A}})}{\det(\mathbf{A})} = \sum_{j=1}^{n}\tilde{a}_{jk}a_{kj}^{-1}. \tag{5.24}$$

In every Monte Carlo step two Slater determinants are modified, so we need to calculate the ratios for two pairs of determinants using Eq. 5.24. At this point, $q_1^2 \cdot q_2^2$ will be the ratio of the probabilities of the new and the old configurations, which can be used to decide whether we accept the step or not. If $q_1^2 \cdot q_2^2 \geq 1$ we always accept the new configuration, if $q_1^2 \cdot q_2^2 \leq 1$ we only accept the new configuration with a probability of $q_1^2 \cdot q_2^2$. If we do not accept the step, then we keep the original configuration and continue the algorithm by selecting a new target. However, if we accept the step, we have to update the Slater matrices and the inverse matrices as well to be able to continue the simulation.

For the elements in the k^{th} row of the inverse matrix $\mathbf{A}^{-1}$ the update is

$$\tilde{a}_{kj}^{-1} = \frac{1}{\det(\tilde{\mathbf{A}})}(-1)^{(k+j)}\tilde{\mathbf{A}}_{jk} = \frac{1}{\det(\tilde{\mathbf{A}})}(-1)^{(k+j)}\mathbf{A}_{jk} = \frac{1}{q}a_{kj}^{-1}, \tag{5.25}$$

since we only change elements of $\mathbf{A}$ in column k, the $\mathbf{A}_{jk}$ minor matrices are unchanged, we only need to compensate for the change in the total determinant. For any other element of the inverse matrix ($i \neq k$)

$$\tilde{a}_{ij}^{-1} = a_{ij}^{-1} - \frac{a_{kj}^{-1}}{q}\sum_{l=1}^{n} a_{il}^{-1}\tilde{a}_{lk} \ . \tag{5.26}$$

Note that the sum is the same for all elements in the i^{th} row, so a row of the inverse matrix can be updated in $O(n)$. (5.26) can be verified by simply using the definition in (5.21) to check if it indeed gives the elements of $\tilde{\mathbf{A}}^{-1}$.

$$\begin{aligned}
\sum_{j=1}^{n} \tilde{a}_{ij}^{-1}\tilde{a}_{jm} &= \sum_{j} a_{ij}^{-1}\tilde{a}_{jm} - \sum_{j=1}^{n}\frac{a_{kj}^{-1}}{q}\tilde{a}_{jm}\sum_{l=1}^{n} a_{il}^{-1}\tilde{a}_{lk} \\
&= \sum_{j=1}^{n} a_{ij}^{-1}\tilde{a}_{jm} - \delta_{km}\sum_{l=1}^{n} a_{il}^{-1}\tilde{a}_{lk} \\
&= \sum_{j=1}^{n} a_{ij}^{-1}a_{jm} + \sum_{j=1}^{n} a_{ij}^{-1}\left(\tilde{a}_{jm} - a_{jm}\right) - \delta_{km}\sum_{l=1}^{n} a_{il}^{-1}\tilde{a}_{lk} \\
&= \sum_{j=1}^{n} a_{ij}^{-1}a_{jm} + \delta_{km}\sum_{j=1}^{n} a_{ij}^{-1}\left(\tilde{a}_{jk} - a_{jk}\right) - \delta_{km}\sum_{l=1}^{n} a_{il}^{-1}\tilde{a}_{lk} \\
&= \delta_{im} - \delta_{mk}\delta_{ik} \\
&= \delta_{im}.
\end{aligned} \tag{5.27}$$

In the first step (from first to second line) we used $\frac{a_{kj}^{-1}}{q} = \tilde{a}_{kj}^{-1}$, which is the updated value for the k^{th} line of the inverse matrix. In the next step we decomposed the first sum. Next, we have to remember that in the second sum $\tilde{a}_{jm}$ and a_{jm} only differs if $m = k$, so we can introduce a δ_{km} factor. At this point (fourth line), by merging the second and third sum, we simply get the

matrix product of $\mathbf{A}$ and $\mathbf{A}^{-1}$. In the final step we must remember that this update was used for the $i \neq k$ lines, thus δ_{ik} is 0.

Using this method we can update the determinants and inverse matrices in $O(n^2)$ elementary operations, instead of an $O(n^3)$ determinant calculation. In our calculations the Slater-matrices can have several hundred rows and columns, and a pair of determinants are updated if the target configuration is accepted in the elementary step. When a typical run consists of $\sim 10^{10}$ steps, an efficient update is extremely important.

5.5 Making measurements

At this point we have a process which generates configurations with a given $p^{\mathrm{IS}}(\{j\})$ probability distribution in the equilibrium. The measurement for the $n_i^\beta n_j^\beta$ quantity is simple, we only have to check if the fermions of site i and j both have color β or not, and the value of $\langle\{j\}_\mu|n_i^\alpha n_j^\alpha|\{j\}_\mu\rangle$ is 1 or 0 accordingly. However there are some caveats that we must pay attention to.

We already mentioned the issue of relaxation time,. the time that is needed to reach equilibrium from a starting configuration. If we measure too early, i.e. when the probability distribution has not reached the equilibrium distribution, the estimate will be distorted. In equilibrium we pick configurations with higher weights (see Fig. 5.1), so if we check the weight of the configurations in the Monte Carlo process we must see some kind of convergence in time towards higher weights (See Fig. 5.2).

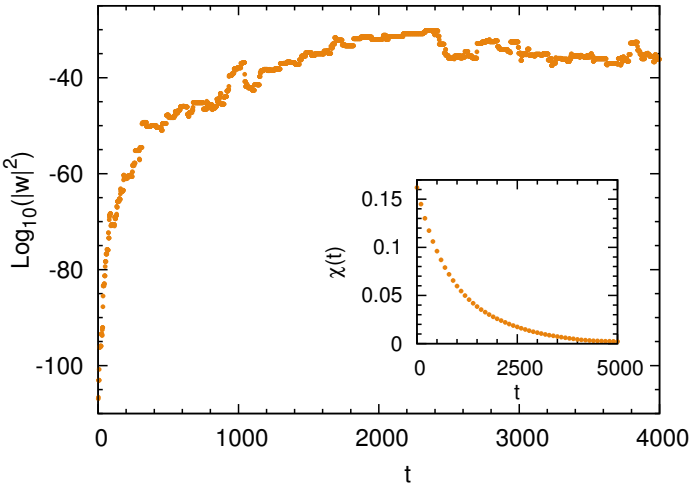

FIGURE 5.2: The $\left|w_{\{j\}}\right|^2$ weights of the configurations in the beginning of an importance sampling simulation, and in the inset the autocorrelation function for the $n_0^\beta n_\delta^\beta$ nearest neighbor color-color correlation, for $\mathsf{N}_s = 216$ honeycomb lattice with uniform π-flux configuration. Exponential fit gives an autocorrelation time around 1000 steps.

A similar problem is the sampling distance, the time we should wait between two measurements. The "measurement in time" is the real life alternative to the "measurement in ensemble" approach, and it is important to wait long enough, so that the measured configurations are stochastically independent. The correlation between measurements can be traced by the autocorrelation function

$$\chi_Q(t) = \int dt' \left(Q(t+t') - \langle Q \rangle\right)\left(Q(t) - \langle Q \rangle\right), \tag{5.28}$$

where $\langle Q \rangle = \int dt' Q(t')$ is the average of some measured quantity Q, in our case it is $n_i^\beta n_j^\beta$. The inset of Fig. 5.2 shows a typical autocorrelation function. A τ_Q correlation time can be defined by fitting an exponential decay on the autocorrelation function $\chi_Q(t)$. As a rule of thumb, one can say that if the sampling distance is larger than 2τ the measurements can be considered independent. A too small sampling distance won't ruin the whole estimation, since each measured configuration is still chosen with the equilibrium probability distribution, but the error could be underestimated if we don't realize that the measurements are correlated. There are several methods which can reveal these correlation and allow for realistic error estimates [95]. In our simulations we chose the sampling distance for every cluster to be around 5τ.

5.6 Off-diagonal quantities

So far we discussed how diagonal quantities can be calculated in the Gutzwiller projected variational state. With a little more effort, off-diagonal quantities, like the $\langle P_{kl} \rangle$ bond energies, can be estimated as well. Although in this case the sign changes caused by the exchange of fermionic operators should be followed carefully. The expectation of the P_{kl} exchange term can be written as

$$\langle P_{kl} \rangle = \frac{1}{\sum_{\{j\}} \left|w_{\{j\}}\right|^2} \sum_{\{j\},\{j'\}} \bar{w}_{\{j'\}} \cdot w_{\{j\}} \langle \{j'\} | P_{kl} | \{j\} \rangle, \tag{5.29}$$

where $\bar{w}_{\{j'\}}$ denotes the complex conjugate of $w_{\{j'\}}$. For each $\{j\}$ configuration $\langle \{j'\} | P_{kl} | \{j\} \rangle$ is non-zero for only one $\{j'\}$ configuration, where the colors of the fermions on sites k and l are interchanged, let us denote this configuration by $P_{kl}\{j\}$. For this configuration $\langle P_{kl}\{j\} | P_{kl} | \{j\} \rangle = -1$. The -1 factor is the result of the rearrangement of the fermion creation operators. Using the fermionic operators $P_{kl} = \sum_{\alpha,\beta} f^\dagger_{k,\alpha} f_{k,\beta} f^\dagger_{l,\beta} f_{l,\alpha}$ (for a clearer narrative, we write the summation over color indeces explicitly). If we apply P_{kl} on the $\{j\}$ configuration, it exchanges the color of fermions at sites k and l. But now on $P_{kl}\,|\{j\}\rangle$, the order of fermion creation operators are a little messed up. Let's say, that in $\{j\}$ the colors on sites k and l were green and red, respectively. After applying P_{kl}, we create a fermion with color red on site k and green one on site l. But, now there is a green fermion creation operator among the red ones and a red creation operator among the green ones. So we have to rearrange these two 'misplaced' operators, which will introduce a -1 factor. So that $|P_{kl}\{j\}\rangle = -P_{kl}\,|\{j\}\rangle$, where $|P_{kl}\{j\}\rangle$ follows the ordering we set up in Eq.

(5.6). To summarize, the $\langle P_{kl} \rangle$ quantity can be rewritten as

$$\langle P_{kl} \rangle = -\sum_{\{j\}} p^{\mathrm{IS}}(\{j\}) \cdot \frac{\bar{w}_{P_{kl}\{j\}}}{\bar{w}_{\{j\}}}, \tag{5.30}$$

where $p^{\mathrm{IS}}(\{j\})$ is the probability distribution defined in Eq. (5.10). In the Slater determinants of $|P_{kl}\{j\}\rangle$ one-one column of two determinants are exchanged, so $w_{P_{kl}\{j\}}/w_{\{j\}}$ can be calculated using Eq. (5.24).

$\langle P_{kl} \rangle$ can be estimated with measurements in the same Markov-process as used before, i.e. the acceptance ratios are set to satisfy the detailed balance for $p^{\mathrm{IS}}(\{j\})$. For each sampled $\{j\}_\mu$ configuration we have to calculate $\frac{\bar{w}_{P_{kl}\{j\}_\mu}}{\bar{w}_{\{j\}_\mu}}$, which is again the ratio of the Slater-determinants of the $P_{kl}\{j\}_\mu$ and $\{j\}_\mu$ configurations, and can be effectively calculated using Eq. (5.24), as we discussed in section 5.4.

Similarly, more complicated quantities can be estimated as well. For example, the bond-bond correlation functions $\langle P_{kl}P_{mn} \rangle$ can be given as

$$\langle P_{kl}P_{mn} \rangle = \sum_{\{j\}} p^{\mathrm{IS}}\{j\} \cdot \frac{\bar{w}_{P_{kl}P_{mn}\{j\}}}{\bar{w}_{\{j\}}}, \tag{5.31}$$

where $P_{kl}P_{mn}\{j\}$ is the configuration we get by first exchanging the fermions on site m and n, then on k and l in the configuration $\{j\}$. Calculating $\frac{\bar{w}_{P_{kl}P_{mn}\{j\}}}{\bar{w}_{\{j\}}}$ for the sampled configurations requires a complete matrix and inverse matrix update for the first exchange to be able to calculate the updated determinants after the second exchange.

5.7 Outline of the Monte Carlo algorithm

Summarizing the above considerations, the Monte Carlo algorithm has 3 main parts: (*i*) the initializing, (*ii*) the Monte Carlo time evolution of the system, and (*iii*) the measurement of the desired diagonal or off-diagonal quantities.

(*i*) In the initialization we solve the eigenvalue problem and determine the one-fermion wave functions of the free fermionic Hamiltonian (5.3), prepare an initial fermion configuration with one fermion per site, and calculate the Slater-matrices and the inverse matrices for this configuration.

(*ii*)The Monte Carlo time evolution consists of the following steps:

- Select two fermions with different colors in the current configuration, in the target configuration the position of these two fermions are exchanged.
- Calculate the ratio of the Slater-determinants of the target and the current configuration using Eq. (5.24).

- Decide if the configuration is accepted according to Eq. (5.16)
- If the target configuration is accepted, update the fermion configuration, the Slater matrices and the inverse of the Slater matrices using Eqs. (5.25) and (5.26). If the new configuration is not accepted, the current configuration is kept.

(*iii*) A measurement is made after M time steps ($M > 5\tau_{a.c.}$). For $n_i^\beta n_j^\beta$ the measurement is simple, we have to add 1 to the estimate if there is a fermion with color β on both i and j, and 0 in any other case. For the measurement of off-diagonal quantities see section 5.6. (Note that, at the end we have to divide the estimate with the number of measurements.) After a measurement, M elementary step should be made before the next measurement, and so on.

5.8 One dimensional Heisenberg-chain

As a demonstration of the Gutzwiller projection approach, we examined the SU(4) symmetric Heisenberg model on a chain, and compared our results, with the findings of continuous time quantum Monte Carlo (QMC) simulations [86], and Bethe ansatz calculations [96]. We consider the free fermionic Hamiltonian with equal hopping amplitudes,

$$H = -t \sum_{\beta} \sum_{i=1}^{L} \left(f_{i+1,\beta}^{\dagger} f_{i,\beta} + h.c. \right). \tag{5.32}$$

where periodic boundary conditions are assumed. The band structure is $\epsilon(k) = 2t\cos(k)$, which is quarter filled for each color for the SU(4) case (i.e. $k_F = \pi/4$). After the projection the energy per site of the Gutzwiller projected state is $-0.823(2)$ for $L = 300$, compared to the QMC energy $-0.8253(1)$ for $L = 100$, and the -0.8251 provided by the Bethe-ansatz solution for the infinite chain.

The $\langle \sum_\beta n_0^\beta n_r^\beta \rangle$ color-color correlation found by [86] using continuous time QMC method is very well reproduced by our variational Monte Carlo calculations (shown in Fig. 5.3). The Fourier transform shows a definite peak at $k = \pi/2$, so the decay of the color-color correlation in real space can be fitted by

$$\langle n_0^\alpha n_r^\alpha \rangle \approx b_{\pi/2} \left[r^{a_{\pi/2}} + (L-r)^{a_{\pi/2}} \right] \cos\left(\frac{\pi}{2} r\right) + b_0 \left[r^{a_0} + (L-r)^{a_0} \right]. \tag{5.33}$$

Based on the variational Monte Carlo calculation on the Gutzwiller projected wave function we got exponents $a_{\pi/2} = -1.51 \pm 0.006$ and $a_0 = -1.88 \pm 0.06$ for the L=300 chain. QMC results with the same fit gave exponents $a_{\pi/2} = -1.50 \pm 0.01$ and $a_0 = -1.86 \pm 0.16$ for L=100 chains. The $a_{\pi/2}$ exponents was estimated to be between -1.5 and -2 by DMRG calculations

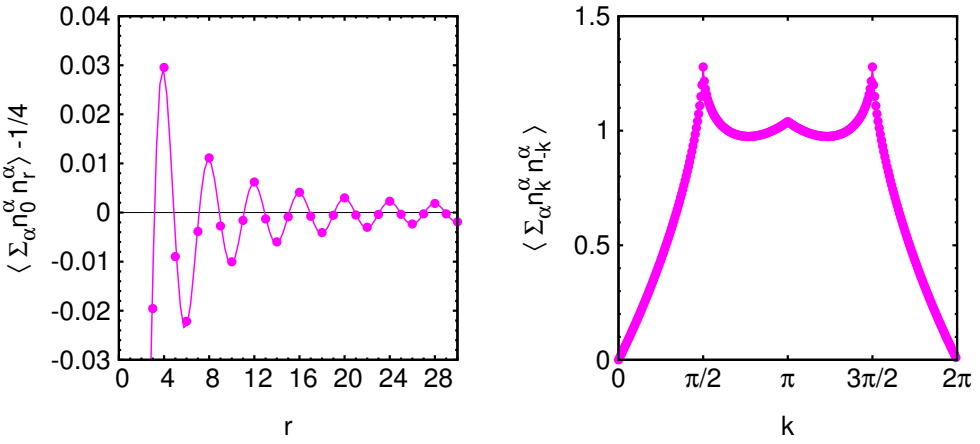

FIGURE 5.3: The color-color correlation for a chain of 300 sites, the line connecting the dots is a fit by Eq. (5.33). The Fourier transform, shows a sharp peak at $k = \pi/2$ and a smaller at $k = \pi$.

as well [1][97]. A prediction based on conformal field theory [98] gives exponents $a_{\pi/2} = -3/2$ and $a_0 = -2$. As we can see, the Gutzwiller projection approach reproduces the findings on the correlation functions of other methods very well.

We should note that the small peak in $\langle n_k^\alpha n_{-k}^\alpha \rangle$ at $k = \pi$ suggests that a $b_\pi \left[r^{a_\pi} + (L-r)^{a_\pi} \right] \cos(\pi r)$ term could be included in the fit as well. In this case the fitted exponents are $a_{\pi/2} = -1.50 \pm 0.0016$, $a_0 = -1.94 \pm 0.06$ and $a_\pi = -2.03 \pm 0.05$ for the L=300 system. The amplitude of the π component is of course smaller than the other two, and has a large error ($b_{\pi/2} = 0.286 \pm 0.002$, $b_0 = -0.129 \pm 0.008$ and $b_\pi = 0.07 \pm 0.01$).

[1]This huge uncertainty is caused by the boundary effect, since DMRG calculations were made with open boundary conditions.

Chapter 6

Algebraic spin-orbital liquid in the honeycomb lattice

The motivation to study the SU(4) Heisenberg-model on honeycomb lattice comes from the recent experimental report on the possible spin-orbital liquid behavior in $Ba_3CuSb_2O_9$ [29]. In this material Sb-Cu 'dumbbells' (see Fig. 6.1) form a triangular lattice. These dumbbells carry electric dipole moments, which show a three-sublattice ferrielectric ordering. As a result, the magnetic Cu^{++} atoms form a honeycomb lattice, with weak inter-layer coupling. In addition to spin-1/2 degrees of freedom , the orbitals of the Cu^{++} are also twofold degenerate. According to X-ray scattering studies, the orbitals fluctuate down to very low temperatures without any signature of a Jahn-Teller distortion, and the magnetic susceptibility also provides no evidence of magnetic long range ordering. Thus, it was concluded that a spin-orbital liquid with disordered spin and orbital structure is realized in Ba_3CuSb_2O.

A minimal model to describe the low energy properties of this material is a Kugel-Khomskii like spin-orbital Hamiltonian on the honeycomb lattice. As we already mentioned in Section 4.1, for special values of parameters the model becomes the highly symmetric SU(4) Heisenberg model,

$$\mathcal{H} = \sum_{\langle i,j \rangle} \left(2\mathbf{S}_i \mathbf{S}_j + \frac{1}{2} \right) \left(2\boldsymbol{\tau}_i \boldsymbol{\tau}_j + \frac{1}{2} \right) = \sum_{\langle i,j \rangle} P_{ij}^{(4)}. \tag{6.1}$$

From a theoretical aspect the SU(4) Heisenberg model is a promising candidate to accommodate a spin-orbital liquid ground state: (i) from linear flavor-wave theory we learned that the macroscopic degeneracy of the classical, site factorized ground state is only partially lifted by quantum fluctuations (Section 4.3.1 and Fig. 4.2); (ii) the honeycomb lattice has no four site plaquettes, so the formation of localized SU(4) singlets is not likely.

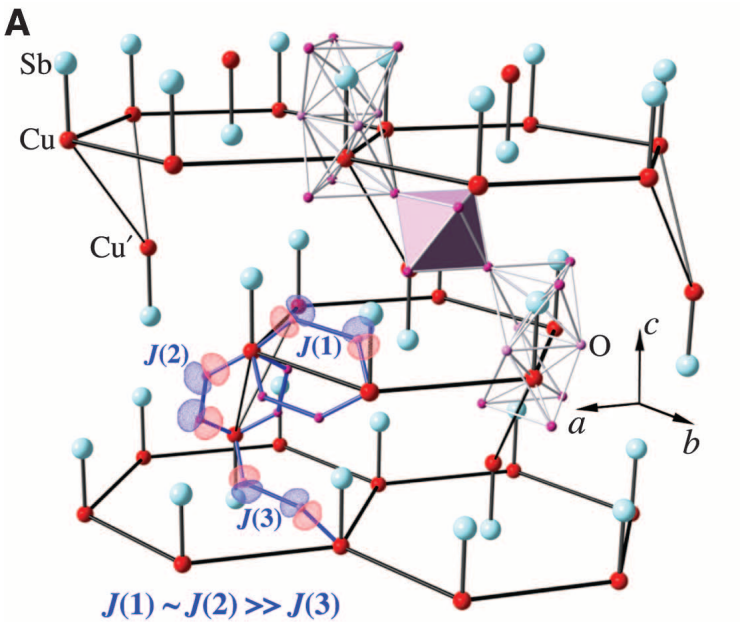

FIGURE 6.1: The crystal structure of $Ba_3CuSb_2O_9$. The centers of face sharing octahedra are occupied by Cu (smaller red spheres) and Sb (larger blue spheres) ions. These Cu-Sb dumbbells form a three sublattice ferrielectric order, resulting in a honeycomb structure for the Cu^{++} ions. Due to the threefold rotation axis of the $CuSbO_9$ units the d orbitals of the Cu^{++} are split resulting in a twofold orbital degeneracy for the hole in the e_g orbital. Figure taken from [29].

In this chapter we will discuss the findings of iPEPS and exact diagonalization calculations, and we will present our calculations on Gutzwiller projected wave functions using the variational Monte Carlo algorithm described in Chapter 5. All these calculations (IPEPS, ED, and VMC) were reported in a common publication [81], where we argued that an algebraic spin-orbital liquid is realized in this model.

6.1 Results of iPEPS calculations

In this introductory section we recollect the iPEPS results of Ref. [81]. iPEPS calculation with large tensor dimensions found no sign of lattice or SU(4) symmetry breaking. However, for smaller tensor dimensions (D=6) on a 4×4 unit cell, a color ordered state was found with a four sublattice order (Fig. 6.2a). With the same tensor dimension and a 2×2 unit cell a dimerized pattern was obtained where the dimerized bonds were the antisymmetric pair of 2 colors (Fig. 6.2b). In both cases as the tensor dimension is increased both the long-range order and the dimerization vanishes, verifying that there is no lattice or SU(4) symmetry breaking in the system (See Fig 6.3).

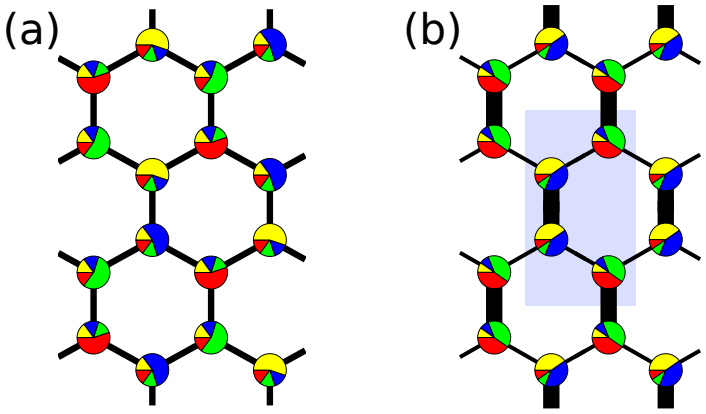

FIGURE 6.2: Ordered states found by iPEPS calculations at small tensor dimensions (calculations made by Philippe Corboz). The colored disks show the onsite density of the different color states, while the thickness of the bonds corresponds to the expectation value of the exchange interaction. (a) A color ordered state with SU(4) symmetry breaking found in a 4×4 unit cell (b) Dimerized SU(4) symmetry breaking order found in a 2×2 unit cell (marked with blue rectangle). In both cases the tensor dimensions were small (D=6), and upon increasing D, the orderings vanish.

The findings of iPEPS of no SU(4) or lattice symmetry breaking, complemented by the linear-flavor-wave results which also show no sign of lattice symmetry breaking, point towards a spin liquid ground state of the SU(4) Heisenberg model on the honeycomb lattice. In the following we will support this statement by calculating the color-color correlation function and structure factor of a Gutzwiller projected wave function of a uniform π-flux free fermion system. We will also check the stability towards the most plausible orderings suggested by iPEPS calculations or by findings in other lattices.

6.2 Free fermionic wave functions with different flux configurations

The free fermionic Hamiltonian we consider for the honeycomb lattice is

$$H = -\sum_{\alpha} \sum_{\langle i,j \rangle} \left(t_{i,j} f^{\dagger}_{j,\alpha} f_{i,\alpha} + h.c. \right) \tag{6.2}$$

where $f^{\dagger}_{i,\alpha}$($f_{i,\alpha}$) creates (annihilates) a fermion with flavor α at site i, and $\langle i, j \rangle$ runs over nearest neighbor bonds. In our calculations the $t_{i,j}$ hoppings are fixed, and we use this notation to emphasize that no self-consistency calculation is done, like for the $\chi_{i,j}$ in the mean-field approach.

The flux of a plaquette is the phase of the product $\prod t_{i,j}$ on the bonds around that plaquette. For example, if we take a hexagon plaquette with sites $1, 2, ..., 6$, the flux of that plaquette is the phase of $t_{1,2} \times t_{2,3} \times \cdots \times t_{5,6} \times t_{6,1}$. When we talk about a flux configuration on a lattice, we take the sites around each plaquette in the same direction (clockwise or counter-clockwise). Since other

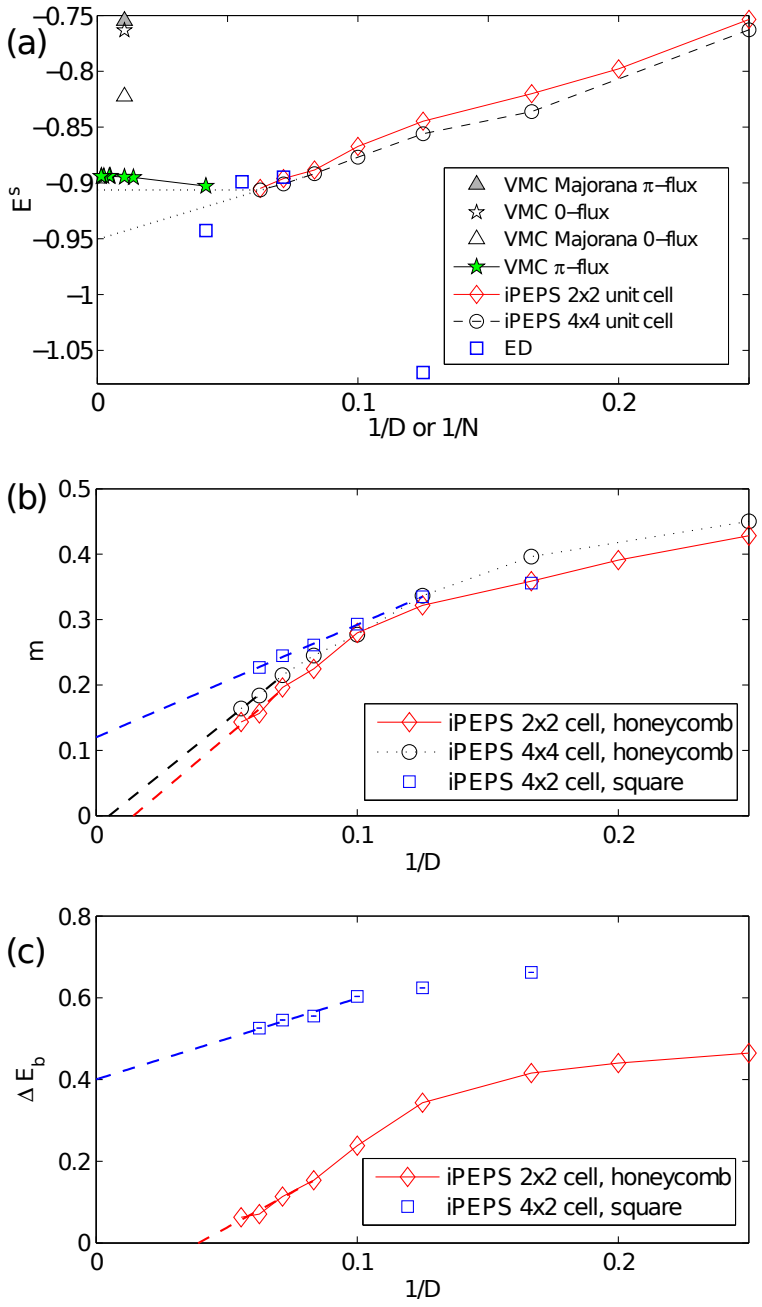

FIGURE 6.3: Results of iPEPS calculations (carried out by Philippe Corboz). (a) The energy per site as a function of the tensor dimension (D). The variational Monte Carlo (VMC) results are also included as a function of system size. (b) The local color order (m) of the system, as a function of tensor dimension. As it can be seen the SU(4) symmetry breaking vanishes as D is increased, the results for the square lattice are also shown, where a dimerized, color ordered pattern remains stable even for large D [79]. (c) The difference of bond energies in the system. For large D the dimerized pattern vanishes for the honeycomb lattice in contrast with the square lattice.

approaches (iPEPS, LFWT) showed no sign of translational invariance breaking for the SU(4) Heisenberg model on the honeycomb lattice, we will only consider uniform flux configurations as well. Based on the findings of [87, 88] for the square lattice, one can argue that for the SU(4) honeycomb lattice only the 0 and π flux configurations are relevant[1].

There are a lot of ways to create a hopping configuration with a given (0 or π) flux configuration, but these can often be connected by local gauge transformations. By introducing an arbitrary phase ϕ for the fermion creation/annihilation operator on a site, so that $f_{i,\alpha} \rightarrow \tilde{f}_{i,\alpha} = f_{i,\alpha}e^{i\phi}$, the phase of the hopping parameters on the bonds connected to that site are changed as $t_{i,i+\delta} \rightarrow \tilde{t}_{i,i+\delta} = t_{i,i+\delta}e^{-i\phi}$. A local gauge transformation at site i introduces a phase for the free fermionic wave functions at that site, which will appear in the calculation of the Slater determinants as a global phase factor, thus the projected wave function is left unchanged up to a phase. We note that, it is only true if the gauge transformation is color independent, in this case case the $S^{\alpha}_{\beta}(i) = f^{\dagger}_{i,\alpha}f_{i,\beta}$ spin operator are also left unchanged. If we only make the transformation for one color, for example for color red, the phase factor will only appear for those configurations were a red colored fermion is present at site i, thus the Gutzwiller projected state will be different.

If we consider real hopping parameters only, this means that the sign of the three hopping parameters connected to a site can be changed simultaneously and the physics of the system will remain the same. Furthermore, considering real hopping parameters ensures that the one-fermion wave functions are real, which allows the Monte Carlo calculation to run faster. To realize a π-flux configuration we used a configuration where the bonds with negative hoppings are aligned in chains, as shown in Fig. 6.5.

The honeycomb lattice with uniform hopping parameters (0-flux case), has a unit cell of two sites with a triangular Bravais-lattice. The smallest unit cell that can accommodate the π-flux hopping configuration and has the full symmetries of the honeycomb lattice has 8 sites (see Fig 6.4a). The Brillouin-zone is therefore reduced to the quarter of the original honeycomb Brillouin-zone and has 8 energy levels in 4 doubly degenerate bands. The band structure of the free fermion Hamiltonian of the 0- and π-flux case can be seen in Fig. 6.4c-d.

The energy levels are occupied till quarter filling, to set the number of fermions equal to the number of sites in the system. As it turns out a uniform π-flux configuration gives lower energies than a 0-flux configuration after the Gutzwiller projection: for the $\mathsf{N}_s = 96$ the energy per site is -0.89466 for the π-flux and -0.763304 for the 0-flux case, so we made detailed calculations in the π-flux case.

[1] private communication with Michael Hermele

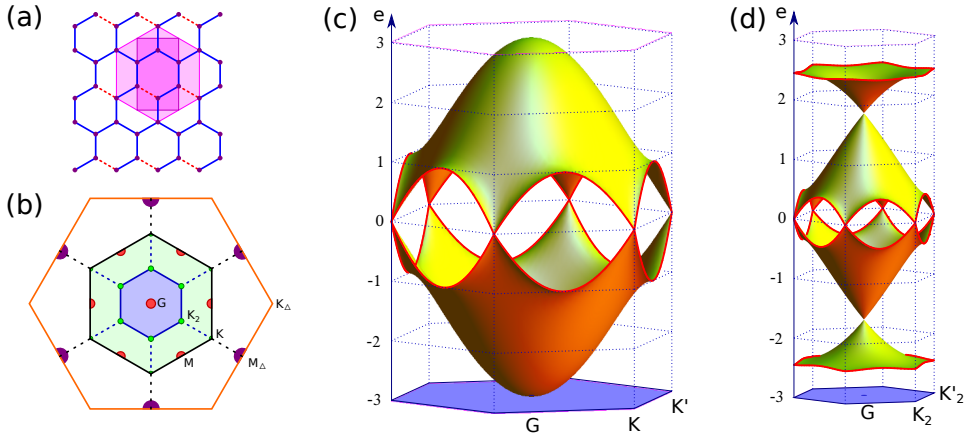

FIGURE 6.4: (a) The minimal 4-site, and 8-site hexagonal unit cell of the π-flux hopping configuration. (b) The Brillouin zone of the honeycomb lattice (black hexagon), and the reduced Brillouin-zone of the π-flux configuration (blue-hexagon).The outer (orange) hexagon shows the Brillouin zone of the triangular lattice, that we get by filling the centers of the honeycomb lattice. (c-d) the free fermion band structure in the 0-flux and π-flux case. In the π-flux case there is a Dirac-cone at quarter-filling, which is the Fermi-level in the SU(4) case.

6.3 Variational Monte Carlo calculations for finite clusters with uniform π-flux configuration

The nearest neighbor bond energies and color-color correlation functions can be calculated for the Gutzwiller projected wave function using the Monte Carlo algorithm we discussed in Chapter 5. If the free fermionic Hamiltonian is color independent, the quarter-filled Fermi sea ground state is a singlet (i.e. acting by the total spin operators gives 0). The Gutzwiller projection operator in the SU(4) can be written as

$$P_G = \prod_{i=1}^{N_s} \frac{1}{6} n_i(2-n_i)(3-n_i)(4-n_i) \tag{6.3}$$

where $n_i = \sum_{\alpha=1}^{4} n_i^\alpha$ is the total number of fermions at site i. Since the S_α^β spin operators do not change the number of fermions on the site, P_G commutes with the total spin operators, thus the projected variational state is also an SU(4) singlet.

Since the singlet state does not break the SU(4) symmetry (all the direction are equivalent), the $\langle P_{ij}\rangle$ can be expressed using only the diagonal operators as $\langle P_{ij}\rangle = 5\langle\sum_\alpha n_i^\alpha n_j^\alpha\rangle - 1$, for the general SU($N$) case

$$\langle P_{ij}\rangle = \left\langle f_{i,\alpha}^\dagger f_{i,\beta} f_{j,\beta}^\dagger f_{j,\alpha}\right\rangle = (N+1)\langle\sum_\alpha n_i^\alpha n_j^\alpha\rangle - 1. \tag{6.4}$$

This is similar to the SU(2) case, where $\langle \mathbf{S}_i \cdot \mathbf{S}_j\rangle = 3\langle S_i^z \cdot S_j^z\rangle = 3\langle(n_i^\uparrow - n_i^\downarrow)(n_j^\uparrow - n_j^\downarrow)\rangle/4$ if the SU(2) symmetry is not broken. Remembering that $(n_i^\uparrow + n_i^\downarrow)(n_j^\uparrow + n_j^\downarrow) = 1$ we get the SU(2)

version of Eq. (6.4)

The coefficients for the equation between $\langle P_{ij}\rangle$ and $\langle\sum_\alpha n_i^\alpha n_j^\alpha\rangle$ can be easily derived, for example, if we consider an SU(N) singlet covering state, which is clearly SU(N) symmetric, and compare the values of the two operators on different bonds. $\langle P_{ij}\rangle$ = -1 if i and j belong to the same singlet, and $1/N$ if they are parts of different singlets. Similarly, $\langle\sum_\alpha n_i^\alpha n_j^\alpha\rangle = 0$ in a singlet, and $1/N$ between singlets.

In this section we will discuss the results for the case where all the hopping parameters have the same magnitude in the free-fermionic Hamiltonian. Later we will argue, that this scenario is indeed energetically favorable towards the most likely instabilities.

We made calculations on two families of finite clusters all having the full symmetry of the honeycomb lattice. The first family consists of clusters with $\mathsf{N}_s = 2(2n)^2$ sites, and are defined by lattice vectors $\mathbf{g}_1 = 3(\sqrt{3}/2, 1/2)n$ and $\mathbf{g}_2 = (0, 3)n$, where n is an integer (the distance between nearest neighbor sites is chosen to be 1). From this family we considered clusters with N_s =24, 96, 216, 384, 600. The other family is defined by the lattice vectors $\mathbf{g}_1 = 3(\sqrt{3}, 0)n$ and $\mathbf{g}_2 = 3(\sqrt{3}/2, 3/2)n$ and contains $\mathsf{N}_s = 6(2n)^2$ sites. From this family we made calculations for N_s = 72, 200, 392, and 648. Fig. 6.5 shows these clusters in a π-flux hopping configuration on the honeycomb lattice as well as the lattice vectors of a selected representative for each case.

For all system sizes preliminary runs were made, the sampling distances were chosen to be around 5 times the correlation time (see Table 6.1 for details).

N	$\tau_{a.c.}$	Δn	ratio	number of measurements
24	22	1000	45.5	10^7
72	150	1000	6.7	10^7
96	260	2000	7.7	10^7
200	970	5000	5.1	$2\cdot10^6$
216	1080	5000	4.6	$2\cdot10^6$
384	2920	20000	6.8	$2\cdot10^6$
392	3340	20000	6.0	$2\cdot10^6$
600	7080	40000	5.6	10^6
648	8100	40000	4.9	10^6

TABLE 6.1: $\tau_{a.c.}$ autocorrelation times for the $\langle n_i^\alpha n_j^\alpha\rangle$ color-color correlation functions compared to the number of elementary steps between two measurements (Δn).

We note that the chains with negative hoppings can be aligned in twelve different ways. In most of the cases the different configurations can not be transformed into each other by local gauge transformations, and a spatial asymmetry is present in the color-color correlation functions. However, the different alignments can be connected by twisting the boundary conditions, i.e. by changing the sign of hoppings in one column. This change can not be described by local gauge transformations, but since it is a boundary-type change it suggests, that the asymmetry of the

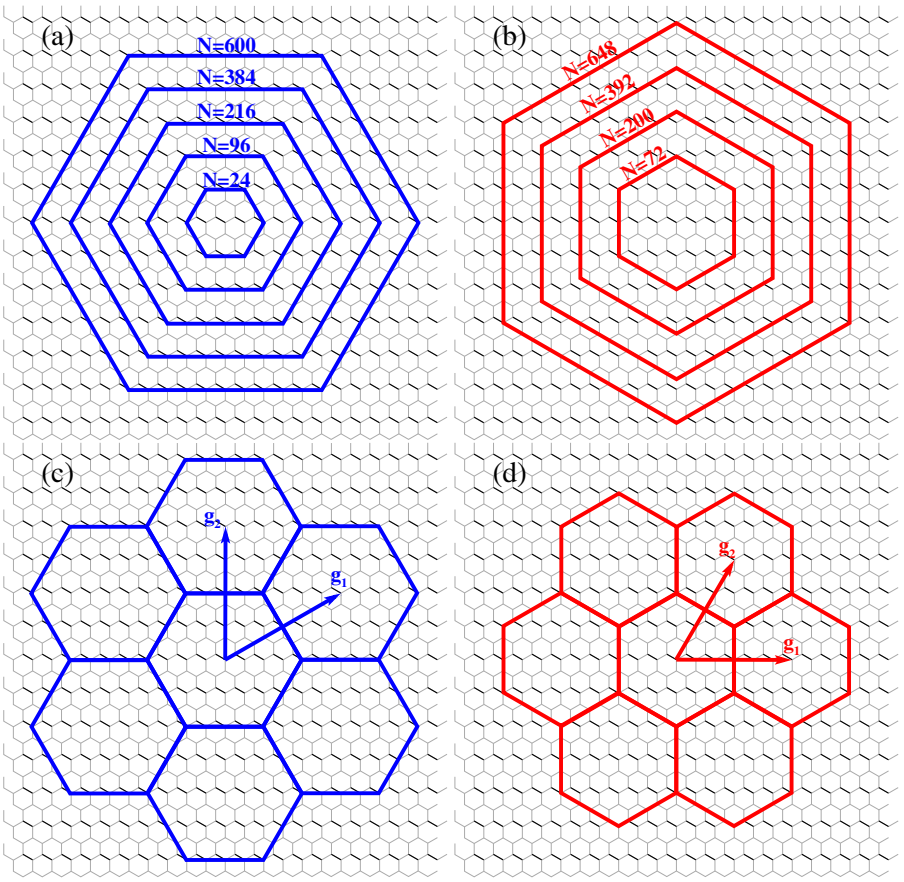

FIGURE 6.5: (a-b)Finite size clusters used for the Gutzwiller projected wave function calculations. The thick bonds denote a negative hopping amplitudes. (c-d) The $N_s = 96$ and $N_s = 72$ systems with the defining lattice vectors $\mathbf{g}_1$ and $\mathbf{g}_2$. The distance between nearest neighbor sites is chosen to be 1.

correlation function vanishes in the thermodynamic limit (see the inset of Fig. 6.8). In some cases ($N_s = 96$ and 384), all the twelve different configurations can be connected by local gauge transformations only. However, in these systems, the Fermi-sea ground state is degenerate, i.e. the Fermi-level is degenerate, and the choice of one-fermion wave functions in the Fermi-sea state is not unambiguous. To avoid this degeneracy, one can introduce antiperiodic boundary conditions, which again results in a vanishing asymmetry in the color-color correlation function.

6.3.1 Comparison with ED

The question arises, if this Gutzwiller projected approach gives a proper description of the ground state of the original SU(4) Heisenberg Hamiltonian. For the 1D Heisenberg chain we have shown that the Gutzwiller projected wave function reproduced the correlations quite accurately.

For the case of the honeycomb lattice we compare the VMC results with exact diagonaliztion findings for the $N_s = 24$ cluster. The exact diagonalization was made by Andreas Läuchli. As

we mentioned earlier the dimension of the Hilbert space of the $N_s = 24$ system is enormous (2 308 743 493 056), and even after considering the symmetries of the system this is one of the highest dimensional system where ED calculations were carried out so far.

Fig. 6.6 shows the color-color correlation $\langle \sum_\beta n_0^\beta n_i^\beta \rangle$ between site i and 0, which is at the center of the cluster. The right half of the figure shows the results gained from ED, while the left half shows the VMC results. The two methods show qualitative and even quantitative agreement, which further verifies the use of Gutzwiller approach. Fig. 6.7 shows the VMC results for different flux states, as can be seen the π-flux case provides the best energy, and the best agreement with the ED results. The Majorana-fermion calculations are motivated by [89]. This representation is based on the isomorphism between the SU(4) and SO(6) groups. The 6 Majorana fermions can be represented by three Dirac fermions. Three colors can be associated with a pair of these Dirac-fermions, while the fourth color with the absence of fermions.

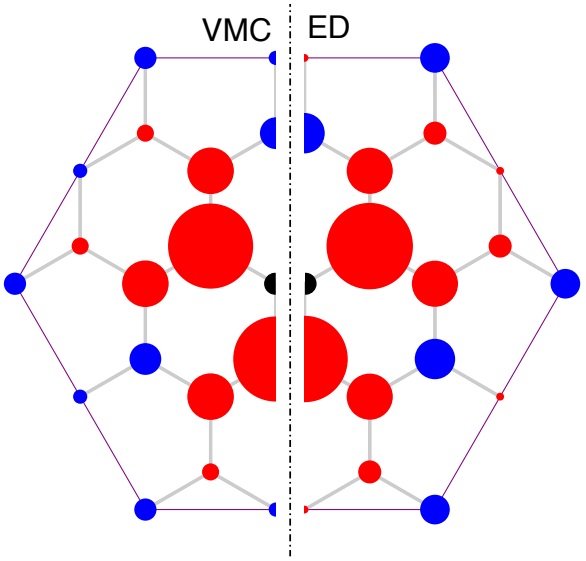

FIGURE 6.6: Comparison of color-color correlations found by exact diagonalization (carried out by Andreas Läuchli) and variational Monte Carlo calculations on an $N_s = 24$ system, the areas of the discs are proportional to $\langle \sum_\beta n_0^\beta n_i^\beta \rangle - 1/4$, where 0 is the index of the central site. The color keeps track of the sign (blue for positive, red for negative).The black dot marks site 0.

6.3.2 Color-color correlation function, structure factor in the π-flux case

The $\langle \sum_\alpha n_i^\alpha n_j^\alpha \rangle - 1/4$ correlation function shows an algebraic decay with a power of around -3.4. Fig. 6.8 displays the correlation function along chains averaged out over all six equivalent directions.

One can compare these correlations to those in a separated chain, where an algebraic decay was found as well by several methods. Fig. 6.9 shows the color-color correlations in real and in Fourier space for a single chain and along a chain in the honeycomb lattice. One can see

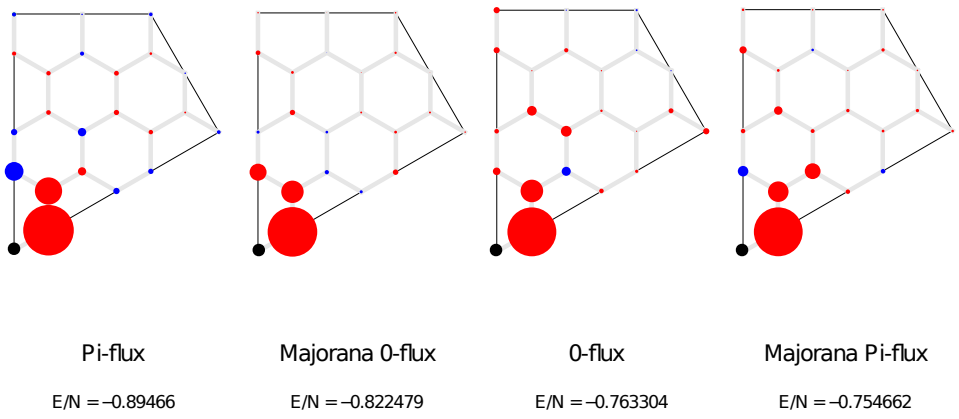

FIGURE 6.7: Comparison of color-color correlations found of different flux configurations in the $N_s = 96$ cluster. The π-flux fermion approach gives the lowest energy and the best energy with the ED results. The areas are proportional to $\langle \sum_\beta n_0^\beta n_i^\beta \rangle - 1/4$, where 0 is the index of the central site. The color keeps track of the sign (blue for positive, red for negative)

that in the honeycomb lattice the correlation function decays much faster, and there are no definite peaks in the Fourier space, instead we have cusps at $k = \pi$ and $k = \pi/2$, which is a sign of higher exponents. Fitting the data with a function like in Eq. (5.33), with k=0,π/2 and π terms we get exponents $a_0 = -2.18419 \pm 0.2406$, $a_{\pi/2} = -3.58937 \pm 0.09597$, $a_\pi = -3.68273 \pm 0.0584$, and amplitudes $b_0 = -0.0211045 \pm 0.007999$, $b_{\pi/2} = 0.671645 \pm 0.06572$ and $b_\pi = 0.148091 \pm 0.007996$.

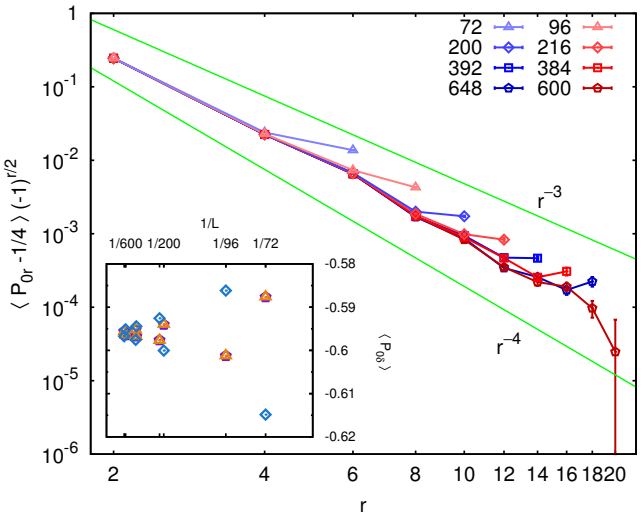

FIGURE 6.8: The decay of the color-color correlation function, along chains in the honeycomb lattice. The decay is clearly algebraic. A least-square fit gives a power of around −3.4. The inset shows the spacial asymmetry of the nearest neighbor color-color correlation, which vanishes as we increase the system size.

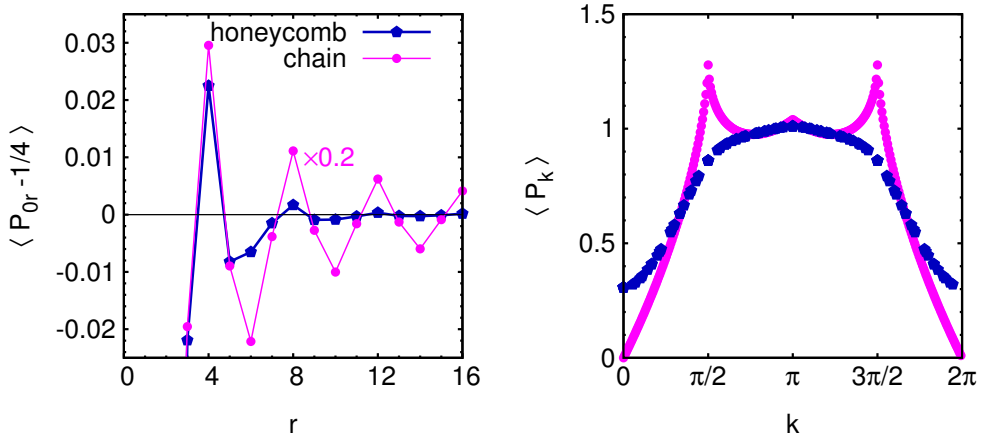

FIGURE 6.9: Comparison of the decay of the color-color correlation function in a single chain ($L = 300$), and along a chain in the honeycomb lattice ($N_s = 648$). The decay in the honeycomb lattice is much faster, and there are no peaks, like in the single chain case. The dominant exponents for a single chain are $a_{\pi/2} = -1.50 \pm 0.01$ and $a_0 = -1.86 \pm 0.16$, while for the honeycomb lattice $a_{\pi/2} = -3.58937 \pm 0.09597, a_\pi = -3.68273 \pm 0.0584$)

This algebraic decay of correlations can be captured in the structure factor as well, which can be given as $S_{\mathbf{k}} = \sum_j e^{i\mathbf{k}\mathbf{r}_j}\langle P_{0j}\rangle$, where $\mathbf{r}_j$ is the position of site j. We chose the wave vectors and the Brillouin-zone of the trianglular lattice, which we get by adding sites in the centers of hexagons in the honeycomb lattice. This way we don't need to deal with sublattice indices, and from this, one can extract the structure factor over smaller Brillouin-zones as well by folding in the parts, that lie outside of the corresponding Brillouin-zone. The conical peaks found at wave vectors corresponding to the difference of the position of Dirac-cones at quarter-filling are typical of algebraic correlations [99]. The presence of long-range order would result in sharp peaks.

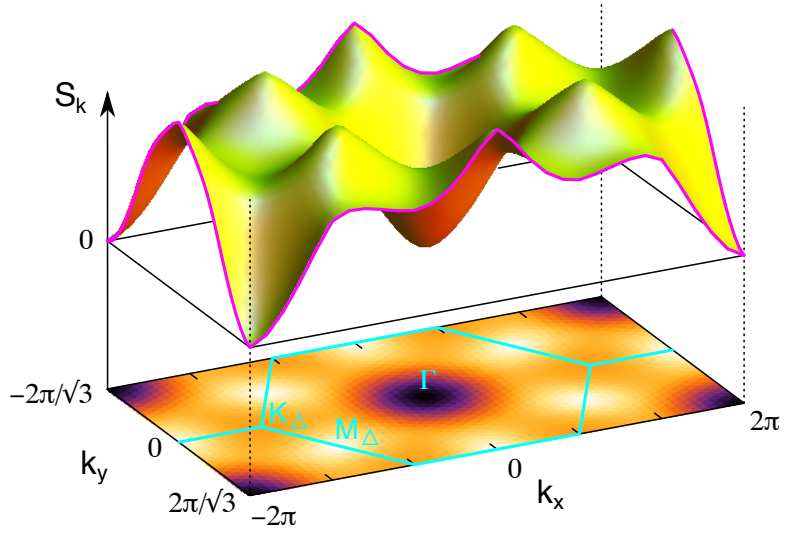

FIGURE 6.10: The structure factor of the Gutzwiller-projected π-flux state, showing conical peaks typical of algebraic correlations.

6.4 Stability of the spin-chiral liquid

While a detailed projective symmetry group classification of the SU(4) color liquid state is not yet available, the π-flux state appears to be a high symmetry liquid. Actually this would be the first example of an algebraic liquid in two dimensions. In the previous sections we discussed the correlations and energies of the Gutzwiller projected wave function when all the hoppings had the same magnitude in the π-flux free-fermionic Hamiltonian. The question naturally arises, whether some kind of ordering in the Gutzwiller projected wave function induced by changing the hopping amplitudes in the free fermionic Hamiltonian can result in a better bond energy. We checked the most probable and physically motivated orderings and found no sign of instability of the SU(4) spin liquid state. In the following we will discuss 4 cases in detail: (*i*) the formation of long range order, (*ii*) dimerization, (*iii*) chain formation and (*iv*) tetramerization. These calculations were carried out on the $\mathsf{N}_s = 96$ cluster.

6.4.1 The formation of long range order

The possibility of magnetic long range, i.e. the breaking of the SU(4) symmetry naturally arises as an instability to the spin liquid state. The presence of long-range order is indicated by a non-zero local moment

$$|m| = \sqrt{\frac{4}{3}\sum_{\alpha,\beta}\left(\langle S^{\beta}_{\alpha}\rangle - \frac{\delta_{\alpha\beta}}{4}\right)^2}, \tag{6.5}$$

where the S^{β}_{α} are the SU(4) spin operators defined in Chapter 4, and α,β run over the four different colors. $|m|$ gives its maximal value of 1 in fully ordered (i.e. site factorized) states. This formula is the SU(4) version of the SU(2) local moment, $\sqrt{\langle S_x\rangle^2 + \langle S_y\rangle^2 + \langle S_z\rangle^2}$. We considered the most plausible four-sublattice ordering shown in Fig. 6.11b, where only one color is present at each site in the fully ordered state, and which was also found by iPEPS calculations for small unit cell and low tensor dimension. Linear-flavor wave approach also predicted this as the most symmetric color-ordered classical ground state, and this color configuration has the largest weight in the Gutzwiller projected π-flux wave function as well.

We induce the SU(4) symmetry breaking in the Gutzwiller-projected variational states by introducing color dependent onsite energies (i.e. external field) in the free fermionic Hamiltonian, corresponding to the four-sublattice order. The onsite energy terms can be complemented with color dependent hopping amplitudes around the sites:

$$\Delta H_{LRO} = \sum_{\beta=1}^{4}\sum_{i\in\Lambda_\beta}\left[-\sum_{\delta}\left(\frac{t_{LRO}}{t}-1\right)\left(t_{i,i+\delta}f^{\dagger}_{i+\delta,\beta}f_{i,\beta} + h.c.\right) + \epsilon_{LRO}n^{\beta}_{i}\right] \tag{6.6}$$

where Λ_β is the sublattice where the color β is preferred in the ordered state, and δ runs through the nearest neighbor bonds. $t = |t_{i,j}|$ denotes the strength of the hopping parameters in the original free fermion Hamiltonian (6.2), where the hoppings have the same magnitude on all bonds and realize the π-flux configuration. The magnitude of the hopping parameters are modified in such a way that the amplitudes are changed for color β on the bonds connected to the sites of Λ_β. The color dependent hopping parameters break the SU(4) and spatial symmetries of the system the same way as the onsite energy terms. Fig. 6.11 illustrates the hopping amplitude and onsite energy pattern, as well as shows examples of the induced order in the projected variational wave functions.

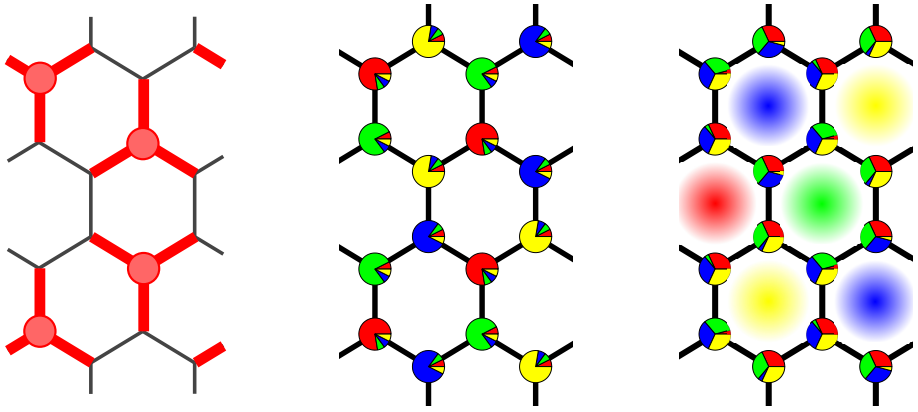

(a) (b) (c)

FIGURE 6.11: (a) The modified hopping configuration to induce long-range order for the color red. The thick red bonds show where the magnitude of the hopping parameter is changed to t_{LRO}, the red discs show where an ϵ_{LRO} onsite energy term is introduced. The free fermion Hamiltonian is modified for all colors in the same pattern, but shifted according to the four sublattice color order. (b) The color order in the projected state at $\epsilon_{\mathrm{LRO}}/t = -1$ and $t_{\mathrm{LRO}}/t = 1.4$. with $m_s = 0.702$ (c) The inverse color order for $\epsilon_{\mathrm{LRO}}/t = 1.4$ and $t_{\mathrm{LRO}}/t = 0.8$, with $m_s = -0.277$.

This induced ordering is similar to the SU(2) case, when the external field is chosen in the z direction. In this case the local moment can be written using only the diagonal spin operators: $|m| = \sqrt{\frac{4}{3}\sum_\alpha \left(\langle n^\alpha \rangle - \frac{1}{4}\right)^2}$, where n^α is the local color density for the color α.

For $-\epsilon_{\mathrm{LRO}}/t \gg 1$ and $t_{\mathrm{LRO}}/t \ll 1$ the Gutzwiller projected state is fully ordered, the low hopping amplitudes will further localize the fermions to the sites selected by the onsite energy term. For $t_{\mathrm{LRO}} = 0$ the lattice is decoupled into two separated sites and a hexagon in the unit cell for each color. The one fermion energy for a single site is $-\epsilon_{\mathrm{LRO}}$, while for a hexagon with π-flux the one fermion energy levels are $-\sqrt{3}t, 0$ and $\sqrt{3}t$, all doubly degenerate. So for $t_{\mathrm{LRO}} = 0$ and $\epsilon_{\mathrm{LRO}}/t < -\sqrt{3}$, the fermions are localized at the decoupled sites, which results in a fully ordered projected state. While, if $t_{\mathrm{LRO}} = 0$ and $\epsilon_{\mathrm{LRO}}/t > -\sqrt{3}$, the fermions prefer to stay on the hexagons, which results in the color ordering shown in Fig. 6.11c, where on each sublattice 3 colors are preferred with equal weight and in the fully ordered case $|m| = 1/3$. This ordering is further stabilized if we increase the onsite energy. We can define a signed local moment in this

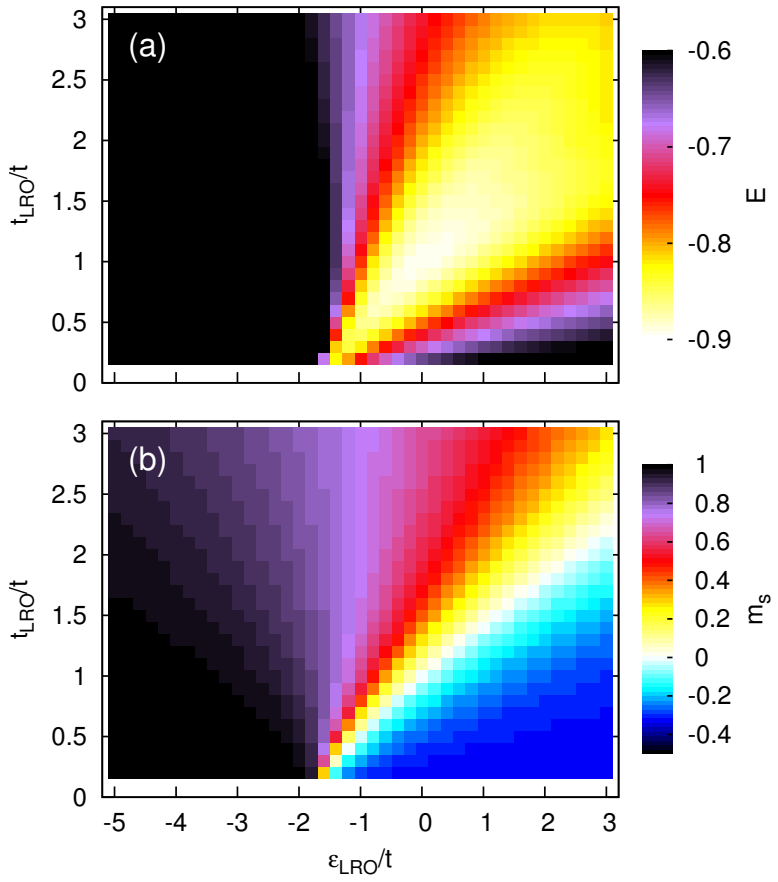

FIGURE 6.12: (a) The energy and (b) the local moment m_s of the projected state, as a function of t_{LRO} and ϵ_{LRO}. The energy is minimal for the spin liquid case.

special case to distinguish between the two scenarios:

$$m_s = \frac{1}{N_s} \sum_{\beta=1}^{4} \sum_{i \in \Lambda_\beta} (\frac{4}{3} n_i^\beta - \frac{1}{3}). \tag{6.7}$$

On every site we take the density of the preferred color, and subtract the densities of the other three colors. It can be shown that in our case $|m_s| = |m|$, but for the case when 3 colors are present of each site (i.e. repulsive onsite interaction for the "preferred" color) it gives a negative value.

Fig 6.12 shows the value of the local moment and the energy of the nearest neighbor Heisenberg model in the projected states as a function of ϵ_{LRO} and t_{LRO}. The energy is the smallest for $\epsilon_{\mathrm{LRO}} = 0, t_{\mathrm{LRO}}/t = 1$, where there is no long range order in the system, i.e. the spin liquid is stable towards the formation of long-range color order.

6.4.2 Dimerization

The SU(4) symmetric Heisenberg model on the square lattice is found to exhibit a dimerized pattern with the antisymmetric combination of 2 colors on the dimers [79]. This raises the question if a similar kind of dimerization can be energetically favorable for the honeycomb lattice as well. Dimerization, i.e. formation of bonds with stronger energies can be realized in many ways, here we consider the one which was found by iPEPS calculations with low tensor dimensions [81] (See Fig. 6.2b). In this state two colors are dimerized on bonds along a column and the other two are dimerized on adjacent similarly oriented bonds. We chose the order parameter to measure the dimerization as the difference of the dimerized and non-dimerized bond energy,

$$r_{\text{dim}} = -\left(\langle P_{i,i+\delta}\rangle_{\text{dim}} - \langle P_{i,i+\delta}\rangle_{\text{non-dim}}\right). \tag{6.8}$$

For the fully dimerized case the wave function of a dimerized bond is $|\bullet\bullet\rangle - |\bullet\bullet\rangle$ or $|\bullet\bullet\rangle - |\bullet\bullet\rangle$ and $\langle P_{i,i+\delta}\rangle_{\text{dim}} = -1$, while $\langle P_{i,i+\delta}\rangle_{\text{non-dim}} = 0$, because different sets of colors are present at the two sites of the non-dimerized bonds (see Fig. 6.13b). This dimerization pattern can be achieved by introducing color sensitive hoppings and onsite energies in the free fermionic Hamiltonian (6.2). On dimerized bonds the hopping amplitude is increased (t_{dim}) for the two dimerized colors and also a negative onsite energy (denoted by ϵ_{dim}) is introduced for these two colors. For example, on the bonds where $|\bullet\bullet\rangle - |\bullet\bullet\rangle$ is formed the hopping magnitude is increased and an onsite energy is introduced for red and green fermions.

$$\Delta H_{\text{dim}} = \sum_{\beta=1}^{4} \sum_{\langle i,j\rangle\in\beta\text{-dim}} \left[-\left(\frac{t_{dim}}{t} - 1\right)\left(t_{i,j} f^{\dagger}_{j,\beta} f_{i,\beta} + h.c.\right) + \epsilon_{dim}(n^{\beta}_{i} + n^{\beta}_{j}) \right] \tag{6.9}$$

where $\sum_{\langle i,j\rangle\beta\text{-dim}}$ runs over the $\langle i,j\rangle$ nearest neighbor bonds, on which the color β is dimerized. Fig. 6.13a illustrates the hopping parameter and onsite energy pattern, while Fig. 6.13b-c shows partially ordered projected variational wave functions. Fig 6.14 shows the order parameter r_{dim}, and the energy of the Gutzwiller projected states as we change t_{dim} and ϵ_{dim}, the shown results are averaged out over the three possible orientation of the dimerized bonds.

The energy is minimal for the $t_{\text{dim}}/t = 1, \epsilon_{\text{dim}}/t = 0$ case, where $r_{\text{dim}} = 0$, thus validating that the spin liquid is stable against this dimerization pattern dimerization as well.

If we take $t_{\text{dim}}/t > 1, \epsilon_{dim} < 0$ we enforce dimerization in the system as mentioned before. On the other hand, for small t_{dim} and negative ϵ_{dim} the order parameter is negative (see Fig. 6.14b), i.e. the bond energies along chains are stronger, and in Fig. 6.13c the chains seem completely separated. In the free fermionic Hamiltonian hoppings between chains are decreased only for two colors only, but the negative onsite energy for these two colors exclude the other two colors from the hopping process as well, which results in a separated chain-like bond energy pattern.

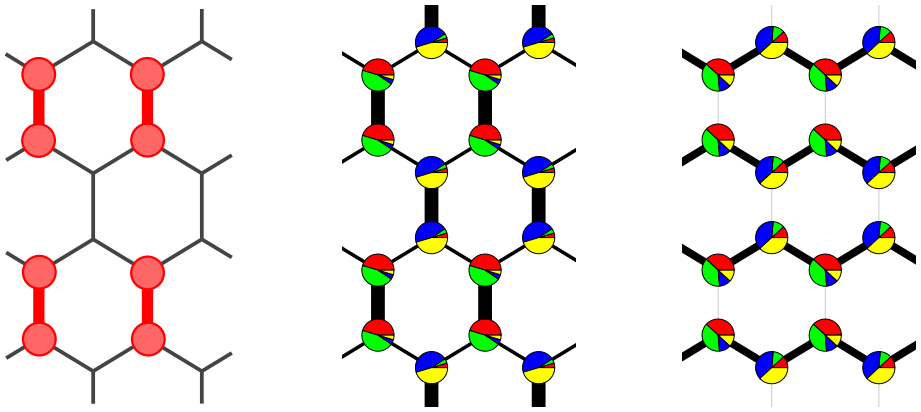

(a) (b) (c)

FIGURE 6.13: (a) The modified hopping configuration for the color red to induce dimerization . The thick red bonds show where the magnitude of the hopping parameter is changed to t_{dim}, while the red discs show where an onsite energy ϵ_{dim} is introduced for the color red. The free fermion Hamiltonian is modified the same way for the color green, while in a shifted pattern for color blue and yellow. (b) A dimerized projected state at $\epsilon_{\text{dim}}/t = -0.5$ and $t_{\text{dim}}/t = 1.6$. with $r_{\text{dim}} = 0.702$. (c) The inverse dimerized order for $\epsilon_{\text{dim}}/t = -2$ and $t_{\text{dim}}/t = 0.001$, with $r_{\text{dim}} = -0.905$. The thickness of the bonds is proportional to the square root of $\langle P_{ij} \rangle - 1/4$.

Our calculations show that the spin liquid state is stable towards this kind of ordering as well, though the chain formation should be properly studied on its own.

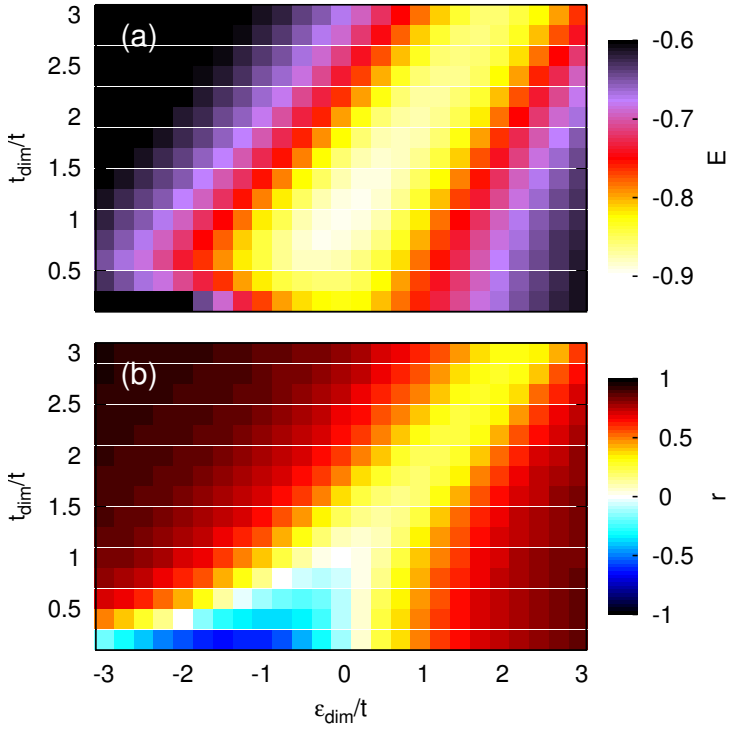

FIGURE 6.14: (a) The energy and (b) the dimerization order parameter r_{dim} of the projected state as a function of t_{dim} and ϵ_{dim}. The energy is minimal for the spin liquid case.

6.4.3 Chain formation

To study the stability towards chain formation we simply decouple chains for all colors in the free fermionic Hamiltonian:

$$\Delta H_{chain} = \sum_{\beta=1}^{4} \sum_{\langle i,j\rangle \notin chain} \left[-\left(\frac{t_{\text{nch}}}{t} - 1\right)\left(t_{i,j} f^{\dagger}_{j,\beta} f_{i,\beta} + h.c.\right)\right] \tag{6.10}$$

i.e. the hopping amplitude for bonds between chains is changed. This is similar to the previous case, where we checked the stability towards dimerization, but in this case we change the hopping parameters for all colors on bonds with the same alignment. We use the r_{dim} order parameter here as well, because it measures the difference of bond energies in chains and between chains.

In the $t_{\text{nch}} \to 0$ limit the free fermionic Hamiltonian decouples into separate chains which is reflected in the Gutzwiller projected state as well, the color-color correlation function along one direction will have the same decay as found for chains and the correlations between chains are supressed (See Fig 6.16a.)

For $t_{\text{nch}} \gg 1$ the energies of bonds between chains are smaller (larger negative), the main difference to the color-ordered dimerized case is that the Hamiltonian is not color dependent, thus there is no explicit color ordering. However, the color-color correlation shows a pattern similar to the color orderer dimerized state in the previous case (see Fig. 6.16b). The sites with positive or negative correlation are arranged in stripes, resembling to the two-color dimerized order. The strong negative correlation to the nearest neighbor in a different chain agrees with the antisymmetric pair formation found by iPEPS, and which was enforced explicitly in the previous case.

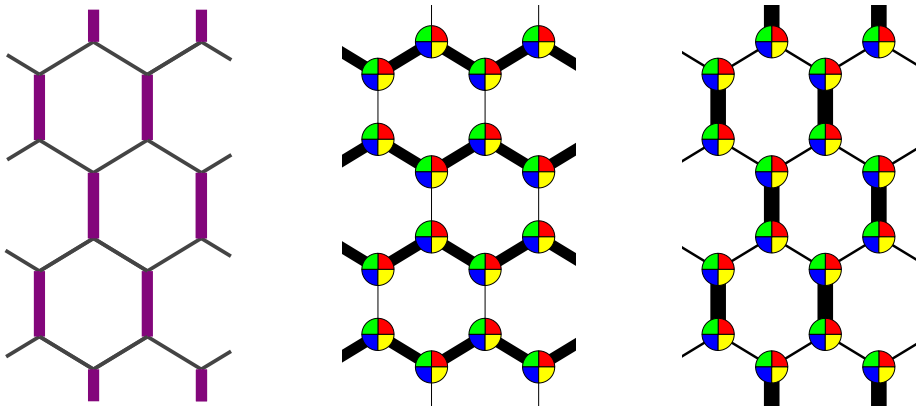

(a) (b) (c)

FIGURE 6.15: (a) The modified hopping configuration to separate chains. The thick purple bonds show where the magnitude of the hopping parameter is changed to t_{nch} for all colors. (b) The bond energies of the projected state for $t_{\text{nch}} = 0.3$. with $r_{\text{dim}} = -0.77$ (c) For $t_{\text{nch}} = 5$ the bonds between chains are stronger, here $r_{\text{dim}} = 0.74$.

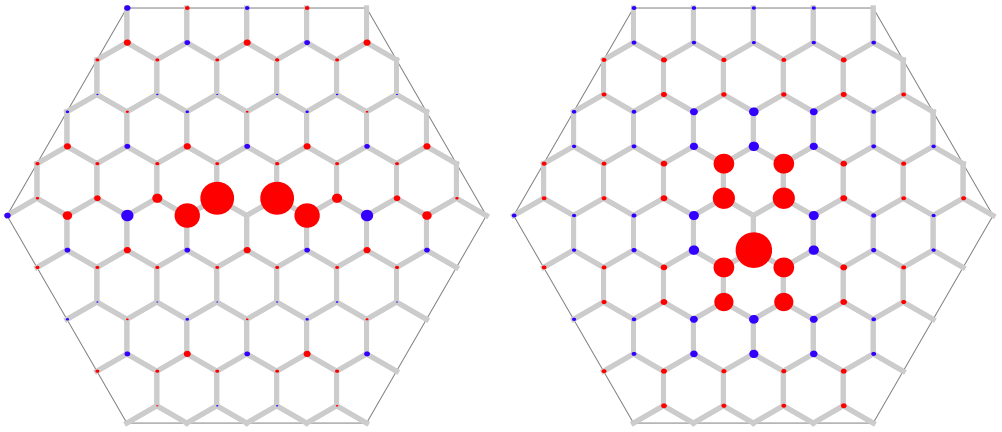

(a) (b)

FIGURE 6.16: (a) The color-color correlation function with respect to the center site in case of the chain formation. (a) shows the $t_{nch} = 0.001$ case, where the chains are separated, while (b) illustrates the $t_{nch} = 10$ case where the hopping amplitudes between chains are larger, the correlation shows similar pattern as was found in the color-ordered dimerized phase. (Compare with Fig. 6.13b)

The energy and the dimerized order parameter of the projected state as a function of t_{nch} is shown in Fig. 6.17. The energy is minimal for the $t_{\text{nch}} = 1$ case verifying once again, that the spin liquid state is stable towards chain formation (and dimerization) as well.

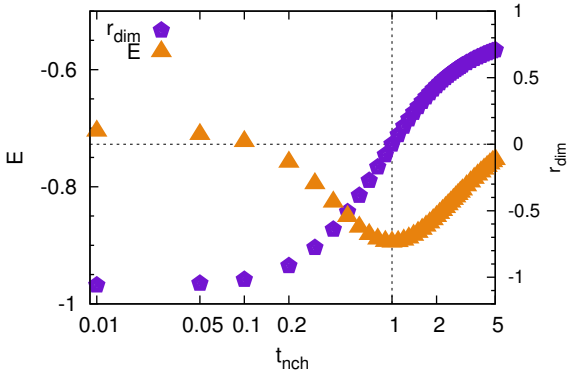

FIGURE 6.17: The order parameter r_{dim} and the energy per site and the nearest neighbor Heisenberg model as a function of t_{nch} in case of induced chain formation. The energy is minimal for $t_{nch} = 1$, where $r_{\text{dim}} = 0$

6.4.4 Tetramerization

Tetramerization refers to the formation of SU(4) singlets on the honeycomb lattice. The appearance of singlet tetramers was proved for SU(4) ladders [72], and was considered relevant in the ground state of the triangular lattices [71]. On the honeycomb lattice a site and its three

neighbors offer a viable option to accommodate an SU(4) singlet, Fig. 6.18b shows the covering of the honeycomb lattice with SU(4) singlets.

A suitable order parameter for such tetramerization is

$$r_{\text{tet}} = -\frac{4}{5}\left(\langle P_{i,i+\delta}\rangle_{\text{tet}} - \langle P_{i,i+\delta}\rangle_{\text{non-tet}}\right), \tag{6.11}$$

where $\langle P_{i,i+\delta}\rangle_{\text{tet}}$ is the average nearest neighbor bond energy in a tetramer, and $\langle P_{i,i+\delta}\rangle_{\text{non-tet}}$ is the nearest neighbor bond energy between tetramers. For the spin liquid without tetramerization r_{tet} is 0, while for the fully tetramerized state $\langle P_{i,i+\delta}\rangle_{\text{tet}} = -1$ and $\langle P_{i,i+\delta}\rangle_{\text{non-tet}} = 1/4$, so $r_{tet} = 1$. To create projected states with finite r_{tet} we modified the free fermionic Hamiltonian by strengthening the hopping amplitudes on bonds which are part of a tetramers. A negative onsite energy at the center of tetramers further stabilizes the tetramerization. The modification to the Hamiltonian reads as

$$\Delta H_{tet} = \sum_{\beta=1}^{4} \sum_{i:\text{center of tetramer}} \left[-\sum_{\delta} \left(\frac{t_{\text{tet}}}{t} - 1\right)\left(t_{i,i+\delta} f^{\dagger}_{i+\delta,\beta} f_{i,\beta} + h.c.\right) + \epsilon_{\text{tet}} n_i^{\beta} \right]. \tag{6.12}$$

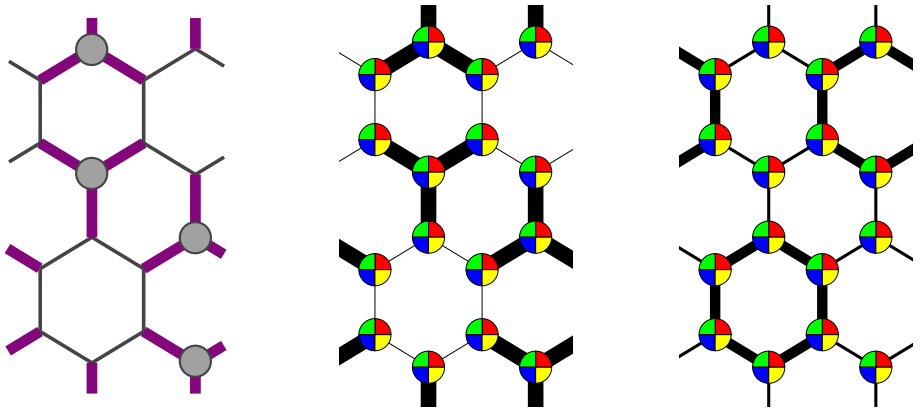

(a) (b) (c)

FIGURE 6.18: (a) The modified hopping configuration to induce tetramerization. The thick purple bonds show where the magnitude of the hopping parameter is changed to t_{tet}, the grey discs show where an onsite energy ϵ_{tet} is introduced. The free fermion Hamiltonian is color independent, it is modified for every color in the same way. (b) A tetramerized projected state at $\epsilon_{\text{tet}}/t = -3$ and $t_{\text{tet}}/t = 1.6$. with $r_{\text{tet}} = 0.859$ (c) The variational wave function for $\epsilon_{\text{tet}}/t = 2$ and $t_{\text{tet}}/t = 0.5$, with $r_{\text{tet}} = -0.366$.

Fig. 6.18 shows the pattern of hopping parameters and onsite energies along with partially tetramerized projected variational states. This type of ordering is relevant, since it opens a gap at the Fermi-level and removes the Dirac point at quarter filling [100]. Fig. 6.19 shows r_{tet}, and the nearest neighbor bond energy per site of the projected state as we change ϵ_{tet} and t_{tet}. For large t_{tet} the fermions prefer to hop on the bonds of separated tetramers, thus resulting a projected wave function with SU(4) singlets. For small t_{tet} the bond energies around hexagons

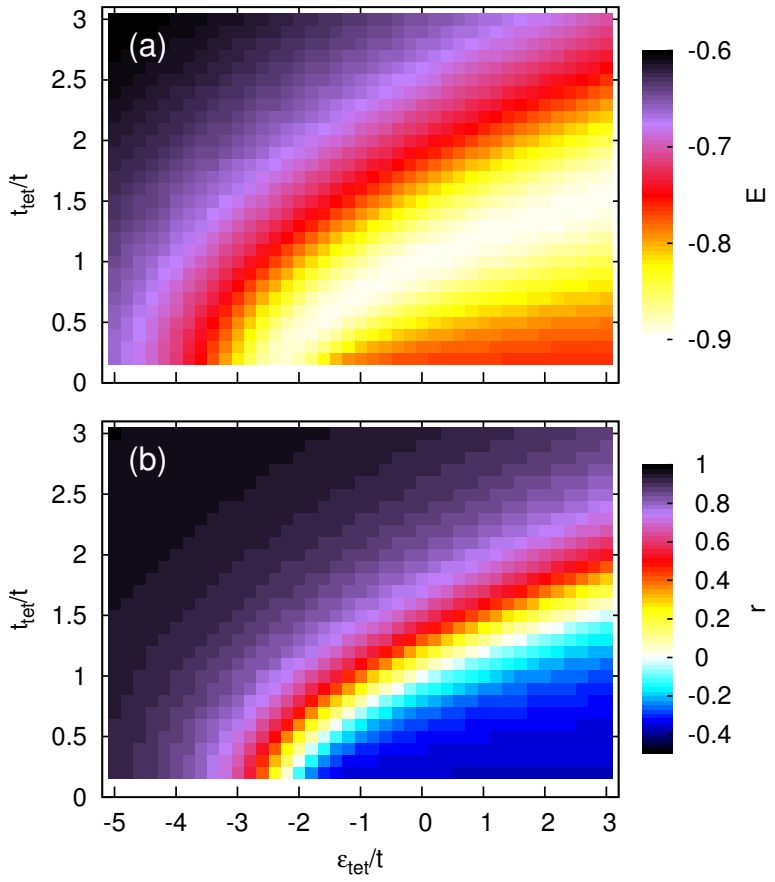

FIGURE 6.19: (a) Energy and (b) the tetramerized order parameter, r_{tet} of the projected state as a function of t_{tet} and ϵ_{tet}. The energy is minimal for the spin liquid case.

are stronger (see Fig 6.18c). The energy is minimal for the spin liquid state at the $\epsilon_{tet} = 0$ and $t_{tet}/t = 1$.

6.5 A model with tetramerized exact ground state

We can construct a Hamiltonian for which the tetramerized state suggested in the previous section is an exact ground state. In this state the lattice is covered with SU(4) singlets as shown in Figs. 6.18b or 6.20a. The $\langle P_{i,j} \rangle$ bond energy between sites belonging to the same singlet is -1, and equals to $1/4$ between sites of different singlets.

We considered the operator

$$Q_{(ij),(kl)} = \frac{1}{4}(1 + P_{ij})(1 + P_{kl}) \tag{6.13}$$

where P_{ij} is the SU(4) Heisenberg exchange. This operator is a projection, i.e. $Q_{(ij),(kl)} = Q^2_{(ij),(kl)}$, therefore it has eigenvalues0 and 1. It gives 0 if the wave function is antisymmetric

either on the (i, j) or the (k, l) bonds, and 1 if the wave function is symmetric on both bonds. If we choose (i, j) and (k, l) to be nearest neighbor parallel bonds as shown in Fig 6.20a, one of the two bonds will be always part of an SU(4) singlet in the fully tetramerized state. The Hamiltonian constructed as the sum of the operators,

$$\mathcal{H}_Q = \sum_{(ij),(kl)} Q_{(ij),(kl)}, \tag{6.14}$$

is a sum of projection operators, therefore the ground state energy must be non-negative. The tetramerized state introduced in the previous section is a ground state of this model, since it gives 0 with all $Q_{(ij),(kl)}$.

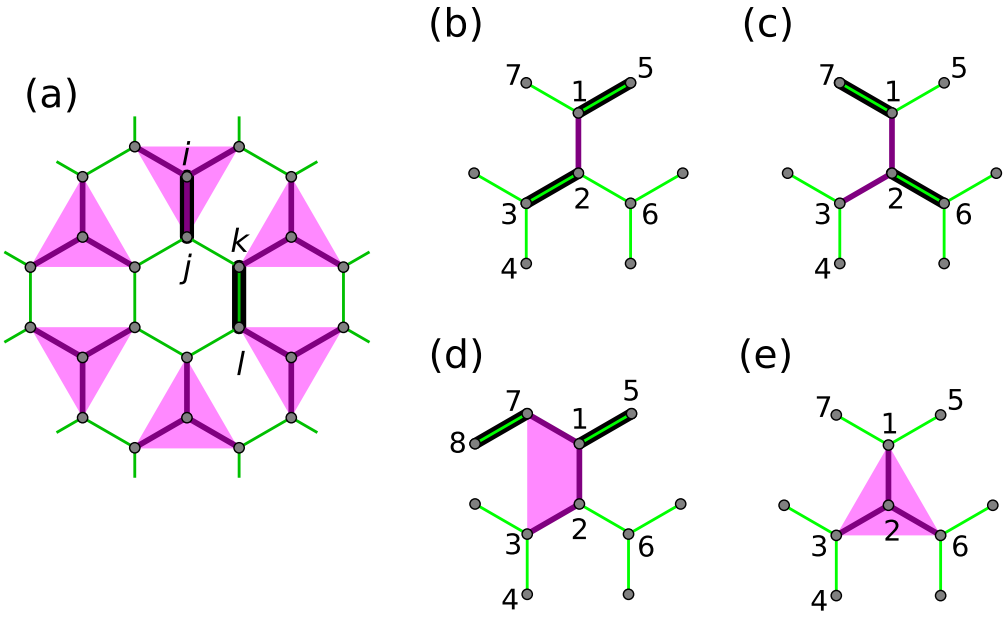

FIGURE 6.20: (a) $Q_{(ij),(kl)}$ with nearest neighbor parallel (ij) and (kj) bonds in the tetramerized state, (b)-(e) illustrates that this kind of covering is the only ground state of $\mathcal{H}_Q$ in Eq. (6.14) (b) To satisfy $Q_{(12)(34)}$ (12) is antisymmetrized (purple bond), next to satisfy $Q_{(15)(23)}$ we antisymmetrize (23). (c) To satisfy $Q_{(17)(26)}$ we can't make an antisymmetrization in (17), since then we will be unable to satisfy $Q_{(15)(78)}$ (d), so the only option we have is an SU(4) singlet located on site 2 and its three neighbors (e).

We can also prove that no other SU(4) singlet covering state satisfies all Q projections. Here we follow the site numbering shown in Fig 6.20b-e. To make $Q_{(12)(34)}$ satisfied, we can choose to antisymmetrize the spins on bond (12). Next, to make $Q_{(15),(23)}$ satisfied we can either antisymmetrize the spins on bond (15) or (23). Without loss of generality we can choose to antisymmetrize on (23). Now, consider $Q_{(17),(26)}$. If we make an antisymmetrization on (17), then we created an SU(4) singlet on sites 1,2,3 and 7. At this point, the $Q_{(15),(78)}$ term can not be satisfied, since 1 and 7 already belong to a singlet, so we cannot make an antisymmetrization neither on (15) nor (78). Therefore, instead of (17) we must make an antisymetrization on bond (26), which then results a singlet on sites 1,2,3 and 6. This shows that a ground state of $\mathcal{H}_Q$ must be built of singlets occupying a site and its three neighbors, which can be done only as shown

in Fig 6.20a. This type of SU(4) singlet covering is fourfold degenerate depending on where the centers of the singlet tetramers are located.

6.5.1 Transition between the spin liquid and the tetramerized phase

The Hamiltonian

$$\mathcal{H}_\eta = (1-\eta)\sum_{(ij)} P_{ij} + \eta \sum_{(ij),(kl)} Q_{(ij),(kl)} = \sum_{(ij)} P_{ij} + \frac{\eta}{4}\sum_{(ij),(kl)} \left(1 + P_{ij}P_{kl}\right) \tag{6.15}$$

connects the spin liquid and tetramerized phases. For $\eta = 1$, $\mathcal{H}_\eta = \mathcal{H}_Q$, while for $\eta = 0$ we recover the nearest neighbor SU(4) Heisenberg model (6.1). The transition between the two cases can be studied using the Gutwiller projected wave functions. As we showed in Chapter 5, the $\langle P_{ij}P_{kl}\rangle$ quantities can be calculated for the Gutzwiller projected wave functions using Monte Carlo algorithm. This allows us to compare the energies of $\mathcal{H}_\eta$ for variational wave functions with different levels of tetramerization. We made calculations for systems with N_s = 24, 96, 216, and 384 sites, Fig. 6.21 shows the value of the order parameter r_{tet} of the lowest energy state as a function of η. The transition between the liquid and tetramerized case strongly depends on the system size, the finite size scaling of the transition point suggests, that in the thermodynamical limit the tetramerized phase might reach the $\eta = 0$ point. The type of the transition seems to be of first order, which is supported by the energy versus order parameter plot at near the transition point, clearly showing two local minima, corresponding to the $r_{\text{tet}} = 0$ liquid and a partially tetramerized state (see the inset of Fig. 6.21).

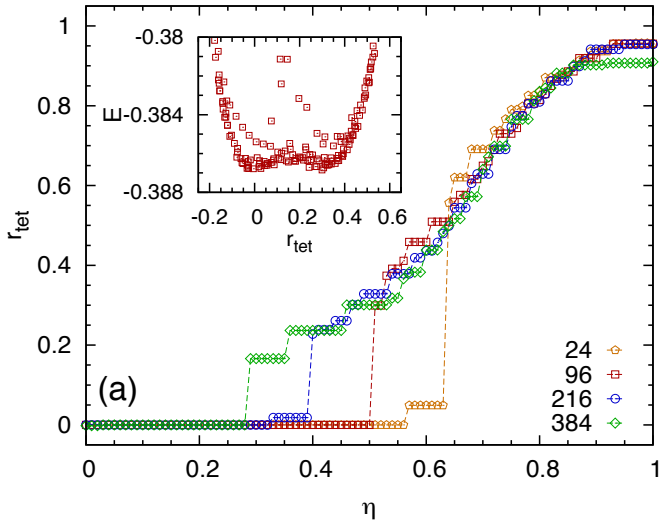

FIGURE 6.21: The tetramerization order parameter r as a function of η in the model given by Eq. (6.15). In the inset we show the energy at $\eta = 0.5$ as a function of the order parameter for the Gutzwiller projected variational states for the $\mathsf{N}_s = 96$ system.

6.5.2 Tetramerization induced by next nearest exchange

Extending the nearest neighbor Heisenberg model with next nearest neighbor exchange increases the number of bonds within a singlet tetramer, but also the bonds between tetramers, so it is not clear, if this leads to tetramerization. The nearest and next nearest bond energies in spin liquid case are $\langle P_{i,i+\delta}\rangle = -0.596$, and $\langle P_{i,i+\delta_2}\rangle = 0.005$, so the energy per site is $E = -0.894J_1 + 0.015J_2$. In the fully tetramerized case the nearest and next nearest bond energies are -1 or 1/4 depending on whether the bond is part of a singlet or not, thus the energy per site of the system is $E = -9J_1/16 + 3J_2/16 = -0.5625J_1 + 0.1875J_2$. Comparing these two energies, we learn that for sufficiently large J_2, tetramerization becomes favorable (for $J_2 \geq 1.6J_1$). Considering partially tetramerized variational wave functions we can get a better picture of the transition between the spin liquid and tetramerized phase as a function of J_2.

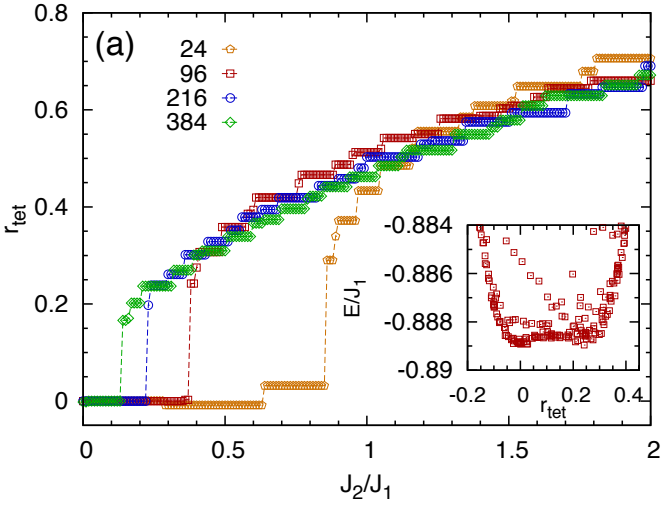

FIGURE 6.22: The tetramerization order parameter as a function of J_2/J_1 in the model with next nearest exchange J_2. The inset shows the energy versus the order parameter near the transition for the $N_s = 96$ system ($J_2/J_1 = 0.38$), the two local minima shows that the transition is of first order.

Fig. 6.22 shows the order parameter as a function of J_2/J_1, while $J_1 > 0$. The transition point is again strongly depends on the system size.

6.5.3 Further verification for the stability of the spin liquid ground state

Our findings for the transition between the liquid and tetramerized phase calls for a more detailed study of the nearest neighbor Heisenberg model, to verify that the spin-orbital liquid remains stable in the thermodynamic limit. To this end, we plot the energy of the nearest neighbor Heisenberg model of Eq. (6.1) as a function of the tetramerization order parameter for different

system sizes (N_s = 24, 96, 216, 384). We fitted the energy curve by the

$$E_{\text{fit}} = E_0 + c_2 r_{\text{tet}}^2 + c_3 r_{\text{tet}}^3 + c_4 r_{\text{tet}}^4 \tag{6.16}$$

trial function. The results of the fit for different system sizes are shown in Fig. 6.23, together with the size dependence of the fitting parameters. We are primarily interested if $r = 0$ remains the lowest energy state. To confirm that E_0 is the lowest energy we examine the sign of $E - E_0 = r_{\text{tet}}^2(c_2 + c_3 r_{\text{tet}} + c_4 r_{\text{tet}}^2)$. If it is positive for all $r_{\text{tet}} \neq 0$, i.e. the discriminant of the $c_2 + c_3 r_{\text{tet}} + c_4 r_{\text{tet}}^2$ is negative, then $r = 0$ is clearly the global minimum of Eq. (6.16) with an energy of E_0. The phase transition occurs when the discriminant becomes 0. We plotted the discriminant as a function of the inverse size in Fig. 6.23(e). It appears that the discriminant remains finite and negative even in the $N \to \infty$ thermodynamic limit. In other words, the variational calculation seems to confirm stability of the algebraic liquid against tetramerization. This argument verifies the stability of the spin-orbital liquid state for the simple nearest neighbor Heisenberg model. We note that in case of the the analysis of the transition to the tetramerized phase, the transition points are determined by tiny energy differences (that may depend on the details of calculations, such as boundary conditions), so we should be cautious when performing finite-size scaling of the transition point.

We note that the case of tetramerization is special among the different orderings. In this case the change of hopping parameters and the introduction of onsite energies open a gap in the Fermi surface. However, the ϵ_{tet} and t_{tet} can be changed simultaneously in Eq. (6.12), to restore the Dirac point at the Fermi surface. Similar feature can be seen in the energy versus order parameter plot in Fig. 6.23a, where the bulk of the points fall on a single curve, i.e. variational states with different ϵ_{tet} and t_{tet} have similar energies and orderings after the Gutzwiller projection. Furthermore, in the Fig. 6.19a, a valley can be seen in the energy as a function of ϵ_{tet} and t_{tet}. We don't understand the origin of these properties yet, but they all show that the effect of Gutzwiller projection is not trivial in this case, and further study might reveal the connection between the effect of the different parameters and the findings in the liquid-tetramerizaiton transition. Also, other methods could provide a clearer understanding of the stability of the spin-orbital liquid phase.

6.6 $J_1 J_2 J_3$ Heisenberg model on the honeycomb lattice

In the previous sections we studied the nearest neighbor SU(4) symmetric Heisenberg interaction on the honeycomb lattice. We collected the numerical evidence that supports the algebraic nature of the liquid state and checked the stability towards the most plausible ordering. We saw that if we extend the nearest neighbor Heisenberg model to contain other interactions as well, the spin liquid state is not necessarily stable anymore. In this section we will extend the Monte Carlo

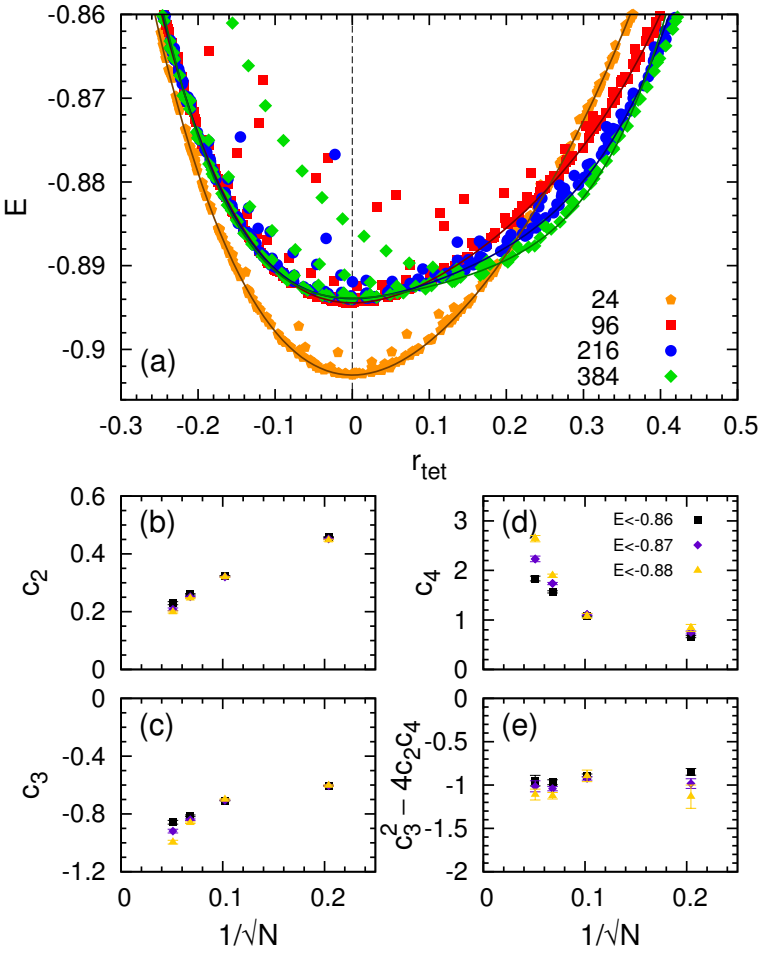

FIGURE 6.23: (a) The energy $E = 3\langle P_1 \rangle/2$ as a function of the tetramerization parameter for 24, 96, 216, and 384 site clusters, together with a fit based on Eq. (6.16) using the points that are below the energy threshold -0.87. In (b)–(d) we plot the fitting parameters for the energy thresholds -0.86, -0.87, and -0.88, as a function of $1/\sqrt{N}$, where N is the size of the system. (e) The finite size dependence of the discriminant.

study to a more general Heisenberg model with next nearest (J_2), and third nearest neighbor (J_3) interactions as well:

$$\mathcal{H} = J_1 \sum_{\langle i,j \rangle} P_{i,j} + J_2 \sum_{\langle\langle i,j \rangle\rangle} P_{i,j} + J_3 \sum_{\langle\langle\langle i,j \rangle\rangle\rangle} P_{i,j},. \tag{6.17}$$

A basic phase diagram can be drawn by comparing the bond energies of the spin liquid and the fully ordered states. In the spin liquid case, the energy per site is found as $E_{\mathrm{SL}} = -0.895J_1 + 0.015J_2 + 0.549J_3$. For the fully color ordered state with four-sublattice order (Fig. 6.11b) the nearest and next nearest bond energies are 0, while the third nearest bond energy is +1, hence the energy per site is $E_{\mathrm{LRO}} = 3J_3/2$. In the dimerized color-ordered case (Fig. 6.13b), the nearest neighbor bond energy is -1 for the dimerized bonds and 0 for the non-dimerized ones. The next-nearest-neighbor bond energy is $1/2$ for two of the next nearest neighbors, and 0 for the other four, where different colors are present. The third nearest neighbor bond

energy is always 1/2. Hence the energy per site in the dimerized case is $E_{\text{dim}} = -J_1/2 + J_2/2 + 3J_3/4$. In case of chain formation (Fig. 6.15b), the nearest and next nearest bond energy along a chain is -0.823 and -0.365 based on the Gutzwiller projected calculations for chains, that we presented at the end of Chapter 5, the bond energies of nearest, next nearest and third nearest bonds between chains are always $1/4$. Thus, the energy per site for chain formation is $E_{\text{chain}} = -0.698J_1 + 0.1358J_2 + 3J_3/8$. Finally in case of tetramerization (Fig. 6.18b) the energy per site is $E_{\text{tet}} = -9J_1/16 - 3J_2/16 + 3J_3/8$, as discussed earlier. Note that the third nearest neighbor bonds always connect sites belonging to different singlets thus the bond energy for these is 1/4.

According to the above energies a basic phase diagram is shown in Fig. 6.24a. As can be seen, for strongly ferromagnetic J_3 the SU(4) symmetry breaking, long-range ordered state takes over, because in that case the third nearest bond energy is the highest possible (+1). For antiferromagnetic J_2, the tetramerized order is preferred, as we discussed before, while for ferromagnetic J_2 the dimerized scenario is chosen. The formation of chains is selected for ferromagnetic J_2 and antiferromagnetic J_3.

This phase diagram can be improved if we consider states with partial orderings. We considered all the projected states with different types of orderings, that we discussed in the previous section, and calculated the nearest, next-nearest and third next nearest bond energies as well. For arbitrary value of J_1, J_2 and J_3 one can select the variational projected state with lowest energy among all the possibilities (see Fig. 6.24b).

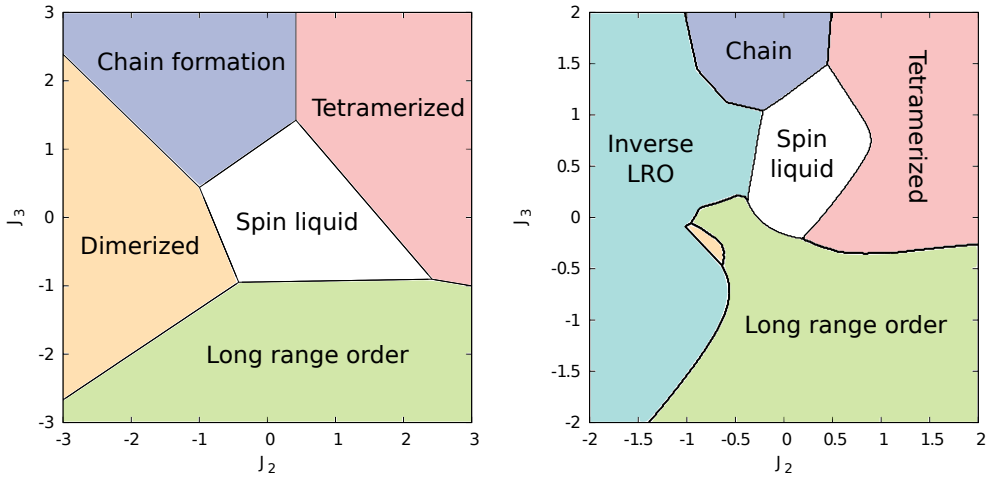

FIGURE 6.24: (a) The phase diagram of the $J_1J_2J_3$ Heisenberg-model based on the comparison of the energies of the fully ordered states. (b) The phase diagram considering all, partially ordered Gutzwiller projected states.

As could be anticipated, the size of the spin liquid regime is much smaller. Surprisingly, the dimerized phase disappears and its place is taken over by the inverse long range ordered state

discussed in subsection 6.4.1, and depicted in Fig. 6.11c.

We must emphasize, that the results of this phase diagram should be taken with care, since we only considered a few types of orderings, and sometimes the variational energies are really close to each other (for example for ferromagnetic J_2 the energies of the inverse long range ordered and the dimerized cases). Moreover, these orderings can be induced with different modification of the free-fermionic Hamiltonian, which might give different variational projected states, and different energies. Also, we didn't considered states with multiple orderings, which might provide insight into the transition between the different orderings. Nonetheless, these phase diagrams show, that the spin liquid state is stable for finite J_2 and J_3 interactions as well, not just for the nearest neighbor Heisenberg model.

6.7 Conclusions

The numerical results of linear flavor wave theory and iPEPS calculations on the absence of lattice and SU(4) symmetry breaking provide strong evidence that the ground state of the nearest neighbor SU(4) symmetric Kugel-Khomskii model on the honeycomb lattice is a spin-orbital liquid. The findings of the π-flux variational Gutzwiller projected states support this claim, and further shows that the ground state is in fact an algebraic spin-orbital liquid. The usage of the Gutzwiller approach can be verified by the comparable energies to iPEPS results, and the excellent agreement with exact diagonalization results.

We further showed that the spin-orbital liquid ground state is stable against the most plausible and relevant orderings, like the formation of SU(4) symmetry breaking long-range order, dimerization or SU(4) singlet formation. In all cases we found that the spin-orbital liquid case is stable.

We can also examine models with longer range or higher order interactions in the Gutzwiller approach. We showed this through the example of the SU(4) singlet formation, where a Hamiltonian can be constructed that exhibits these tetramerized states as exact ground states. The transition can be studied by variational states with different extend of ordering. Our calculations show that the tetramerized SU(4) singlet- plaquette state, next to the algebraic color-liquid state, appear to be a strong ground-state candidate for the four-component Mott insulating state on the honeycomb lattice at zero temperature, and its realization may depend on fine details of the effective Heisenberg model. So far exact diagonalization, and iPEPS calculations showed no sign of tetramerization, but in the light of our results further studies are needed, to provide a clearer picture.

We also carried out calculations considering the $J_1J_2J_3$ model, and found that the spin-orbital liquid found in the $J_2 = J_3 = 0$ case is stable for finite values of J_2 and J_3 as well. This

further strengthens the experimental relevance of our findings, since it shows the robustness of the spin-orbital liquid behavior.

Chapter 7

SU(3) Heisenberg model on the honeycomb lattice

In the literature there are conflicting results on the ground state structure of the SU(3) Heisenberg model on the honeycomb lattice. The linear flavor wave approach predicts a dimerized order with an 18-site unit cell, depicted in Fig. 4.2a [80]. Tensor renormalization group method shows plaquette ordering with a 6-site unit cell [101], where bonds around separated elementary hexagonal plaquettes are stronger. These two scenarios have not been tested against each other, the order by disorder approach is not variational, thus its energies cannot be compared to the tensor network algorithm results, and the 18-site unit cell which is compatible with dimerized order has not been considered in the tensor network study.

In the following sections we will undertake a more systematic study of the ground state structure using the Gutzwiller projection approach. These results complement the findings of a thorough iPEPS calculation in the system [102].

7.1 iPEPS results, dimerization vs. hexamerization

For an 18-site unit cell with low tensor dimensions ($D = 2$), a dimerized structure was found with SU(3) symmetry breaking. On each site one color is dominant, and antisymmetric pairs of colors are formed on the dimerized bonds (See Fig. 7.1a). This is similar to the dimerized state predicted by LFWT. In case of a 6-site unit cell a plaquette state is found, where low-energy bonds are formed around hexagons without any sign of color ordering (Fig. 7.1b). For small tensor dimensions the dimerized case has a lower energy, but the energy of the hexamerized case decreases faster, and for large tensor dimensions it becomes energetically preferable (Fig 7.1c).

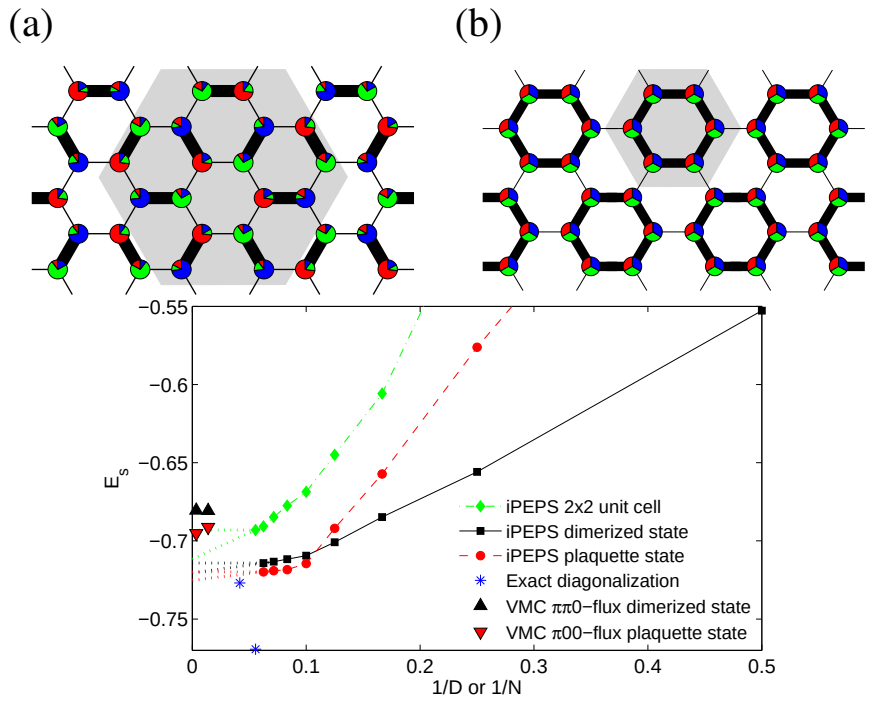

FIGURE 7.1: Orderings found by iPEPS calculations, (a) Dimerized order found for the 18-site unit cell, with SU(3) symmetry breaking. (b) Plaquette order found on a 6-site unit cell, without sign of color order. (c) Energies of iPEPS calculations as a function of tensor dimension. For $D \leq 8$ the dimerized color ordered state has lower energy, but for $D \geq 8$ the plaquette ordering is energetically favorable [102].

7.2 Different flux configurations

In the SU(3) case the iPEPs results show that the translation invariance of the system is broken, therefore we will consider non-uniform flux configurations as well. The different flux states are illustrated in Figure 7.2, in the following we give a detailed description of the considered scenarios.

1. Two configurations with 0 flux in a central hexagon and 0 or π flux in the adjacent hexagons called respectively 000 and $0\pi\pi$–flux states (Fig. 7.2 a-b) [103]. These states are compatible with a 6-site unit cell. In this gauge, the hopping amplitudes around the central hexagon are set to t_h, while they alternate between t_h and t_d as one goes around the two remaining hexagons in the unit cell. The motivation to study these states comes from the tensor network simulations of [101] as well as the iPEPS calculations on the six-site unit cell (Fig. 7.1b).

2. Two configurations with π-flux in a central hexagon and 0 or π flux in the adjacent hexagons called respectively $\pi 00$ and $\pi\pi\pi$–flux states (Fig. 7.2c-d). The realization of these layouts requires a larger hexagonal unit cell of 24 sites. These configurations are

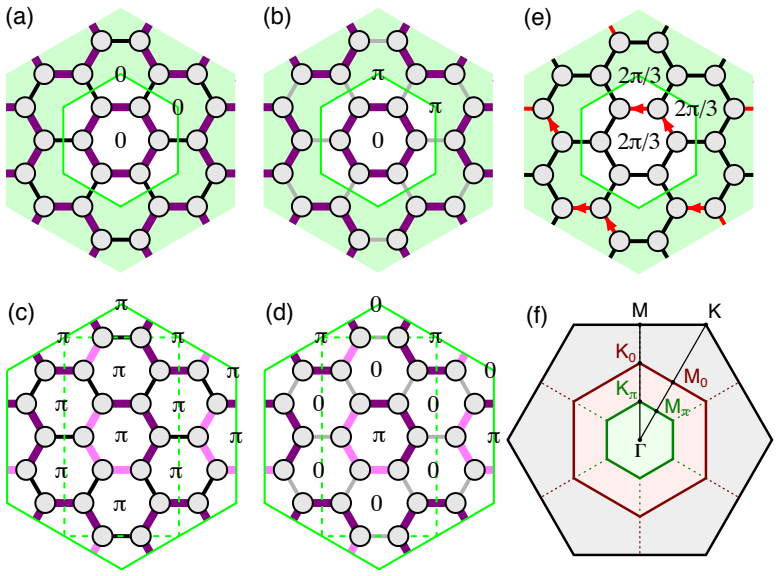

FIGURE 7.2: (a) The 000–flux and (b) the $0\pi\pi$–flux states, with 6 sites and 3 hexagons in the unit cell. (c) The $\pi\pi\pi$–flux and (d) the $\pi 00$–flux states have 12 sites in the primitive unit cell (shown by dashed rectangle) or 24 sites in the hexagonal unit cell. These 4 configurations are characterized by two different absolute values of hopping amplitudes, t_d and t_h. The hopping amplitudes on the thin black and grey bonds are t_d and $-t_d$, while on the thick dark and light purple bonds the hopping amplitudes are t_h and $-t_h$, respectively. (e) The chiral $\Phi\Phi\Phi$–flux state with $\Phi = 2\pi/3$. The red bonds with arrows denote hoppings with complex $t_h e^{i2\pi/3}$ amplitudes. Here one can also introduce a modulation for the hoppings by changing the sign on the bonds crossing the boundaries of the unit cell (t_d bonds), resulting in a $\Phi\Phi'\Phi'$ flux configuration, with $\Phi' = 5\pi/3$. Also $\Phi'\Phi'\Phi'$ and $\Phi'\Phi\Phi$ flux configurations can be created by introducing complex hoppings to the $\pi\pi\pi$ and $\pi 00$ case. (f) Brillouin zone of the honeycomb lattice (black hexagon) with the high symmetry points $\Gamma = (0,0)$, $\mathsf{K} = (2\pi/3\sqrt{3}, 2\pi/3)$, and $\mathsf{M} = (0, 2\pi/3)$. The Brillouin-zone of the 6-site unit cell flux states (000, $0\pi\pi$, $\Phi\Phi\Phi$, and $\Phi\Phi'\Phi'$) shown by the dark red hexagon, with the high symmetry points $\mathsf{K}_0 = (0, 4\pi/9)$ and $\mathsf{M}_0 = (2\pi/3\sqrt{3}, 2\pi/6)$. The dark green hexagon stands for the Brillouin-zone of the 24-site unit cell of the $\pi\pi\pi$, $\pi 00$, $\Phi'\Phi'\Phi'$, and $\Phi'\Phi\Phi$–flux configurations with $\mathsf{K}_\pi = (0, 2\pi/9)$ and $\mathsf{M}_\pi = (\pi/3\sqrt{3}, \pi/6)$. The index in M and K refers to the flux of the central hexagon realized by real hopping amplitudes. The nearest-neighbor distance is chosen to be unity.

motivated by the results of the SU(4) case on the honeycomb lattice [81], where a uniform π-flux configuration gave a variational state energetically comparable to the iPEPS results.

3. A uniform chiral $\Phi\Phi\Phi$–flux state with $\Phi = 2\pi/3$ per hexagon (Fig. 7.2e), following the mean–field results for the SU(6) Heisenberg model on the honeycomb lattice [82], as well as the uniform $\Phi'\Phi'\Phi'$–flux state, where $\Phi' = 5\pi/3$. Both uniform flux states can be modulated to achieve a $\Phi\Phi'\Phi'$ and a $\Phi'\Phi\Phi$ flux configuration. The states with Φ flux in the central hexagon can be realized in the 6-site unit cell, while the states with Φ' flux require a 24 site hexagonal unit cell. We note that, these constructions can be only achieved by complex hoppings, while the other four flux-states can be realized with real hopping parameters.

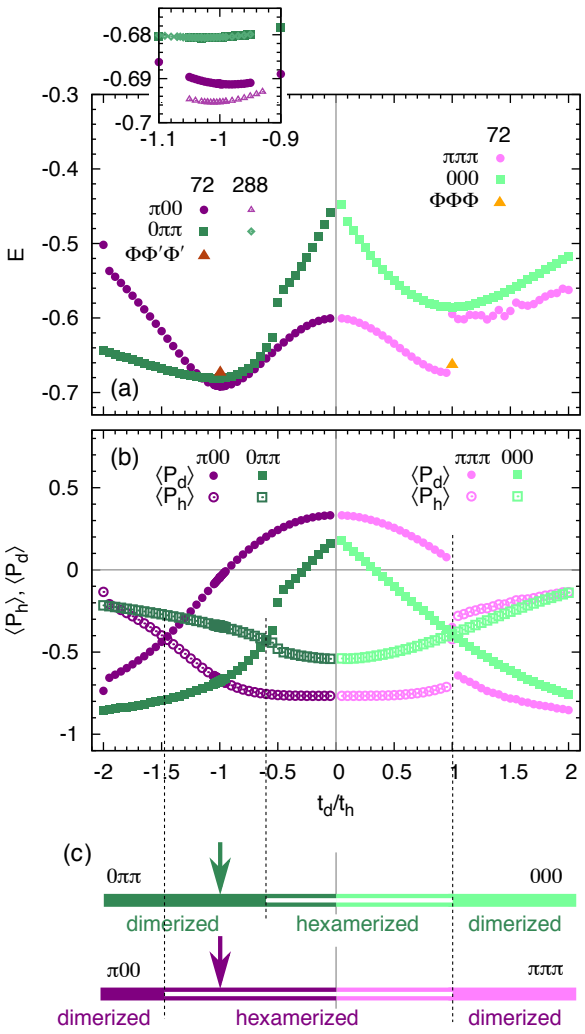

FIGURE 7.3: (a) Nearest-neighbor bond energy as a function of t_d/t_h in the 72 site cluster. As we change the sign of t_d/t_h from negative to positive, we shift between the $0\pi\pi$–flux and 000–flux states (green squares), or between the $\pi 00$–flux and $\pi\pi\pi\pi$–flux states (purple circles). The energy of the chiral $\Phi\Phi\Phi$–flux state with $\Phi = 2\pi/3$ ($E(\Phi\Phi\Phi) = -0.662$) is compared to the $t_d = t_h$ case, while the energy of the chiral $\Phi\Phi'\Phi'$–flux state $E(\Phi\Phi'\Phi') = -0.671$ is compared to the $t_d = -t_h$ case. The $\Phi'\Phi'\Phi'$–flux and $\Phi'\Phi\Phi$–flux states have a higher energy ($E(\Phi'\Phi'\Phi') = -0.604$, $E(\Phi'\Phi\Phi) = -0.629$). The inset of (a) shows the energies around $t_d/t_h = -1$ for the 72 and 288 site clusters. The free fermion Fermi-sea state is degenerate for the $\pi\pi\pi$–flux state at the Fermi level when $t_d/t_h > 1$, and this is the origin of the scattered energy values of the projected state. (b) The energies of the d and h bonds versus t_d/t_h. The hexamerization ($\langle P_h\rangle < \langle P_d\rangle$) is more extended for the $\pi 00$–flux state than for for the $0\pi\pi$–flux state. (c) Schematic drawing of the extension of the hexamerized (plaquette) and dimerized phases that can be read off from the bond energies given in (b). The arrows denote the minima of the energies shown in (a).

For the 000-$0\pi\pi$ and $\pi\pi\pi$-$\pi 00$ cases we made calculations for different values of t_d/t_h, with fixed $t_h > 0$. If t_d changes sign, the flux of the central hexagon remains the same, while the flux of the other hexagons around change by π.

7.3 VMC results

For the Gutzwiller-projected calculations we chose finite clusters that have the full symmetry of the honeycomb lattice and are compatible with both the 6 and 18-site unit cell of the iPEPS calculations, and with the 24-site unit cell of the $\pi\pi\pi$ and $\pi 00$ flux-configurations. The bulk of the calculations were made on clusters with 72 sites, and around the minimal energies we made calculations on systems N_s =288. The number of elementary Monte Carlo steps was $10^{10}(2 \cdot 10^{10})$ for N_s =72 (288), and the sampling distance was chosen to be 1000(10000) which is around 5 times the correlation length.

Among all states that we have investigated, the $\pi 00$-flux configuration provides the lowest energy per site, -0.6912 on the 72-site cluster. The minimum occurs around $t_d/t_h \approx -1$, where the projected state shows strong hexamerization ($\langle P_h \rangle$, i.e. the energy of the t_h bonds is significantly smaller than the energy of the t_d bonds denoted by $\langle P_d \rangle$, see Fig. 7.3). The minimum of the $0\pi\pi$–flux wave function also occurs around $t_d/t_h \approx -1$, with an energy -0.6807 per site (N_s =72) and shows dimerized pattern ($\langle P_d \rangle < \langle P_h \rangle$). The two energies are quite close to each other, but calculations on N_s=288 around the minima shows, that while the energy of the dimerized state slightly depends on the cluster size, the energy of the hexamerized state is further lowered when going to the 288-site cluster (shown in the inset of Fig. 7.3(a)). In both cases the statistical error of the Monte Carlo results is around 10^{-4}. This shows that in the thermodynamic limit the hexamerized $\pi 00$-flux state has clearly a lower variational energy than the dimerized $0\pi\pi$–flux state, in agreement with the iPEPS results. The energy of the $\pi\pi\pi$, 000, and chiral states are all above the $\pi 00$ and $0\pi\pi$ states. We have also compared the energy of different chiral states on the 72 site cluster: $E(\Phi\Phi'\Phi') = -0.671$, $E(\Phi\Phi\Phi) = -0.662$, $E(\Phi'\Phi\Phi) = -0.629$, and $E(\Phi'\Phi'\Phi') = -0.604$, where $\Phi = 2\pi/3$ and $\Phi' = \pi + \Phi = 5\pi/3$.

In both the $\pi 00$–flux state, and of its main competitor, the dimerized $0\pi\pi$–flux state, the minimum energy is around $t_d = -t_h$. In the hexamerized $\pi 00$–flux state (Fig. 7.4a) there is a gap between the filled and empty bands. By contrast, the Fermi level for the dimerized $0\pi\pi$–flux state is inside the bands (Fig. 7.4b-d), and the $t_d = -t_h$ point is special, for $t_d \leq -t_h$ the Fermi surface is reduced to two Dirac-points at the K_0 equivalent sites.

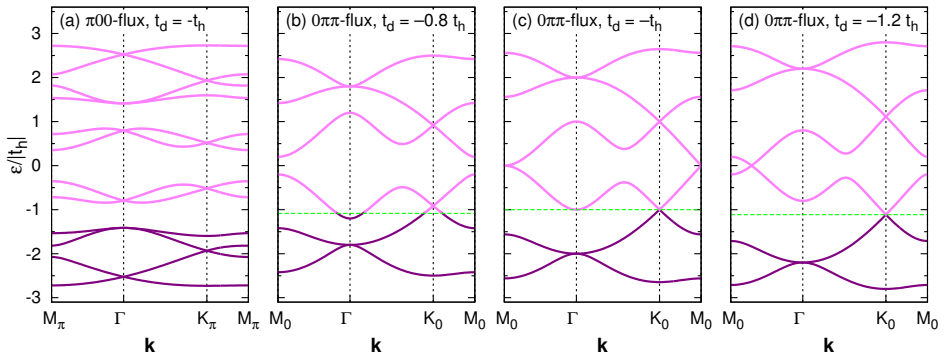

FIGURE 7.4: (a) The band structures of the free fermion Hamiltonian along the path $M_\pi \Gamma K_\pi M_\pi$ for the hexamerized $\pi 00$-flux state ($t_d = -t_h$). (b)-(d) The band structure of the dimerized $0\pi\pi$-flux state for different values of t_d along the path $M_0 \Gamma K_0 M_0$. For $t_d/t_h < -1$ the Fermi surface is a Dirac point at K_0 — the minimal energy for the $0\pi\pi$-flux configuration corresponds to the case when the Fermi sea touches the lowest empty band at the Γ point for $t_d = -t_h$ [plot (c)]. The dark and light purple lines denote occupied and empty bands, respectively, the green dashed line shows the Fermi energy.

7.3.1 Stability towards SU(3) symmetry breaking

Up to this point all Gutzwiller projected variational states were SU(3) symmetric, since there was no color dependent term in the free fermionic Hamiltonian. To check the stability towards color ordering suggested by iPEPS results at low bond dimensions we allow for color dependent hopping parameters and onsite energies around the minimal energy states with $t_d = -t_h$. For each color we introduce a negative onsite energy ϵ_{LRO} according to the pattern found by iPEPS. Furthermore we also allowed for a modified hoping amplitude (denoted by t_{LRO}) for the two colors that form the antisymmetric pair on the dimerized bonds, while for the third color the hopping amplitude is left unchanged. On non-dimerized bonds the hopping ampiltude is also left unchanged for all colors. Fig. 7.5 illustrates the pattern of modified hopping amplitudes and onsite energies. The sign of the hopping parameters are set to display the appropriate flux state. Note that upon reversing the sign of t_{LRO} the fluxes on the hexagons do not change, since for each color, we change the sign of two (or none) of the hopping parameters around a hexagon.

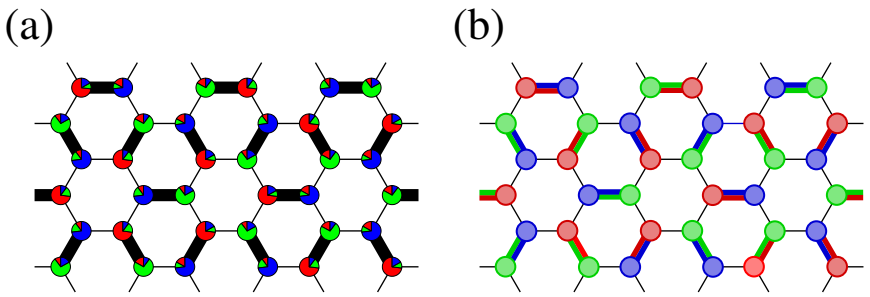

FIGURE 7.5: (a) The color ordered iPEPS results for the 18-site unit cell, (b) and the color dependent hopping amplitude and onsite energy pattern to enforce long range order in the Gutzwiller-projected states. The colored discs denote an onsite energy term, while the colored bonds show where the hopping amplitude is changed for the corresponding colors. On each site an onsite energy is introduced for one color only, and on the highlighted bonds the hopping amplitude is changed to t_{LRO} for two colors. On the thin black bonds the hopping amplitudes are left unchanged for all colors.

Fig. 7.6 shows the energy of the Gutzwiller projected state as a function of ϵ_{LRO} and t_{LRO} for the $0\pi\pi$ and $\pi 00$ flux states. It can be clearly seen that the energy is minimal for $\epsilon_{\mathrm{LRO}} = 0$ and $t_{\mathrm{LRO}} = t_h$, i.e. for the case where there is no long-range order in the system.

We have repeated the calculation also for the 000 and $\pi\pi\pi$ case as well, starting from $t_d = t_h$, and we found that the long-range color ordered phase is stabilized for the 000–flux state with energy $E = -0.610$ per site (for $t_{\mathrm{LRO}}/|t_H| = 1.3$ and $\epsilon_{\mathrm{LRO}}/|t_h| = -0.4$), much higher than the lowest energy $\pi 00$ solution.

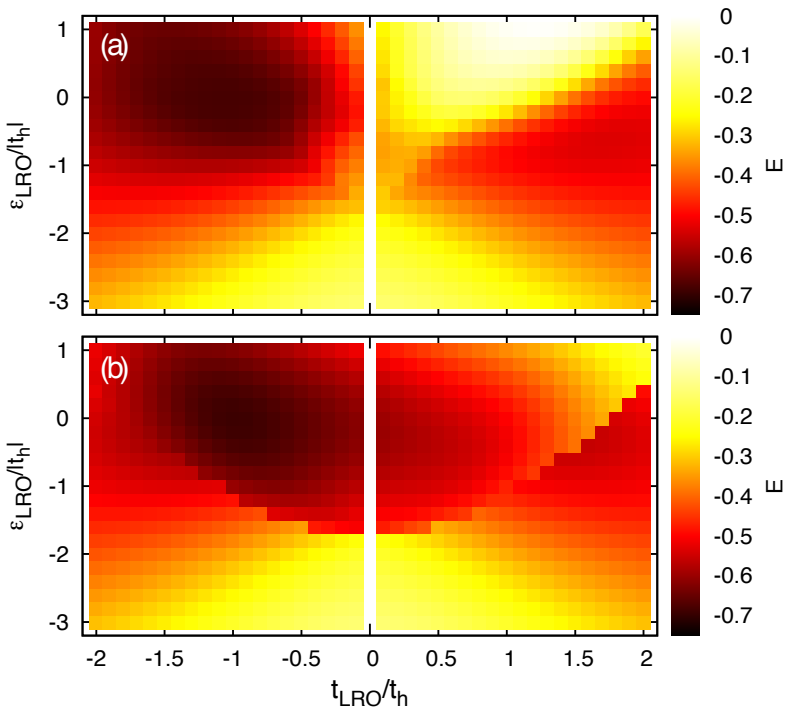

FIGURE 7.6: The stability of the dimerized and hexamerized states versus the formation of long range order, in the (a) $0\pi\pi$ and (b) $\pi 00$ flux state, respectively. For both cases the energy is minimal for $\epsilon_{\mathrm{LRO}} = 0$ and $t_{\mathrm{LRO}} = t_h$, where there is no long range order. The calculations were made with stepsizes $\Delta t_{\mathrm{LRO}} = 0.1|t_h|$ and $\Delta\epsilon_{\mathrm{LRO}} = 0.2|t_h|$. For $t_{\mathrm{LRO}} = 0$ the fermionic band structure collapses to a few highly degenerate bands, which caused numerical difficulties in the Monte Carlo code we used for the calculation.

7.4 Conclusions

In this chapter we showed the results of variational Gutzwiller-projection approach, which support the findings of systematic iPEPS calculations. Both methods found that the ground state of the SU(3) Heisenberg-model is hexamerized with no SU(3) symmetry breaking. The findings of LFWT of a dimerized structure can be understood as a low-entanglement solution, which is unstable if we allow for more entanglement in the system. This picture is supported by iPEPS results showing a dimerized color ordered solution for low tensor dimensions, although for higher tensor dimensions the hexamerized case becomes energetically favorable. Gutzwiller projection approach found both a hexamerized and dimerized solutions, the energies of the two cases are near to each other, but the Monte Carlo calculations clearly prefer the hexamerized scenario (the energy difference is small, but still 2 magnitude larger than, the statistical error of the VMC calculations). The Gutzwiller projection approach showed no sign of color-ordering in the system, though a stable dimerized color ordered state was found at much higher energies. It is also worth mentioning the free fermion band structure in the competing hexamerized $0\pi\pi$ and dimerized $\pi 00$ cases. In both cases the energy minima were found near the uniform hopping amplitude ($t_d = -t_h$) configuration. In the $0\pi\pi$-flux configuration at this point the band structure is gapped

at the Fermi-level, and nothing particular is happening. However, in the dimerized case, the Fermi-surface is reduced to a Dirac-point for $t_d/t_h \leq -1$.

Chapter 8

Concluding remarks

In the introduction we discussed that the origin of magnetism in condensed matter physics in most of the cases is the localization of electrons. In case of the three leg tube the Heisenberg and ring exchange interactions can be understood as perturbative energies in the large-U limit. The Heisenberg interaction is a second order correction, while the ring exchange interaction can be derived from fourth order perturbation.

An SU(4) symmetric model can be also derived from the orbital degenerate Hubbard-model, with two orbitals per site. At special values of the parameters the effective spin-orbital exchange becomes SU(4) symmetric as discussed in the beginning of Chapter 4.

As a finishing thought for this work we would like to make another point which connect these two studies in a broader sense. In both cases numerical methods were an essential part of our studies. In case of the three-leg tubes exact diagonalization results gave the motivation to study these systems by showing non-trivial 0 energy ground states for the Batista-Trugman model. Later, the further evaluation of these results helped us understand the structure of these states and we were able to give an analytic description.

In case of the SU(3) and SU(4) models on the honeycomb lattice, the Monte Carlo calculations on the variational Gutzwiller projected wave function provided valuable insight to the ground state structure, and could give information on the correlations and energies. These calculations served as ”numerical experiments” on the system.

Both cases show the unique role of numerical methods. Computational physics sometimes serves as an experiment for theories, and sometimes as a theorem for experiments. Algorithms can make tedious theoretical calculations easier and much faster, while simulations which try to mimic the behavior of real systems can sometimes reveal new phenomena, inspiring further theoretical and experimental study of the system.

Appendix A

Exact ground states for spin tubes of even length

A.1 Dimerized ground state

The explicit form of the dimerized wave function of alternating spin and chirality singlets reads as

$$\sum_{\{\sigma_2,\sigma_4,\ldots,\sigma_L\}} \bigotimes_{i=1}^{L/2} (-1)^{(1/2-\sigma^z_{2i})} \left(|\nu^{-\sigma_{2i-2},1}_{2i-1} \nu^{\sigma_{2i},2}_{2i}\rangle - |\nu^{-\sigma_{2i-2},2}_{2i-1} \nu^{\sigma_{2i},1}_{2i}\rangle \right). \tag{A.1}$$

The $|\nu^{-\sigma_{2i-2},1}_{2i-1} \nu^{\sigma_{2i},2}_{2i}\rangle - |\nu^{-\sigma_{2i-2},2}_{2i-1} \nu^{\sigma_{2i},1}_{2i}\rangle$ term is a chirality singlet between triangles $2i-1$ and $2i$. The spin degrees of freedom of triangles $2i$ and $2i+1$ form a singlet bond $|\uparrow\downarrow\rangle - |\downarrow\uparrow\rangle$, therefore the spin of triangle $2i+1$ is the opposite to that of triangle $2i$, and the -1 factor takes care of the antisymmetrization.

A.2 The ground state with two domain walls

Most of the matrix elements of the Hamiltonian between 2-domain wall states, shown in Fig. 3.13 , can be derived from the one domain wall overlaps. As a reminder, the one domain wall onsite terms $\langle \xi^\sigma_m | \mathcal{H} | \xi^\sigma_m \rangle = 5/18$ $\langle \eta^\sigma_m | \mathcal{H} | \eta^\sigma_m \rangle = 5/6$ and the propagation of a domain wall is described by $\langle \xi^\sigma_m | \mathcal{H} | \eta^\sigma_{m\pm1} \rangle = -5\sqrt{3}/36$. These overlaps are valid for the infinitely long systems ($L \to \infty$), for finite systems we have other terms scaling as 2^{-L}.

For tubes of even length, the nonzero overlaps in the thermodynamic limit for $suficientlyseparatedm$ and n are:

$$\begin{aligned}
\left\langle \xi^{\uparrow}_m\xi^{\downarrow}_n - \xi^{\downarrow}_m\xi^{\uparrow}_n \right| \mathcal{H} \left| \xi^{\uparrow}_m\xi^{\downarrow}_n - \xi^{\downarrow}_m\xi^{\uparrow}_n \right\rangle &= 5/9, \\
\left\langle \eta^{\uparrow}_m\eta^{\downarrow}_n - \eta^{\downarrow}_m\eta^{\uparrow}_n \right| \mathcal{H} \left| \eta^{\uparrow}_m\eta^{\downarrow}_n - \eta^{\downarrow}_m\eta^{\uparrow}_n \right\rangle &= 5/3, \\
\left\langle \xi^{\uparrow}_m\eta^{\downarrow}_n - \xi^{\downarrow}_m\eta^{\uparrow}_n \right| \mathcal{H} \left| \xi^{\uparrow}_m\eta^{\downarrow}_n - \xi^{\downarrow}_m\eta^{\uparrow}_n \right\rangle &= 10/9, \\
\left\langle \xi^{\uparrow}_m\xi^{\downarrow}_n - \xi^{\downarrow}_m\xi^{\uparrow}_n \right| \mathcal{H} \left| \xi^{\uparrow}_m\eta^{\downarrow}_{n\pm1} - \xi^{\downarrow}_m\eta^{\uparrow}_{n\pm1} \right\rangle &= -5\sqrt{3}/36, \\
\left\langle \eta^{\uparrow}_m\eta^{\downarrow}_n - \eta^{\downarrow}_m\eta^{\uparrow}_n \right| \mathcal{H} \left| \eta^{\uparrow}_m\xi^{\downarrow}_{n\pm1} - \eta^{\downarrow}_m\xi^{\uparrow}_{n\pm1} \right\rangle &= -5\sqrt{3}/36.
\end{aligned}$$

For $\left|\xi^{\uparrow}_m\eta^{\downarrow}_n - \xi^{\downarrow}_m\eta^{\uparrow}_n\right\rangle$ $m-n$ is even, while for $\left|\xi^{\uparrow}_m\xi^{\downarrow}_n - \xi^{\downarrow}_m\xi^{\uparrow}_n\right\rangle$ and $\left|\eta^{\uparrow}_m\eta^{\downarrow}_n - \eta^{\downarrow}_m\eta^{\uparrow}_n\right\rangle$ $m-n$ is odd.

When the two domain walls get close, *i.e* they overlap spatially, both the diagonal and off-diagonal matrix element may differ from the general case, and they read

$$\begin{aligned}
\left\langle \eta^{\uparrow}_m\eta^{\downarrow}_{m+1} - \eta^{\downarrow}_m\eta^{\uparrow}_{m+1} \right| \mathcal{H} \left| \eta^{\uparrow}_m\eta^{\downarrow}_{m+1} - \eta^{\downarrow}_m\eta^{\uparrow}_{m+1} \right\rangle &= 5/6, \\
\left\langle \xi^{\uparrow}_m\xi^{\downarrow}_{m+1} - \xi^{\downarrow}_m\xi^{\uparrow}_{m+1} \right| \mathcal{H} \left| \xi^{\uparrow}_m\xi^{\downarrow}_{m+1} - \xi^{\downarrow}_m\xi^{\uparrow}_{m+1} \right\rangle &= 5/12, \\
\left\langle \xi^{\uparrow}_m\eta^{\downarrow}_{m+2} - \xi^{\downarrow}_m\eta^{\uparrow}_{m+2} \right| \mathcal{H} \left| \xi^{\uparrow}_m\eta^{\downarrow}_{m+2} - \xi^{\downarrow}_m\eta^{\uparrow}_{m+2} \right\rangle &= 5/4, \\
\left\langle \xi^{\uparrow}_m\xi^{\downarrow}_{m+1} - \xi^{\downarrow}_m\xi^{\uparrow}_{m+1} \right| \mathcal{H} \left| \xi^{\uparrow}_m\eta^{\downarrow}_{m+2} - \xi^{\downarrow}_m\eta^{\uparrow}_{m+2} \right\rangle &= -5/18, \\
\left\langle \zeta_{m+\frac{1}{2}} \right| \mathcal{H} \left| \zeta_{m+\frac{1}{2}} \right\rangle &= 5/6, \\
\left\langle \xi^{\uparrow}_m\xi^{\downarrow}_{m+1} - \xi^{\downarrow}_m\xi^{\uparrow}_{m+1} \right| \mathcal{H} \left| \zeta_{m+\frac{1}{2}} \right\rangle &= -5\sqrt{6}/36.
\end{aligned}$$

These states are orthonormal (*i.e.* the overlap matrix is identity) in the $L \to \infty$ limit. The matrix elements given above were used to produce the variational results in Fig. 3.14.

The third exact ground state of $\mathcal{H}_{K_\Delta=0}$ is then given as

$$\begin{aligned}
\Psi_{2dw} = \; & \sqrt{2}\zeta(\pi) + 2\sqrt{3}\,|\xi\xi\,(\pi,1)\rangle + 3\sum_{l=4,\text{odd}}^{L/2} (-1)^{\frac{l-1}{2}}\,|\xi\xi\,(\pi,l)\rangle \\
& - \sqrt{3}i\sum_{l=2,\text{even}}^{L-2} (-1)^{\frac{l}{2}}\,|\xi\eta\,(\pi,l)\rangle - \sum_{l=1,\text{odd}}^{L/2} (-1)^{\frac{l-1}{2}}\,|\eta\eta\,(\pi,l)\rangle
\end{aligned} \tag{A.2}$$

This wave function is actually valid for a system of arbitrary even length L. Above we use the Fourier transform with the following phase convention

$$\begin{aligned}
\xi\xi\,(k,l) &= \sum_m \left|\xi^{\uparrow}_m \xi^{\downarrow}_{m,m+l} - \xi^{\downarrow}_m \xi^{\uparrow}_{m,m+l}\right\rangle \exp\left(ik\left(m+\frac{l}{2}\right)\right) \\
\eta\eta\,(k,l) &= \sum_m \left|\eta^{\uparrow}_m \eta^{\downarrow}_{m,m+l} - \eta^{\downarrow}_m \eta^{\uparrow}_{m,m+l}\right\rangle \exp\left(ik\left(m+\frac{l}{2}\right)\right) \\
\xi\eta\,(k,l) &= \sum_m \left|\xi^{\uparrow}_m \xi^{\downarrow}_{m,m+l} - \xi^{\downarrow}_m \xi^{\uparrow}_{m,m+l}\right\rangle \exp\left(ik\left(m+\frac{l}{2}\right)\right) \\
\zeta(k) &= \sum_m \left|\zeta_{m+\frac{1}{2}}\right\rangle \exp\left(ik(m+\frac{1}{2})\right)
\end{aligned} \tag{A.3}$$

for $\xi\xi\,(k,l)$ and $\eta\eta\,(k,l)$ l is odd and $1 \le l \le L/2$ since $\xi\xi\,(k,l) = -\xi\xi\,(k,-l)$, while for $\xi\eta\,(k,l)$ l is even and runs from 2 to $L-2$. $m + l/2$ corresponds to the center of mass of the two domain walls, and k is the total wave number.

Bibliography

[1] Patrik Fazekas. *Lecture Notes on Electron Correlation and Magnetism*. Series in Modern Condensed Matter Physics. World Scientific (Singapore, New Jersey, London, Hong Kong), 1999.

[2] Martin C. Gutzwiller. Effect of correlation on the ferromagnetism of transition metals. *Phys. Rev. Lett.*, 10:159–162, Mar 1963. doi: 10.1103/PhysRevLett.10.159. URL http://link.aps.org/doi/10.1103/PhysRevLett.10.159.

[3] J. Hubbard. Electron correlations in narrow energy bands. *Proceedings of the Royal Society of London. Series A. Mathematical and Physical Sciences*, 276(1365):238–257, 1963. doi: 10.1098/rspa.1963.0204. URL http://rspa.royalsocietypublishing.org/content/276/1365/238.abstract.

[4] Junjiro Kanamori. Electron correlation and ferromagnetism of transition metals. *Progress of Theoretical Physics*, 30(3):275–289, 1963. doi: 10.1143/PTP.30.275. URL http://ptp.ipap.jp/link?PTP/30/275/.

[5] P. W. Anderson. New approach to the theory of superexchange interactions. *Phys. Rev.*, 115:2–13, Jul 1959. doi: 10.1103/PhysRev.115.2. URL http://link.aps.org/doi/10.1103/PhysRev.115.2.

[6] M Takahashi. Half-filled hubbard model at low temperature. *Journal of Physics C: Solid State Physics*, 10(8):1289, 1977. URL http://stacks.iop.org/0022-3719/10/i=8/a=031.

[7] R. Coldea, S. M. Hayden, G. Aeppli, T. G. Perring, C. D. Frost, T. E. Mason, S.-W. Cheong, and Z. Fisk. Spin waves and electronic interactions in la_2cuo_4. *Phys. Rev. Lett.*, 86:5377–5380, Jun 2001. doi: 10.1103/PhysRevLett.86.5377. URL http://link.aps.org/doi/10.1103/PhysRevLett.86.5377.

[8] MC Cross and DD Osheroff. Novel Magnetic Properties of Solid He-3. *Physics Today*, 40(2):35–41, FEB 1987. ISSN 0031-9228.

[9] K I spin and D I Khomskii. The jahn-teller effect and magnetism: transition metal compounds. *Soviet Physics Uspekhi*, 25(4):231, 1982. URL http://stacks.iop.org/0038-5670/25/i=4/a=R03.

[10] C. Castellani, C. R. Natoli, and J. Ranninger. Magnetic structure of v_2o_3 in the insulating phase. *Phys. Rev. B*, 18:4945–4966, Nov 1978. doi: 10.1103/PhysRevB.18.4945. URL http://link.aps.org/doi/10.1103/PhysRevB.18.4945.

[11] C. Castellani, C. R. Natoli, and J. Ranninger. Insulating phase of v_2o_3: An attempt at a realistic calculation. *Phys. Rev. B*, 18:4967–5000, Nov 1978. doi: 10.1103/PhysRevB.18.4967. URL http://link.aps.org/doi/10.1103/PhysRevB.18.4967.

[12] Patrik Fazekas. *Antiferromágnesség, és Szimmetriasértés*. A szilárdtestkutatás újabb eredményei. Akadémia Kiadó, 1978.

[13] L. Berger, S. A. Friedberg, and J. T. Schriempf. Magnetic susceptibility of cu $(NO_3)_2 \cdot 2.5h_2o$ at low temperature. *Phys. Rev.*, 132:1057–1061, Nov 1963. doi: 10.1103/PhysRev.132.1057. URL http://link.aps.org/doi/10.1103/PhysRev.132.1057.

[14] David Adler. Mechanisms for metal-nonmental transitions in transition-metal oxides and sulfides. *Rev. Mod. Phys.*, 40:714–736, Oct 1968. doi: 10.1103/RevModPhys.40.714. URL http://link.aps.org/doi/10.1103/RevModPhys.40.714.

[15] M. Azuma, Z. Hiroi, M. Takano, K. Ishida, and Y. Kitaoka. Observation of a spin gap in $srcu_2o_3$ comprising spin-1/2 quasi-1d two-leg ladders. *Phys. Rev. Lett.*, 73:3463–3466, Dec 1994. doi: 10.1103/PhysRevLett.73.3463. URL http://link.aps.org/doi/10.1103/PhysRevLett.73.3463.

[16] H. Kageyama, K. Yoshimura, R. Stern, N. V. Mushnikov, K. Onizuka, M. Kato, K. Kosuge, C. P. Slichter, T. Goto, and Y. Ueda. Exact dimer ground state and quantized magnetization plateaus in the two-dimensional spin system $srcu_2(bo_3)_2$. *Phys. Rev. Lett.*, 82:3168–3171, Apr 1999. doi: 10.1103/PhysRevLett.82.3168. URL http://link.aps.org/doi/10.1103/PhysRevLett.82.3168.

[17] L. Hulthén. Über das Austauschproblem eines Kristalls. *Ark. Mat. Astron. Fysik A*, 26 (11):106 p., 1938.

[18] P.W. Anderson. Resonating valence bonds: A new kind of insulator? *Materials Research Bulletin*, 8(2):153 – 160, 1973. ISSN 0025-5408. doi: 10.1016/0025-5408(73)90167-0. URL http://www.sciencedirect.com/science/article/pii/0025540873901670.

[19] P. Fazekas and P. W. Anderson. On the ground state properties of the anisotropic triangular antiferromagnet. *Philosophical Magazine*, 30(2):423–440, 1974. doi: 10.1080/14786439808206568. URL http://www.tandfonline.com/doi/abs/10.1080/14786439808206568.

[20] B. Bernu, C. Lhuillier, and L. Pierre. Signature of néel order in exact spectra of quantum antiferromagnets on finite lattices. *Phys. Rev. Lett.*, 69:2590–2593, Oct 1992. doi: 10.1103/PhysRevLett.69.2590. URL http://link.aps.org/doi/10.1103/PhysRevLett.69.2590.

[21] R. Moessner and S. L. Sondhi. Resonating valence bond phase in the triangular lattice quantum dimer model. *Phys. Rev. Lett.*, 86:1881–1884, Feb 2001. doi: 10.1103/PhysRevLett.86.1881. URL http://link.aps.org/doi/10.1103/PhysRevLett.86.1881.

[22] L. Balents, M. P. A. Fisher, and S. M. Girvin. Fractionalization in an easy-axis kagome antiferromagnet. *Phys. Rev. B*, 65:224412, May 2002. doi: 10.1103/PhysRevB.65.224412. URL http://link.aps.org/doi/10.1103/PhysRevB.65.224412.

[23] O. I. Motrunich and T. Senthil. Exotic order in simple models of bosonic systems. *Phys. Rev. Lett.*, 89:277004, Dec 2002. doi: 10.1103/PhysRevLett.89.277004. URL http://link.aps.org/doi/10.1103/PhysRevLett.89.277004.

[24] Leon Balents. Spin liquids in frustrated magnets. *Nature*, 464(7286):199–208, 03 2010. URL http://dx.doi.org/10.1038/nature08917.

[25] Patrick A. Lee. An end to the drought of quantum spin liquids. *Science*, 321(5894):1306–1307, 2008. doi: 10.1126/science.1163196. URL http://www.sciencemag.org/content/321/5894/1306.short.

[26] Arthur P. Ramirez. Quantum spin liquids: A flood or a trickle? *Nat Phys*, 4(6):442–443, 06 2008. URL http://dx.doi.org/10.1038/nphys978.

[27] F. Verstraete, V. Murg, and J.I. Cirac. Matrix product states, projected entangled pair states, and variational renormalization group methods for quantum spin systems. *Advances in Physics*, 57(2):143–224, 2008. doi: 10.1080/14789940801912366. URL http://www.tandfonline.com/doi/abs/10.1080/14789940801912366.

[28] Z. Y. Meng, T. C. Lang, S. Wessel, F. F. Assaad, and A. Muramatsu. Quantum spin liquid emerging in two-dimensional correlated dirac fermions. *Nature*, 464(7290):847–851, 04 2010. URL http://dx.doi.org/10.1038/nature08942.

[29] S. Nakatsuji, K. Kuga, K. Kimura, R. Satake, N. Katayama, E. Nishibori, H. Sawa, R. Ishii, M. Hagiwara, F. Bridges, T. U. Ito, W. Higemoto, Y. Karaki, M. Halim,

A. A. Nugroho, J. A. Rodriguez-Rivera, M. A. Green, and C. Broholm. Spin-orbital short-range order on a honeycomb-based lattice. *Science*, 336(6081):559–563, 2012. doi: 10.1126/science.1212154. URL http://www.sciencemag.org/content/336/6081/559.abstract.

[30] A. V. Gorshkov, M. Hermele, V. Gurarie, C. Xu, P. S. Julienne, J. Ye, P. Zoller, E. Demler, M. D. Lukin, and A. M. Rey. Two-orbital SU(N) magnetism with ultracold alkaline-earth atoms. *Nat Phys*, 6(4):289–295, 2010. doi: 10.1038/nphys1535.

[31] FJ Dyson, EH Lieb, and B Simon. Phase-transitions in Quantum Spin Systems with Isotropic and Non-isotropic Interactions. *Journal of Statistical Physics*, 18(4):335–383, 1978. ISSN 0022-4715. doi: {10.1007/BF01106729}.

[32] Hidetoshi Nishimori, Kenn Kubo, Yukiyasu Ozeki, Yasuhiro Tomita, and Tatsuya Kishi. Long-range order in the xxz model. *Journal of Statistical Physics*, 55(1-2):259–277, 1989. ISSN 0022-4715. doi: 10.1007/BF01042599. URL http://dx.doi.org/10.1007/BF01042599.

[33] Anders W. Sandvik. Finite-size scaling of the ground-state parameters of the two-dimensional heisenberg model. *Phys. Rev. B*, 56:11678–11690, Nov 1997. doi: 10.1103/PhysRevB.56.11678. URL http://link.aps.org/doi/10.1103/PhysRevB.56.11678.

[34] K Okamoto and K Nomura. Fluid dimer critical-point in S=1/2 antiferromagnetic Heisenberg-chain with next-nearest-neighbor interactions. *Physics Letters A*, 169(6):433–437, OCT 12 1992. ISSN 0375-9601. doi: {10.1016/0375-9601(92)90823-5}.

[35] Chanchal K. Majumdar and Dipan K. Ghosh. On next-nearest-neighbor interaction in linear chain. ii. *Journal of Mathematical Physics*, 10(8):1399–1402, 1969. doi: 10.1063/1.1664979. URL http://link.aip.org/link/?JMP/10/1399/1.

[36] B. Sriram Shastry and Bill Sutherland. Excitation spectrum of a dimerized next-neighbor antiferromagnetic chain. *Phys. Rev. Lett.*, 47:964–967, Sep 1981. doi: 10.1103/PhysRevLett.47.964. URL http://link.aps.org/doi/10.1103/PhysRevLett.47.964.

[37] Elliott Lieb, Theodore Schultz, and Daniel Mattis. Two soluble models of an antiferromagnetic chain. *Annals of Physics*, 16(3):407 – 466, 1961. ISSN 0003-4916. doi: 10.1016/0003-4916(61)90115-4. URL http://www.sciencedirect.com/science/article/pii/0003491661901154.

[38] F. D. M. Haldane. Nonlinear field theory of large-spin heisenberg antiferromagnets: Semiclassically quantized solitons of the one-dimensional easy-axis néel state. *Phys.*

Rev. Lett., 50:1153–1156, Apr 1983. doi: 10.1103/PhysRevLett.50.1153. URL http://link.aps.org/doi/10.1103/PhysRevLett.50.1153.

[39] Ian Affleck, Tom Kennedy, ElliottH. Lieb, and Hal Tasaki. Valence bond ground states in isotropic quantum antiferromagnets. *Communications in Mathematical Physics*, 115: 477–528, 1988. ISSN 0010-3616. doi: 10.1007/BF01218021. URL http://dx.doi.org/10.1007/BF01218021.

[40] G. E. Granroth, M. W. Meisel, M. Chaparala, Th. Jolicœur, B. H. Ward, and D. R. Talham. Experimental evidence of a haldane gap in an $S = 2$ quasi-linear-chain antiferromagnet. *Phys. Rev. Lett.*, 77:1616–1619, Aug 1996. doi: 10.1103/PhysRevLett.77.1616. URL http://link.aps.org/doi/10.1103/PhysRevLett.77.1616.

[41] Hsiang-Hsuan Hung and Chang-De Gong. Numerical evidence of a spin-1?2 chain approaching a spin-1 chain. *Phys. Rev. B*, 71:054413, Feb 2005. doi: 10.1103/PhysRevB.71.054413. URL http://link.aps.org/doi/10.1103/PhysRevB.71.054413.

[42] Li-Hua Pan and Chang-De Gong. A note on haldane's conjecture. *Journal of Physics: Condensed Matter*, 20(21):215232, 2008. URL http://stacks.iop.org/0953-8984/20/i=21/a=215232.

[43] Luca Capriotti, Federico Becca, Alberto Parola, and Sandro Sorella. Resonating valence bond wave functions for strongly frustrated spin systems. *Phys. Rev. Lett.*, 87:097201, Aug 2001. doi: 10.1103/PhysRevLett.87.097201. URL http://link.aps.org/doi/10.1103/PhysRevLett.87.097201.

[44] O. P. Sushkov, J. Oitmaa, and Zheng Weihong. Quantum phase transitions in the two-dimensional J_1-J_2 model. *Phys. Rev. B*, 63:104420, Feb 2001. doi: 10.1103/PhysRevB.63.104420. URL http://link.aps.org/doi/10.1103/PhysRevB.63.104420.

[45] M. E. Zhitomirsky and Kazuo Ueda. Valence-bond crystal phase of a frustrated spin-1/2 square-lattice antiferromagnet. *Phys. Rev. B*, 54:9007–9010, Oct 1996. doi: 10.1103/PhysRevB.54.9007. URL http://link.aps.org/doi/10.1103/PhysRevB.54.9007.

[46] Matthieu Mambrini, Andreas Läuchli, Didier Poilblanc, and Frédéric Mila. Plaquette valence-bond crystal in the frustrated heisenberg quantum antiferromagnet on the square lattice. *Phys. Rev. B*, 74:144422, Oct 2006. doi: 10.1103/PhysRevB.74.144422. URL http://link.aps.org/doi/10.1103/PhysRevB.74.144422.

[47] C. D. Batista and S. A. Trugman. Exact ground states of a frustrated 2d magnet: Deconfined fractional excitations at a first-order quantum phase transition. *Phys. Rev. Lett.*, 93:217202, Nov 2004. doi: 10.1103/PhysRevLett.93.217202. URL http://link.aps.org/doi/10.1103/PhysRevLett.93.217202.

[48] Elbio Dagotto and T. M. Rice. Surprises on the way from one- to two-dimensional quantum magnets: The ladder materials. *Science*, 271(5249):618–623, 1996. doi: 10.1126/science.271.5249.618. URL http://www.sciencemag.org/content/271/5249/618.abstract.

[49] Tôru Sakai, Masahiro Sato, Kiyomi Okamoto, Kouichi Okunishi, and Chigak Itoi. Quantum spin nanotubes—frustration, competing orders and criticalities. *Journal of Physics: Condensed Matter*, 22(40):403201, 2010. URL http://stacks.iop.org/0953-8984/22/i=40/a=403201.

[50] S. Nishimoto and M. Arikawa. Low-lying excitations of the three-leg spin tube: A density-matrix renormalization group study. *Phys. Rev. B*, 78(5):054421, Aug 2008. doi: 10.1103/PhysRevB.78.054421.

[51] Tôru Sakai, Masahiro Sato, Kouichi Okunishi, Yuichi Otsuka, Kiyomi Okamoto, and Chigak Itoi. Quantum phase transitions of the asymmetric three-leg spin tube. *Phys. Rev. B*, 78(18):184415, Nov 2008. doi: 10.1103/PhysRevB.78.184415.

[52] Kouichi Okunishi, Shinichiro Yoshikawa, Tôru Sakai, and Seiji Miyashita. Low-energy excitations of the $s = 1/2$ quantum spin tube
with the triangular lattice structure. *Prog. Theor. Phys. Supplement*, 159:297–301, 2005. doi: 10.1143/PTPS.159.297. URL http://ptp.ipap.jp/link?PTPS/159/297/.

[53] J.-B. Fouet, A. Läuchli, S. Pilgram, R. M. Noack, and F. Mila. Frustrated three-leg spin tubes: From spin 12 with chirality to spin 32. *Phys. Rev. B*, 73:014409, Jan 2006. doi: 10.1103/PhysRevB.73.014409. URL http://link.aps.org/doi/10.1103/PhysRevB.73.014409.

[54] Hirotaka Manaka, Yuji Hirai, Yuta Hachigo, Masahiro Mitsunaga, Masakazu Ito, and Norio Terada. Spin-liquid state study of equilateral triangle $s = 3/2$ spin tubes formed in $cscrf_4$. *Journal of the Physical Society of Japan*, 78(9):093701, 2009. doi: 10.1143/JPSJ.78.093701. URL http://jpsj.ipap.jp/link?JPSJ/78/093701/.

[55] Georg Seeber, Paul Kogerler, Benson M. Kariuki, and Leroy Cronin. Supramolecular assembly of ligand-directed triangular CuII3Cl clusters with spin frustration and spin-chain behaviour. *Chem. Commun.*, pages 1580–1581, 2004. doi: 10.1039/B402487G. URL http://dx.doi.org/10.1039/B402487G.

[56] Jürgen Schnack, Hiroyuki Nojiri, Paul Kögerler, Geoffrey J. T. Cooper, and Leroy Cronin. Magnetic characterization of the frustrated three-leg ladder compound $[(CuCl_2tachH)_3Cl]cl_2$. *Phys. Rev. B*, 70:174420, Nov 2004. doi: 10.1103/PhysRevB.70.174420. URL http://link.aps.org/doi/10.1103/PhysRevB.70.174420.

[57] Ivar Martin and C. D. Batista. Itinerant electron-driven chiral magnetic ordering and spontaneous quantum hall effect in triangular lattice models. *Phys. Rev. Lett.*, 101:156402, Oct 2008. doi: 10.1103/PhysRevLett.101.156402. URL http://link.aps.org/doi/10.1103/PhysRevLett.101.156402.

[58] Y. Shiomi, M. Mochizuki, Y. Kaneko, and Y. Tokura. Hall effect of spin-chirality origin in a triangular-lattice helimagnet $fe_{1.3}Sb$. *Phys. Rev. Lett.*, 108:056601, Jan 2012. doi: 10.1103/PhysRevLett.108.056601. URL http://link.aps.org/doi/10.1103/PhysRevLett.108.056601.

[59] E. Orignac, R. Citro, and N. Andrei. Low-energy behavior of the spin-tube and spin-orbital models. *Phys. Rev. B*, 61(17):11533–11551, May 2000. doi: 10.1103/PhysRevB.61.11533.

[60] Kenro Kawano and Minoru Takahashi. Three-leg antiferromagnetic heisenberg ladder with frustrated boundary condition; ground state properties. *J. Phys. Soc. Jpn.*, 66(12):4001–4008, 1997. doi: 10.1143/JPSJ.66.4001. URL http://jpsj.ipap.jp/link?JPSJ/66/4001/.

[61] A. K. Kolezhuk, H.-J. Mikeska, and U. Schollwöck. Elementary excitations in one-dimensional spin-orbit models: Neutral and charged solitons and their bound states. *Phys. Rev. B*, 63:064418, Jan 2001. doi: 10.1103/PhysRevB.63.064418. URL http://link.aps.org/doi/10.1103/PhysRevB.63.064418.

[62] Yu. A. Fridman, O. A. Kosmachev, A. K. Kolezhuk, and B. A. Ivanov. Spin nematic and antinematic states in a spin-$\frac{3}{2}$ isotropic non-heisenberg magnet. *Phys. Rev. Lett.*, 106:097202, Mar 2011. doi: 10.1103/PhysRevLett.106.097202. URL http://link.aps.org/doi/10.1103/PhysRevLett.106.097202.

[63] Andreas Lüscher, Reinhard M. Noack, Grégoire Misguich, Valeri N. Kotov, and Frédéric Mila. Soliton binding and low-lying singlets in frustrated odd-legged $s = \frac{1}{2}$ spin tubes. *Phys. Rev. B*, 70:060405, Aug 2004. doi: 10.1103/PhysRevB.70.060405. URL http://link.aps.org/doi/10.1103/PhysRevB.70.060405.

[64] Congjun Wu, Jiang-ping Hu, and Shou-cheng Zhang. Exact so(5) symmetry in the spin-3/2 fermionic system. *Phys. Rev. Lett.*, 91:186402, Oct 2003. doi: 10.1103/PhysRevLett.91.186402. URL http://link.aps.org/doi/10.1103/PhysRevLett.91.186402.

[65] Carsten Honerkamp and Walter Hofstetter. Ultracold fermions and the SU(n) hubbard model. *Phys. Rev. Lett.*, 92:170403, Apr 2004. doi: 10.1103/PhysRevLett.92.170403. URL http://link.aps.org/doi/10.1103/PhysRevLett.92.170403.

[66] M A Cazalilla, A F Ho, and M Ueda. Ultracold gases of ytterbium: ferromagnetism and mott states in an su(6) fermi system. *New Journal of Physics*, 11(10):103033, 2009. URL http://stacks.iop.org/1367-2630/11/i=10/a=103033.

[67] Walther Gerlach and Otto Stern. Das magnetische moment des silberatoms. *Zeitschrift für Physik*, 9(1):353–355, 1922. ISSN 0044-3328. doi: 10.1007/BF01326984. URL http://dx.doi.org/10.1007/BF01326984.

[68] Bretislav Friedrich and Dudley Herschbach. Stern and gerlach: How a bad cigar helped reorient atomic physics. *Physics Today*, 56(12):53–59, 2003. doi: 10.1063/1.1650229. URL http://link.aip.org/link/?PTO/56/53/1.

[69] Friedel Weinert. Wrong theory – right experiment: The significance of the stern-gerlach experiments. *Studies in History and Philosophy of Science Part B: Studies in History and Philosophy of Modern Physics*, 26(1):75 – 86, 1995. ISSN 1355-2198. doi: 10.1016/1355-2198(95)00002-B. URL http://www.sciencedirect.com/science/article/pii/135521989500002B.

[70] C. Monesi, C. Meneghini, F. Bardelli, M. Benfatto, S. Mobilio, U. Manju, and D. D. Sarma. Local structure in $lamno_3$ and $camno_3$ perovskites: A quantitative structural refinement of mn *k*-edge xanes data. *Phys. Rev. B*, 72:174104, Nov 2005. doi: 10.1103/PhysRevB.72.174104. URL http://link.aps.org/doi/10.1103/PhysRevB.72.174104.

[71] Karlo Penc, Matthieu Mambrini, Patrik Fazekas, and Frédéric Mila. Quantum phase transition in the su(4) spin-orbital model on the triangular lattice. *Phys. Rev. B*, 68:012408, Jul 2003. doi: 10.1103/PhysRevB.68.012408. URL http://link.aps.org/doi/10.1103/PhysRevB.68.012408.

[72] Mathias van den Bossche, Patrick Azaria, Philippe Lecheminant, and Frédéric Mila. Spontaneous plaquette formation in the SU(4) Spin-Orbital ladder. *Phys. Rev. Lett.*, 86 (18):4124, April 2001. doi: 10.1103/PhysRevLett.86.4124.

[73] Ian Affleck. Large-*n* limit of SU(*n*) quantum "spin" chains. *Phys. Rev. Lett.*, 54:966–969, Mar 1985. doi: 10.1103/PhysRevLett.54.966. URL http://link.aps.org/doi/10.1103/PhysRevLett.54.966.

[74] Ian Affleck and J. Brad Marston. Large- *n* limit of the heisenberg-hubbard model: Implications for high-T_c superconductors. *Phys. Rev. B*, 37:3774–3777, Mar 1988. doi: 10.1103/PhysRevB.37.3774. URL http://link.aps.org/doi/10.1103/PhysRevB.37.3774.

[75] Daniel P. Arovas. Simplex solid states of SU(n) quantum antiferromagnets. *Phys. Rev. B*, 77:104404, Mar 2008. doi: 10.1103/PhysRevB.77.104404. URL http://link.aps.org/doi/10.1103/PhysRevB.77.104404.

[76] M. van den Bossche, F.-C. Zhang, and F. Mila. Plaquette ground state in the two-dimensional SU(4) spin-orbital model. *Eur. Phys. J. B*, 17(3):367–370, October 2000. doi: 10.1007/PL00011085.

[77] A. Joshi, M. Ma, F. Mila, D. N. Shi, and F. C. Zhang. Elementary excitations in magnetically ordered systems with orbital degeneracy. *Phys. Rev. B*, 60:6584–6587, Sep 1999. doi: 10.1103/PhysRevB.60.6584. URL http://link.aps.org/doi/10.1103/PhysRevB.60.6584.

[78] Tamás A. Tóth, Andreas M. Läuchli, Frédéric Mila, and Karlo Penc. Three-sublattice ordering of the su(3) heisenberg model of three-flavor fermions on the square and cubic lattices. *Phys. Rev. Lett.*, 105:265301, Dec 2010. doi: 10.1103/PhysRevLett.105.265301. URL http://link.aps.org/doi/10.1103/PhysRevLett.105.265301.

[79] Philippe Corboz, Andreas M. Läuchli, Karlo Penc, Matthias Troyer, and Frédéric Mila. Simultaneous dimerization and SU(4) symmetry breaking of 4-Color fermions on the square lattice. *Phys. Rev. Lett.*, 107(21):215301, November 2011. doi: 10.1103/PhysRevLett.107.215301.

[80] Yu-Wen Lee and Min-Fong Yang. Spontaneous dimerization in the spin-1 bilinear-biquadratic heisenberg model on a honeycomb lattice. *Phys. Rev. B*, 85:100402, Mar 2012. doi: 10.1103/PhysRevB.85.100402. URL http://link.aps.org/doi/10.1103/PhysRevB.85.100402.

[81] Philippe Corboz, Miklós Lajkó, Andreas M. Läuchli, Karlo Penc, and Frédéric Mila. Spin-orbital quantum liquid on the honeycomb lattice. *Phys. Rev. X*, 2:041013, Nov 2012. doi: 10.1103/PhysRevX.2.041013. URL http://link.aps.org/doi/10.1103/PhysRevX.2.041013.

[82] G. Szirmai, E. Szirmai, A. Zamora, and M. Lewenstein. Gauge fields emerging from time-reversal symmetry breaking for spin-5/2 fermions in a honeycomb lattice. *Phys. Rev. A*, 84:011611, Jul 2011. doi: 10.1103/PhysRevA.84.011611. URL http://link.aps.org/doi/10.1103/PhysRevA.84.011611.

[83] T. A. Kaplan, P. Horsch, and P. Fulde. Close relation between localized-electron magnetism and the paramagnetic wave function of completely itinerant electrons. *Phys. Rev. Lett.*, 49:889–892, Sep 1982. doi: 10.1103/PhysRevLett.49.889. URL http://link.aps.org/doi/10.1103/PhysRevLett.49.889.

[84] A. F. Albuquerque, D. Schwandt, B. Hetényi, S. Capponi, M. Mambrini, and A. M. Läuchli. Phase diagram of a frustrated quantum antiferromagnet on the honeycomb lattice: Magnetic order versus valence-bond crystal formation. *Phys. Rev. B*, 84:024406, Jul 2011. doi: 10.1103/PhysRevB.84.024406. URL http://link.aps.org/doi/10.1103/PhysRevB.84.024406.

[85] B. K. Clark, D. A. Abanin, and S. L. Sondhi. Nature of the spin liquid state of the hubbard model on a honeycomb lattice. *Phys. Rev. Lett.*, 107:087204, Aug 2011. doi: 10.1103/PhysRevLett.107.087204. URL http://link.aps.org/doi/10.1103/PhysRevLett.107.087204.

[86] Beat Frischmuth, Frédéric Mila, and Matthias Troyer. Thermodynamics of the one-dimensional SU(4) symmetric spin-orbital model. *Phys. Rev. Lett.*, 82:835–838, Jan 1999. doi: 10.1103/PhysRevLett.82.835.

[87] Michael Hermele, T. Senthil, and Matthew P. A. Fisher. Algebraic spin liquid as the mother of many competing orders. *Phys. Rev. B*, 72:104404, Sep 2005. doi: 10.1103/PhysRevB.72.104404. URL http://link.aps.org/doi/10.1103/PhysRevB.72.104404.

[88] Michael Hermele, Victor Gurarie, and Ana Maria Rey. Mott insulators of ultracold fermionic alkaline earth atoms: Underconstrained magnetism and chiral spin liquid. *Phys. Rev. Lett.*, 103:135301, Sep 2009. doi: 10.1103/PhysRevLett.103.135301. URL http://link.aps.org/doi/10.1103/PhysRevLett.103.135301.

[89] Fa Wang and Ashvin Vishwanath. Z_2 spin-orbital liquid state in the square lattice Kugel-Khomskii model. *Phys. Rev. B*, 80(6):064413, 2009. doi: 10.1103/PhysRevB.80.064413.

[90] Xiao-Gang Wen. Quantum orders and symmetric spin liquids. *Phys. Rev. B*, 65:165113, Apr 2002. doi: 10.1103/PhysRevB.65.165113. URL http://link.aps.org/doi/10.1103/PhysRevB.65.165113.

[91] Yuan-Ming Lu and Ying Ran. F_2 spin liquid and chiral antiferromagnetic phase in the hubbard model on a honeycomb lattice. *Phys. Rev. B*, 84:024420, Jul 2011. doi: 10.1103/PhysRevB.84.024420. URL http://link.aps.org/doi/10.1103/PhysRevB.84.024420.

[92] J. A. Kjäll, M. P. Zaletel, R. S. K. Mong, J. H. Bardarson, and F. Pollmann. The phase diagram of the anisotropic spin-2 XXZ model: an infinite system DMRG study. *ArXiv e-prints*, December 2012.

[93] M. E. J. Newman and G. T. Barkema. *Monte Carlo Methods in Statistical Physics*. Clarendon Press, 1999.

[94] Nicholas Metropolis, Arianna W. Rosenbluth, Marshall N. Rosenbluth, Augusta H. Teller, and Edward Teller. Equation of state calculations by fast computing machines. *The Journal of Chemical Physics*, 21(6):1087–1092, 1953. doi: 10.1063/1.1699114. URL http://link.aip.org/link/?JCP/21/1087/1.

[95] Vinay Ambegaokar and Matthias Troyer. Estimating errors reliably in Monte Carlo simulations of the Ehrenfest model. *American Journal of Physics*, 78(2):150–157, FEB 2010. ISSN 0002-9505. doi: {10.1119/1.3247985}.

[96] Bill Sutherland. Model for a multicomponent quantum system. *Phys. Rev. B*, 12:3795–3805, Nov 1975. doi: 10.1103/PhysRevB.12.3795. URL http://link.aps.org/doi/10.1103/PhysRevB.12.3795.

[97] Yasufumi Yamashita, Naokazu Shibata, and Kazuo Ueda. Su(4) spin-orbit critical state in one dimension. *Phys. Rev. B*, 58:9114–9118, Oct 1998. doi: 10.1103/PhysRevB.58.9114. URL http://link.aps.org/doi/10.1103/PhysRevB.58.9114.

[98] Ian Affleck. Exact critical exponents for quantum spin chains, non-linear σ-models at $\theta = \pi$ and the quantum hall effect. *Nuclear Physics B*, 265(3):409 – 447, 1986. ISSN 0550-3213. doi: 10.1016/0550-3213(86)90167-7. URL http://www.sciencedirect.com/science/article/pii/0550321386901677.

[99] Tian-Heng Han, Joel S. Helton, Shaoyan Chu, Daniel G. Nocera, Jose A. Rodriguez-Rivera, Collin Broholm, and Young S. Lee. Fractionalized excitations in the spin-liquid state of a kagome-lattice antiferromagnet. *Nature*, 492(7429):406–410, 12 2012. URL http://dx.doi.org/10.1038/nature11659.

[100] M. Lajkó and K. Penc. Tetramerization in a SU(4)-Heisenberg model on the honeycomb lattice. *ArXiv e-prints*, March 2013.

[101] H. H. Zhao, Cenke Xu, Q. N. Chen, Z. C. Wei, M. P. Qin, G. M. Zhang, and T. Xiang. Plaquette order and deconfined quantum critical point in the spin-1 bilinear-biquadratic heisenberg model on the honeycomb lattice. *Phys. Rev. B*, 85(13):134416, April 2012. doi: 10.1103/PhysRevB.85.134416. URL http://link.aps.org/doi/10.1103/PhysRevB.85.134416.

[102] P. Corboz, M. Lajkó, K. Penc, F. Mila, and A. M. Läuchli. Competing states in the SU(3) Heisenberg model on the honeycomb lattice: Plaquette valence-bond crystal versus dimerized color-ordered state. *ArXiv e-prints*, February 2013.

[103] Chang-Yu Hou, Claudio Chamon, and Christopher Mudry. Electron fractionalization in two-dimensional graphenelike structures. *Phys. Rev. Lett.*, 98:186809, May 2007. doi: 10.1103/PhysRevLett.98.186809. URL http://link.aps.org/doi/10.1103/PhysRevLett.98.186809.